Superconductivity in the intercalated graphite compounds C_6Yb and C_6Ca

Thomas Edward Weller

A Thesis Submitted to the
Faculty of Mathematical and Physical Sciences
in part fulfilment of the requirements for the
degree of Doctor of Philosophy

Department of Physics and Astronomy, UCL

September 2006

ProQuest LLC
789 East Eisenhower Parkway
P.O. Box 1346
Ann Arbor, MI 48106-1346

Abstract

This thesis concerns the discovery of superconductivity in the intercalated graphite compounds C_6Yb and C_6Ca. A novel technique for synthesis of these intercalates has been developed, and is presented in detail. These two materials are shown to superconduct at 6.5K and 11.5K respectively. The superconductivity is demonstrated by measurements of the magnetisation and resistivity. Initial measurements of the superconducting transition of these materials as a function of pressure shows an increase in the transition with increasing pressure.

Contents

Figures & Tables

Preface

The Bardeen Cooper Schrieffer (BCS) mechanism provided the first microscopic explanation of superconducting behaviour, in terms of mediating phonons, but superconductors have since been discovered that challenge this theoretical understanding. One alternative put forward in response to this challenge is spin fluctuation exchange, or magnetic mediation. In particular calculations suggested that quasi-2D nearly antiferromagnetic metals might provide fertile ground for finding new examples of magnetically mediated superconductivity [Monthoux 2001].

Mark Ellerby, Montu Saxena, and Neal Skipper came up with the idea that C_6Yb, one of many graphite intercalates, might provide an example of magnetically mediated superconductivity. This hypothesis was based on the combination of two arguments, firstly that graphite forms intercalation compounds that are quasi 2D in nature [Dresselhaus 1981], and secondly that ytterbium compounds are often proximal to an antiferromagnetic phase boundary [Bauer 1999]. Most importantly ions intercalated into graphite take on a triangular lattice, and this could potentially lead to frustration of any antiferromagnetism at the Yb site, with the frustration effects causing long range spin fluctuations at low temperatures.

Experimentally graphite intercalates are excellent candidates for studying dimensionally dependent phenomenon and are electronically sensitive to a number of control parameters, which may also be exploited to tune magnetic states [Solin 1988, Clarke 1981, Roth 1985]. Serendipitously ytterbium has a nearly isostructural and normally non-magnetic equivalent in calcium. Ca is favourable for a number of reasons [Klaasse 1981], most importantly ytterbium in its non-magnetic state and calcium are both divalent and the reported sandwich depth in a graphite intercalate differs by less than one percent between them [Enoki 2003].

This thesis describes my efforts to synthesise C_6Yb and C_6Ca and characterise their magnetic and transport properties. *Chapter 1* outlines an

experimentalist's perspective on the theory of superconductivity. It relies heavily on the texts of Tinkham [Tinkham 1975] and Waldram [Waldram 1996], which are recommended to the reader as excellent introductions to the subject. Other key texts are those of Kittel [Kittel 1996], Ashcroft & Mermin [Ashcroft 1976], and Ziman [Ziman 1960]. Theoretical ideas from these works, including aspects of the Ginzburg-Landau theory and the Bardeen-Cooper-Schrieffer theory, are distilled for an experimentalist's perspective relevant to the techniques employed for *Chapters 4,5*, and *6*. *Chapter 2* introduces the background to graphite intercalates, and consists of a brief introduction to their structure, with specific information on the electron and the phonon behaviour, and special reference to rare earth and alkali earth intercalants where available. The field of superconducting graphite intercalates is surveyed with particular attention paid to identifying trends and representing the proposed explanations of the superconductivity in intercalates. *Chapter 3* discusses the synthesis of graphite intercalation compounds. In particular it focuses on the alkali-earth and rare-earth binaries. A detailed report on the novel synthesis technique developed for the production of C_6Yb and C_6Ca is given. The structure and morphology of these samples are demonstrated through the use of X-ray diffraction (XRD) and scanning electron microscopy (SEM) with energy dispersive analysis of X-rays (EDAX). *Chapter 4* presents data gathered with a Quantum Design MPMS7 SQUID magnetometer from measurements on samples described in detail in *Chapter 3*. Data from supplementary measurements on ZYA HOPG and Yb_2O_3 are also included for the purpose of analysing the data and determining that behaviour attributable to the C_6Yb and C_6Ca. Chapter 5 presents data gathered with an Oxford Instruments MagLab cryogenic resistivity system from four-point measurements on samples synthesised according to the process described in *Chapter 3*. Data from measurements on ZYA HOPG is also included for the purpose of interpreting the data. Corroborating data gathered from measurements made by Robert P. Smith at the Cavendish Laboratory on samples I synthesised is also included. *Chapter 6* presents data from measurements of the pressure dependence of the superconducting transition in C_6Yb. This investigation of the pressure dependence of the superconducting transition temperature in C_6Yb was carried out using

magnetization measurements and resistivity measurements made in Cambridge. I carried out the magnetization measurements at UCL using a miniature CuBe piston clamp cell in a SQUID magnetometer and Robert P. Smith carried out the resistivity measurements using a piston cylinder clamp cell and low frequency AC four probe technique with an ADR. *Chapter 7* places the work I have done in context, discusses the work that has continued while this thesis has been written and what will be happening.

Acknowledgements

I would like to echo the sentiment of John Waldram, whose book has been so important in contributing to my understanding of this subject, "during the writing, I have frequently been alarmed by the feeling that the subject is moving faster than I was."

To all those who kept me moving, thank you. Mark Ellerby for standing by me when there wasn't a peak to be sniffed and for opening my eyes and ears, Neal Skipper for just the right dose of Black Adder at just the right moment, Montu Saxena for exciting tastes of the international scene, Chris Howard for getting me into this mess, and Arthur, Cecilia, Emily, Hels, Helen, Jonathan, Hayley, Eamonn, Jon, Shu, Anna, Rob, Mike, Steven, and Sibel, for helping me enjoy being in it. For their inspiration Mukul Laad, Mark Baxendale, Gil Lonzarich, Ben Simons, Gabe Aeppli, and Peter Littlewood.

Especially John Dumper, a neutral ear and a steady hand, without whom there would be no XRD measurements and John and Mike without whom there would be no samples.

My family and my friends, who have probably been cursing this thesis for some time now, and most especially Vicky, for putting up with this just when she thought she had got it all out of the way.

Finally some of our team's collaborators I have yet to have the pleasure of meeting: Gabor Csanyi, A.H. Nevidomskyy, Chris Pickard, Claudia Dallera, Matteo D'Astuto, M.Grioni, Ana Akrap, Titusz Feher, and Rainer Friedlein.

Chapter 1

Observing Superconductivity

This chapter outlines an experimentalist's perspective on the theory of superconductivity. It relies heavily on the texts of Tinkham [Tinkham 1975] and Waldram [Waldram 1996], which are recommended to the reader as excellent introductions to the subject. Other key texts are those of Kittel [Kittel 1996], Ashcroft & Mermin [Ashcroft 1976], and Ziman [Ziman 1960]. Theoretical ideas from these works, including aspects of the Ginzburg-Landau theory and the Bardeen-Cooper-Schrieffer theory, are distilled for a perspective relevant to the techniques employed for *Chapters 4*,*5*, and *6*.

1.1 Introduction

The reciprocal relation between experimental science and theoretical science, complementary aspects of scientific inquiry, is well illustrated by the development of our understanding of superconductivity [Bardeen 1972]. Kamerlinge-Onnes, a pioneer of low temperature physics, was expecting platinum and other metals to lose their resistance at low temperatures, as the factors he imagined to hinder electron motion disappeared. He was surprised by the abrupt transition to zero resistance he finally observed [Onnes 1913]. Magnetisation studies were delayed by the tacit assumption that the magnetic behaviour would be that of a perfect conductor; that flux would be trapped [Shoenberg 1962]. Observations, by Meissner and Ochsenfeld, of the expulsion of magnetic flux from a superconductor passing through the transition in an applied magnetic field were not made until 1933 [Tinkham 1975]. This stimulated an interest in magnetisation properties of superconductors which then led to what later became known as Type II superconductivity being observed in 1935, when De-Haas and Kasimir-Jonker measured magnetisation of superconducting alloys [Abrikosov 2003]. A satisfactory theory did not appear until 1950 when Ginzburg and Landau (GL) introduced the wavefunction Ψ as an order parameter in their phenomenological theory. It was also in 1950 that it was discovered that the transition temperature varied with mean atomic mass – the isotope effect. This coincided with and gave strong support to Fröhlich's suggestion that superconductivity might be associated with an electronic interaction mediated by deviation of ions from their lattice positions. In 1954 Abrikosov provided a numerical distinction between Type I and Type II in terms of only one parameter, the so-called Ginzburg Landau parameter. The ideas of London and Fröhlich were finally crystallised by John Bardeen, Leonard Cooper and John Schrieffer into the BCS theory, introduced in 1957.

1.2 Measuring T_c, and what it tells us

The two basic characteristics of superconductivity are zero resistance and magnetic flux expulsion. The onset of superconductivity can thus be observed by measurements of the temperature dependence of resistance with, for instance, a four-point probe technique, and by measurements of the magnetisation with respect to temperature.

The two basic theories of superconductivity, the phenomenological Ginzburg-Landau theory (GL) and the microscopic Bardeen-Cooper-Schrieffer theory (BCS), look at the phase transition from different perspectives. In the GL theory this is understood in terms of a phase transition to a state with a finite value of a superconducting wavefunction, Ψ, and in the BCS theory to the formation of an energy gap, Δ, between superconducting electrons, in so-called Cooper pairs, and the excitations of the system. Gorkov later showed that GL theory is a limiting form of the BCS, valid near T_C with Ψ proportional to Δ, Tinkham points out that Ψ can be thought of as the wavefunction of the centre of mass motion of the Cooper pairs [Tinkham p10]. However it is the many-particle condensate wavefunction Ψ, maintaining phase coherence over macroscopic distances that is the universal characteristic of the superconducting state [Tinkham p13].

Intuitive understanding of the relationship between the observable transition temperature and the internal properties of the system is provided by the BCS theory. If $\Delta << k_B\theta_D$, where θ_D is the Debye temperature and k_B the Boltzmann constant, then a superconductor is said to be in the weak coupling limit [Waldram p131, Tinkham p28]. In this case the BCS equations may be simplified by setting the general matrix element of the pair interaction potential, $V_{k'k}$, to a constant –V [Waldram p129], since the electrons have no feedback effect on the potential they will all observe the same potential. This approximation is valid for many conventional superconductors and it makes possible a computation of T_c on the basis of the Debye temperature θ_D, and the BCS coupling parameter NV:

$$T_C = 1.14\theta_D e^{-1/NV} \qquad (1.1).$$

N is the density of paired states at the Fermi energy (half the density of states) so this relation gives an expectation of the behaviour of T_c with respect to the density of states. The energy gap at T = 0 can also be calculated in this approximation and turns out to be:

$$\Delta_0 = 1.76 k_B T_C \qquad (1.2),$$

where k_B is the Boltzmann constant. From the experimental perspective T_C can, in the weak coupling limit, give an idea of both the coupling parameter and the size of the energy gap, if the Debye temperature is known.

Given that $k_B\theta_D = \hbar\omega_D$ [Ashcroft 1976], and that for simple harmonic motion the frequency $\omega \propto M^{-1/2}$, in pure metals an isotope effect such that $T_c \propto M^{-1/2}$ [Waldram p132] is expected to occur in the weak coupling limit. Although in alloys it is not correct to assume that all phonons scale simply with ion mass it was the unexpected or non-existent isotope effect in elemental Os, Ru and Zr that motivated Eliashberg to develop a strong coupling theory, and McMillan showed that these deviations could be explained by applying it [McMillan 1968].

In order to account for a more realistic interaction potential Eliashberg worked from the normal Fermi liquid state. The standard Green's function approach [Mattuck 1992] describes the effects of placing an electron into a system and the effects of that system on the new electron with the mathematical constructs for switching on an interaction adiabatically. However, it does not contain any information that can allow perturbation theory to produce a condensate from the normal state. Gorkov's singlet pair function [Waldram p160] allows for long-range phase coherence and so Eliashberg, working with both these functions simultaneously was able to apply standard perturbation theory to the superconducting state.

Eliashberg's equations describe a correction to the normal state frequencies $\Sigma(\omega)$ and the gap frequency $\Delta(\omega)$, and these reduce to the BCS equations in the weak coupling limit. They contain a parameter λ_M analogous to the BCS

coupling parameter NV, and the short range screened Coulomb repulsion, or Coulomb pseudopotential, μ^* [Waldram p216].

McMillan used the Eliashberg formalism to give his famous equation for T_C in the strong coupling limit [McMillan 1968, p217 Waldram]:

$$T_c = (\theta_D/1.45) \exp [-1.04(1+\lambda_M)/(\lambda_M-\mu^*(1+0.62\lambda_M))] \qquad (1.3).$$

The relative energies of the phonons and electrons set the weak coupling limit, $\Delta << k_B\theta_D$, and therefore a boundary on the utility of the BCS approximation. A useful method to distinguish the limit appropriate for a given superconductor is to observe the effect of the application of pressure on the superconducting transition. In the weak coupling limit a decrease in volume, associated with the application of pressure, is expected to decrease the superconducting transition. This should arise from the band broadening effect that reduces $N(E_F)$, which, according to *Equation 1.1* will reduce T_C. Any other behaviour therefore points toward a breakdown of the BCS approximation, and so a strong coupling mechanism.

1.3 Microscopic Sample Homogeneity

Further limits to the applicability of any theory are imposed by the homogeneity of the sample. The characteristic length for electrons in a normal metal is the mean free path, $\Lambda = v_F\tau$, travelled by an electron at the Fermi velocity (v_F) for the time between scattering events (τ). From the definition of $\rho = E/j$ and the current density j in a field E one may find that $\tau = m_e/\rho ne^2$. Considering the Fermi sphere and the volume of a single state in k-space the electronic density may be found $n = k_F^3/(3\pi^2)$ or simply $n = 3/(4\pi r_s^3)$, where r_s is the radius of a sphere containing just one electron. These results and the Fermi relation $v_F = (\hbar/m_e)k_F$ allow one to show that $\Lambda = (3\pi^2\hbar/e^2) \times (1/k_F^2) \times (1/\rho)$ and that $k_F = 1.92/r_s$. A useful change of units according to Ashcroft and Mermin gives $k_F = 3.63/(r_s/a_0)$ in $Å^{-1}$. Thus:

$$\Lambda = ((r_s/a_0)^2/\rho_0) \times 92Å \qquad (1.4)$$

where ρ_0 is the residual resistivity in $\mu\Omega$cm, and a_0 the Bohr radius.

The GL coherence length, $\xi(T)$, is a characteristic spatial distance over which a disturbance from the equilibrium value of the wavefunction decays, a characteristic length for the variation of ψ, a natural requirement within the GL perspective [Waldram p44, Tinkham p112]. This value diverges as T_C is approached from below [Waldram p47]. This length can be determined experimentally from the field dependence of the magnetisation, as discussed further in *Section 1.6*.

The comparison of this length with the mean free path will allow one to consider the homogeneity of the sample with respect to the superconductivity and thus define the material to be in the clean limit:

$$\Lambda >> \xi \qquad (1.5),$$

the dirty limit:

$$\Lambda \sim \xi \qquad (1.6),$$

or in the extreme dirty limit with $\Lambda << \xi_0$.

1.4 Superconductor/Normal Boundaries and the Type I/II Distinction

The Meissner state cannot remain rigid against all fields and there is a threshold beyond which a magnetic field will drive a superconductor normal. Two classes of behaviour may be distinguished when observing the field dependent magnetisation of a material in the superconducting state. The first type of superconductor to be discovered showed a first order transition like that of *Figure 1.1a* and this behaviour retains the title Type I superconductivity, consequently the second type of superconductivity, shown in *Figure 1.1b*, became known as Type II. Type I superconductivity is a first order transition and Type II is a second order.

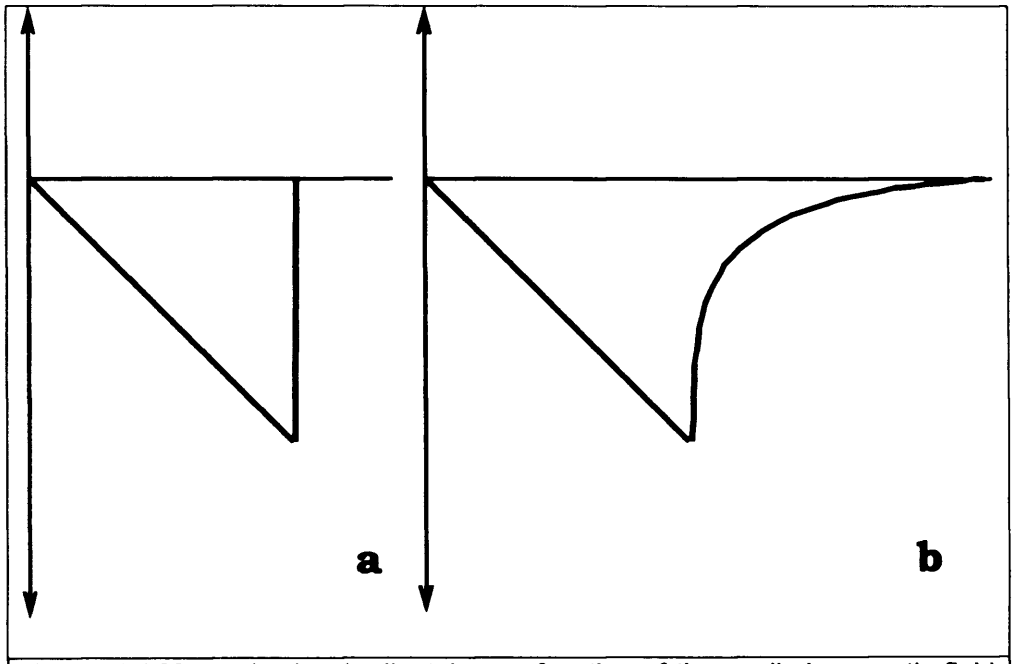

Figure 1.1 Magnetisation (ordinate) as a function of the applied magnetic field (abscissa) for a) Type I and b) Type II superconductors. The figure shows the ideal behaviour for each type of superconductor, with the Meissner state a) abruptly lost and b) gradually lost.

The form of the transition depends on the surface energy of the boundary between a normal region and a superconducting region within the material. If the surface energy of the boundary is positive then the boundary is minimized and the field penetrates catastrophically. However the boundary will be maximized if the boundary energy is negative, as in a Type II superconductor, so that flux will be quantized and the phase transition will be continuous.

The Ginzburg Landau theory defines the parameter κ as the ratio between the penetration depth, $\lambda(T)$, and the coherence length [Tinkham p133]

$$\kappa = \lambda(T)/\xi(T) \qquad (1.7).$$

Abrikosov showed that there is a particular value of the GL parameter, $\kappa = 1/\sqrt{2}$, which distinguishes Type I and Type II superconductors. Type II superconductors have $\kappa > 1/\sqrt{2}$. As the value of $\lambda(T)$ is not accessible from magnetisation measurements, it is useful that Brandt [Brandt 1997] has

shown that appropriately normalised curves can be used to estimate the value of κ. *Figure 1.2* consequently facilitates an estimation of the penetration depth from the measurement of M vs H.

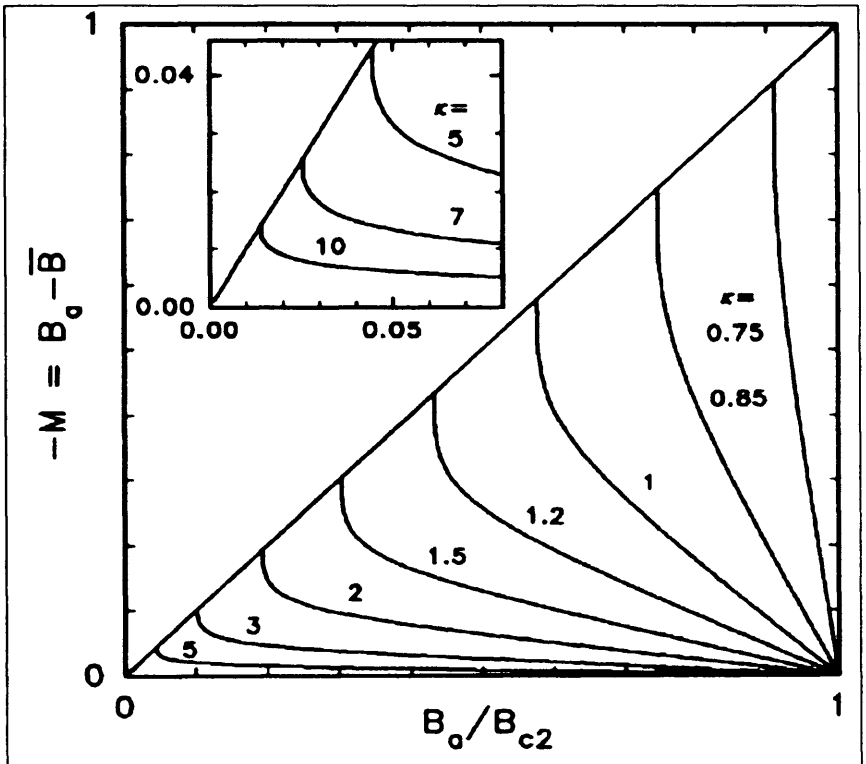

Figure 1.2 Brandt's reversible magnetisation curves for ideal vortex lattices in reduced units. For a discussion of the reduction of the units please refer to the original work [Brandt 1997].

1.5 Lower Critical Field, and the Energy per Flux Line

The Meissner state allows no penetration of flux into the sample, but as the density of flux lines around the sample increases at some lower critical field (H_{C1}) the first isolated flux lines can begin to penetrate into the sample. At the critical field the Gibbs free energy must have the same value whether the first flux line is in or out of the sample. Therefore a condition for the lower critical field may be derived that is dependent on the vortex line energy per unit length [Waldram p73]

$$B_{C1} = \mu_0 \varepsilon / \Phi_0 \qquad (1.8).$$

The shape of the magnetisation curve just above the first critical field, see *Figure 1.1b*, is due to the sharp rise in the number of flux lines entering in rapid succession. As the flux line spacing approaches λ they repulse each other, so that flux begins to enter more slowly with rising applied field. In the pinning free Type II superconductor the lower critical field is simply the minimum in the data.

In a real Type II superconductor measured in the laboratory the presence of magnetic flux pinning sites prevents flux lines from moving reversibly through the material, a complex matter discussed in detail by Waldram [Waldram p80]. Rather than a sharp rise in the number of flux lines entering in rapid succession throughout the sample at H_{C1}, the entry of the flux lines is restricted. Consequently the magnetisation curve is much smoother, and the minimum in the data may be higher than the true H_{C1}. The real behaviour will have a component such as that depicted by the thin red line in *Figure 1.3*. Flux may be pinned by impurities, defects, or dislocations in the material, these are all termed pinning [Tinkham p161] sites, and the number of them there are will push the behaviour of the superconductor further from the ideal.

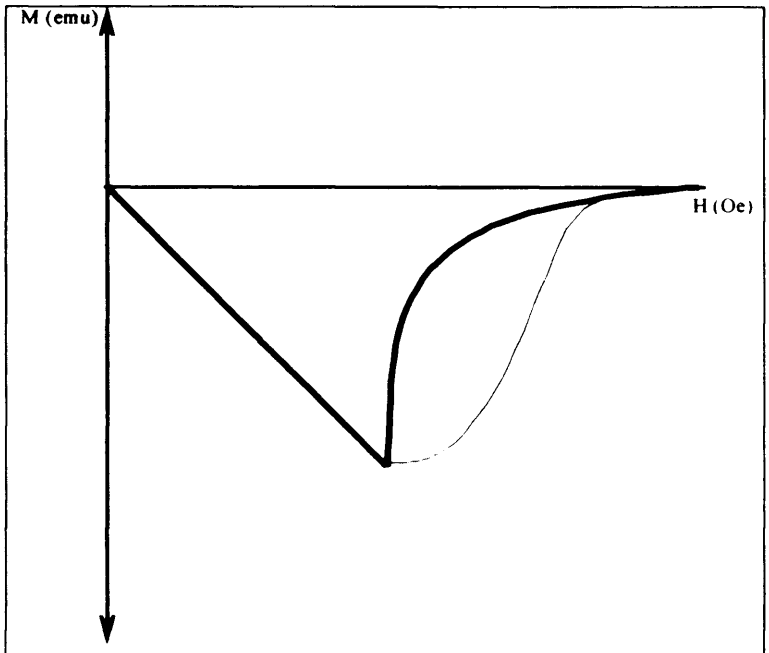

Figure 1.3 The ideal pinning free magnetisation of a Type II (thick blue) is in contrast to the observed behaviour. One component of the real magnetisation is due to pinning sites that cause a shape like that shown by the thin red line.

Geometric local magnetic field enhancement lowers the apparent critical field, as do weak links, otherwise known as Josephson junctions [Waldram p92]. The field is enhanced by edges and voids so that for a given applied field there may be local fields that are higher. These higher fields may penetrate where the applied field would not. Consequently flux penetration will occur at apparently lower fields. Josephson junctions, in contrast to edges and voids, lower the apparent critical field by allowing flux to penetrate the sample at lower fields [Tinkham p144]. The observed magnetic field behaviour of a Type II superconductor will combine the pinning effects with the field enhancement and Josephson effects to look more like the red line shown in *Figure 1.4*.

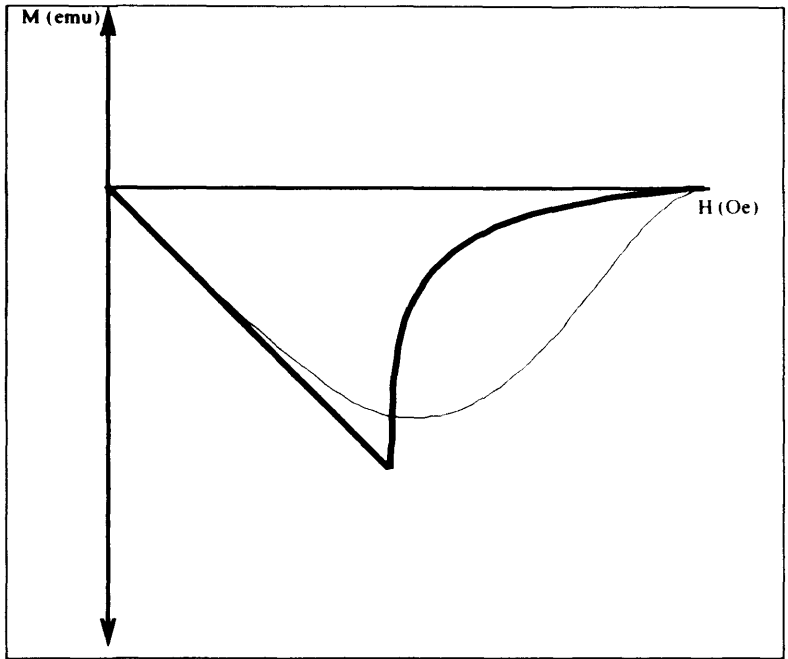

Figure 1.4 Ideal Type II (thick blue line) compared to the behaviour observed in the presence of pinning, geometric, and Josephson effects (thin red line).

1.6 Upper Critical Field and the Ginzburg Landau Coherence Length

At the upper critical field the wavefunction is very small and a linear version the GL equation may be used to solve for the minimum energy of the wavefunction. The linearised GL equation takes the form

$$(\tfrac{1}{2}m)(-i\hbar\nabla + 2eB)^2 \Psi = -\alpha\Psi \qquad (1.9).$$

This form is equivalent to the Schrodinger equation for a free particle of mass m and charge 2e in a uniform induced magnetic field, with an energy eigenvalue of α. The solutions to this equation are Landau levels [p260 Kittel] with energies

$$\alpha = \hbar^2 k_z^2/2m + (n+1/2)\hbar\, 2eB/m \qquad (1.10).$$

In order to find the lowest eigenenergy we set $k_z = 0$ and $n = 0$. The definition of the coherence length in the GL theory is [Waldram p59, Tinkham p110]

$$\xi(T) = \sqrt{\hbar^2/2m|\alpha(T)|} \qquad (1.11).$$

Thus combining *Equation 1.10* and *1.11* the highest value of B at which a value of Ψ still exists is

$$B = \hbar/2e\xi(T)^2 \qquad (1.12).$$

Since the flux quantum is

$$\Phi_0 = h/2e = 2.0678 \times 10^{-15}\ Tm^2 \qquad (1.13),$$

following Tinkham [Tinkham p129]

$$B_{C2} = \Phi_0/(2\pi\xi(T)^2) \qquad (1.14).$$

Thus the value of the critical field, where the magnetisation approaches zero, clearly demonstrates the physical situation. B_{C2} occurs as the packing of the flux lines reaches a critical areal density, with one flux quantum for twice the area of a circle of radius the coherence length. Any more field will cause the normal cores of the vortices to overlap significantly and completely suppress the magnetisation to zero.

For an anisotropic material with in-plane lattice vectors averaged and a distinct c-axis this must be modified for geometric reasons to give

$$B_{C2//c} = \Phi_0/(2\pi\xi_{//ab}(T)^2) \qquad (1.14(a)),$$

and

$$B_{C2//ab} = \Phi_0/(2\pi\xi_{//ab}(T)\xi_{//c}(T)) \qquad (1.14(b)).$$

Superconductivity is not limited by this value of field as a free surface of any given sample parallel to an applied field can act as a nucleation centre for superconductivity [Waldram p59, Tinkham p131]. If a boundary condition is applied during the solution of the linearised GL equation then a localised surface sheath solution arises at a higher field

$$B_{C3} = 1.695B_{C2} \qquad (1.15)$$

1.7 Cooper Pair Extent and its relation to the Rigidity of the Wavefunction

Pippard was the first to introduce the concept of a coherence length [Tinkham pp6,7], he used it analogously to the electron mean free path in an uncertainty relation argument to give a coherence length based on the Fermi velocity v_f and the transition temperature:

$$\xi_0 = ahv_F/2\pi k_B T_c \qquad (1.16),$$

where *a* is a constant.

In type II superconductors the spatial extent of a Cooper pair, the Pippard coherence length ξ_0, is related to the GL coherence length [Tinkham p129]. In the clean limit:

$$\xi(T) = 0.74\xi_0(1-t)^{-1/2} \qquad (1.17),$$

and in the dirty limit:

$$\xi(T) = 0.855(\xi_0\Lambda)^{1/2}(1-t)^{-1/2} \qquad (1.18)$$

where $t = T/T_C$. In the clean limit there is only clear validity for this relation near T_c, outside this range the effective value of $\xi(T)$ will depend on the sample configuration. In dirty superconductors this relation may remain valid far from T_C [Tinkham p113]. Thus by fitting the temperature dependence of the coherence length it is possible to see that the superconductor in question fits the GL theory, and to extract a value for the Pippard coherence length.

1.8 Parameterising the Anisotropy of a Superconductor

There are few superconductors without some degree of anisotropy. The first class of high anisotropy superconductors to be studied were thin films [Chaiken 1998], these were termed 2D as their thickness was less than ξ_0. Thin film superconductors and multilayers of 2D superconductor are at the extreme of anisotropic superconductivity.

The other type of anisotropic superconductors are metals like Nb, with anisotropic Fermi surfaces and consequent anisotropic coherence lengths. The model suitable for anisotropic 3D superconductors is the so-called effective mass model. The parameter describing the anisotropy in this case is

$$\Gamma^2 = m_{//ab}/m_{//c} = (H_{C2//ab}{}^2/H_{C2//c}{}^2) = \xi_{//ab}/\xi_{//c} \qquad (1.19),$$

so that the larger the ratio between the upper critical fields, the larger the anisotropy. This effective mass model requires an adjustment to the relation between the upper critical field and the GL coherence length [Waldram p271], such that

$$B_{C2//c} = \Phi_0/(2\pi\xi_{ab}(T)^2) \qquad (1.20)$$

and

$$B_{C2//ab} = \Phi_0/(2\pi\xi_{ab}(T)\,\xi_c(T)) \qquad (1.21)$$

The model appropriate to a 2D superconductor [Klemm 1992] gives a characteristic parameter

$$\gamma = 4(\xi_{//ab}(0) / (s/2))^2/\pi \qquad (1.22),$$

with the in-plane GL coherence length $\xi_{//ab}(0)$ and s the layer repeat distance. The γ parameter becomes smaller for more 2D materials.

1.9 Demagnetisation Corrections

B may not diverge when the magnetisation within a body diverges at the surface of that body, therefore there must be an equal and opposite divergence of the magnetic field strength [Blundell 2001]. In general this opposing divergence of H means that the field actually experienced by the material differs from the applied field far from the body, in the case of diamagnetic or superconducting samples the field is enhanced relative to the applied field, since the magnetisation is negative. In a uniformly magnetised material with volume $V(m^3)$, and moment $m(Am^2)$ the internal field is given by

$$H_{int} = H_{app} - N(m/V) \qquad (1.23)$$

The second term is the demagnetising field and N is a factor related to the geometry of the body in question. This factor is only well defined for a sphere (N=1/3); a long cylinder parallel to the field (N=0); a flat plate perpendicular to the field (N=1); and for ellipsoids [Osborn 1945]. The demagnetisation factors for an ellipsoid, as calculated by Osborn, are given for two different field orientations in Figure 1.5, with extrapolations to further values for different diameter to thickness ratios.

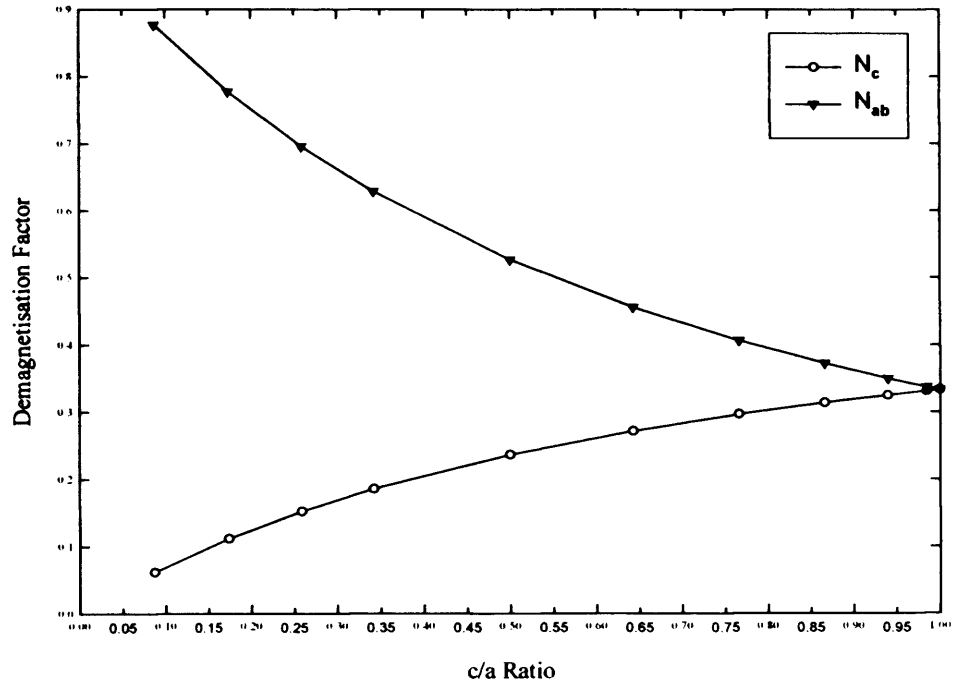

Figure 1.5 Demagnetisation factors for an ellipsoid, as extrapolated following the calculations of Osborn, are given for two different field orientations, Nc for H//c and Nab for H//ab, as a function of the aspect ratio of the sample with c the thickness and a the diameter.

Chapter 2

Graphite, Intercalates, Superconductivity

This chapter introduces the superconductivity of graphite intercalates, beginning with background information on graphite and graphite intercalates. The background consists of a brief introduction to the structure of graphite intercalates, with specific information on the electron and the phonon behaviour, and the electron phonon interaction, with special reference to rare earth and alkali earth intercalants where available. The field of superconducting graphite intercalates is surveyed with particular attention paid to identifying trends and representing the proposed explanations of the superconductivity in intercalates.

2.1 Graphite – The Archetypal Lamellar Structure

Graphite has a layered structure consisting of graphene sheets, flat layers of carbon atoms arranged at the vertices of hexagons 1.42Å on the side. These sheets are stacked 3.35Å apart, in such a way as to give only every other carbon atom of each hexagonal ring a carbon atom immediately above and below it. This structure, shown in *Figure 2.1*, is hexagonal graphite. Following Bernal [Bernal 1924], carbon atoms at the corners of the unit cell which have another atom directly above and below are termed type A, those with a gap (the middle of a hexagon) above and below are termed type B, the stacking has thus come to be referred to as ABAB [Cousins 2003].

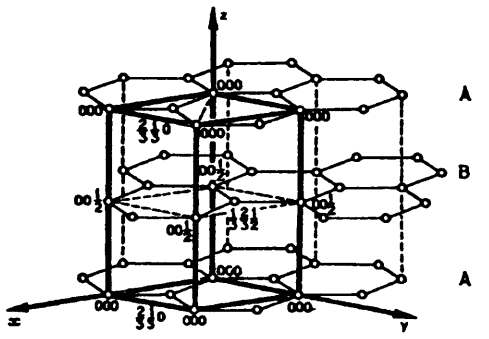

Figure 2.1 The structure of hexagonal graphite showing the unit cell and the crystallographic positions of the atoms in the unit cell. In this diagram the four different atomic sites can be clearly identified [Dresselhaus 1981].

Carbon 2s, $2p_x$, and $2p_y$ orbitals hybridize to form strongly coupled trigonal bonding and antibonding orbitals, giving 7eV/atom in-plane binding energy [Dresselhaus 1981, Cousins 2003]. These trigonal orbitals give rise to three bonding and three antibonding σ-bands. The remaining p_z orbitals form a single bonding and a single antibonding π-band, and these are degenerate at the six equivalent Brillouin zone corners through which the Fermi level passes (equivalent to the HKH line in the 3-dimensional graphite Brillouin zone shown in *Figure 2.2*). Graphene is therefore modelled as a zero-gap semiconductor.

Graphite has four carbon atoms per unit cell, due to the Bernal stacking, and double the number of π-bands. These bands are subject to a weak interlayer interaction that causes a small band overlap, giving rise to 0.02 eV/atom inter-plane binding energy, and the observed semi-metallic behaviour of graphite.

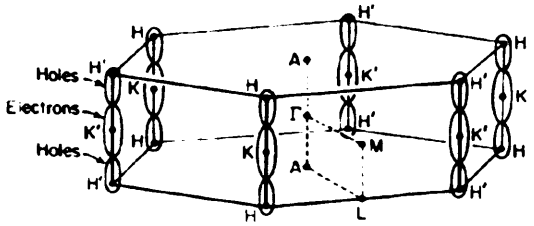

Figure 2.2 The Brillouin zone of hexagonal graphite, showing the high symmetry points and a schematic representation of the electron and hole pockets that lead to graphite being termed a compensated metal. [Dresselhaus 1981]

The full band structure of graphite may be calculated using the Slonczewski-Weiss-McClure (SWMcC) model [Dresselhaus 1981]. This model consists of 7 parameters which can be identified with overlap and transfer integrals within the framework of the tightbinding approximation. The three most relevant to the nature of the Fermi surface are: γ_2 which accounts for the interactions between atoms in next nearest layers and for the small π-band overlap of $2\gamma_2$ (~ 0.04eV), as well as for coupling between π- and σ-bands; γ_1 is the overlap of orbitals of Bernal type A carbon atoms in adjacent layer planes, it determines the width of the π-bands at point K, which is $4\gamma_1$; and Δ gives the difference in crystalline fields experienced by inequivalent carbon sites in layer planes, and determines the volume of the minority hole carrier pocket.

Figure 2.3 shows the construction of the band structure along the KH direction and the relevance of the SWMcC parameters [Dresselhaus 1981]. σ extends from the Brillouin zone edge radially into the plane perpendicular to the KH direction. For a fuller discussion of the band structure of graphite the reader is referred to the extensive review of Mildred and Gene Dresselhaus

[Dresselhaus 1981]. Additional empty band states not shown in the figures exist above the Fermi level constituting an interlayer band [Posternak 1983, Maeda 1988, Strocov 2000].

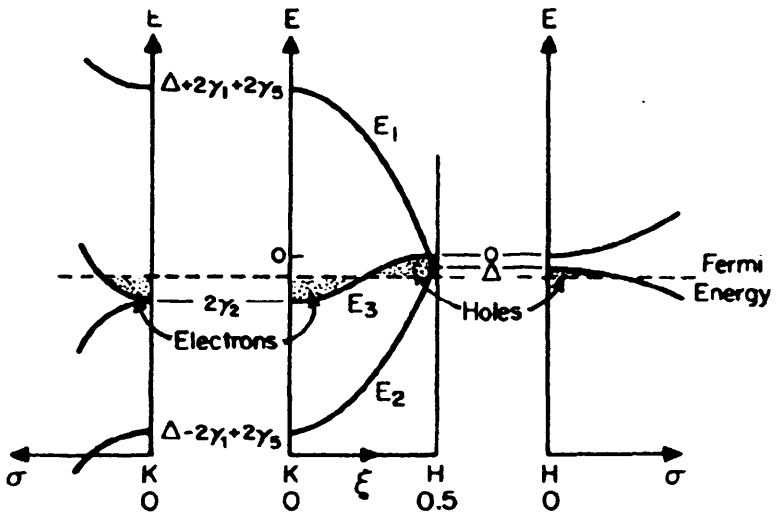

Figure 2.3 Part of the graphite band structure (left) showing the relevance of γ_2 and Δ to the shape of the Fermi surface (right) that is also depicted in *Figure 2* [Dresselhaus 1981]. σ extends from the Brillouin zone edge radially into the plane perpendicular to the KH direction.

2.2 Graphite Intercalation Compounds

2.2.1 Graphite Intercalation Compound Structures

Graphite intercalation compounds have a layered structure consisting of graphene sheets with guest atoms or molecules in the galleries between graphene layers. Carbon-carbon distances within graphene layers are likely to differ from graphene by much less than 1% [Pietronero 1981], whereas the interlayer distance may change by as much as 200% to accommodate the intercalant [Dresselhaus 1981]. The stacking sequence is sheared from the Bernal stacking of graphite to a stacking that brings graphene layers either side of an intercalant layer into identical registry, the stacking sequence may be as simple as AαAα, in C_6Li, or as complex as AαAβAγAδ, for C_8K, where

Greek letters denote intercalant positions. *Figure 2.4* shows the unit cell of an AαAβ stacked binary graphite intercalate.

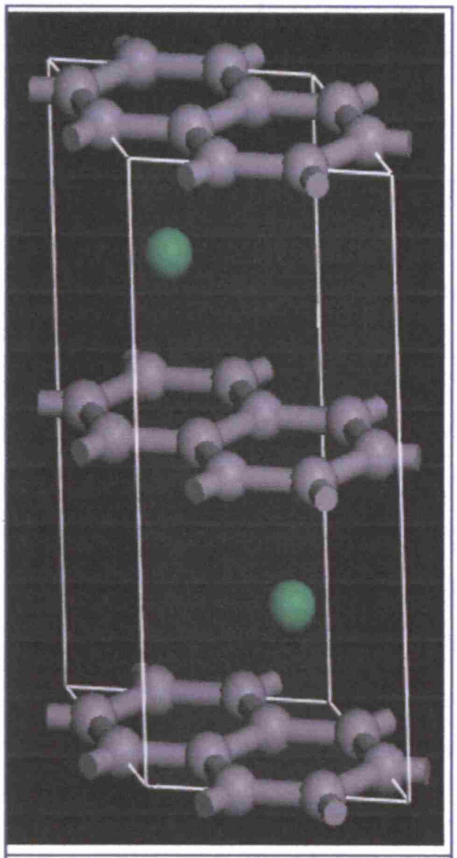

Figure 2.4 A C_6M AαAβ (M=metal) unit cell.

Graphite intercalates exhibit strong c-axis ordering called staging: the intercalant does not disperse equally between all galleries but tends to fill some galleries before others in an ordered manner. A stage *n* compound has *n* graphene layers between each guest intercalant layer. The staging is highly ordered as it is mediated by long range elastic interactions [Safran 1979]. The model presented by Safran is based on elastic dipoles, shown in *Figure 2.5*, that are repulsive within the same layer and attractive between layers. It is the competition between the electrostatic repulsion and the elastic attraction within a layer that causes the ordered structure of an intercalant within the galleries.

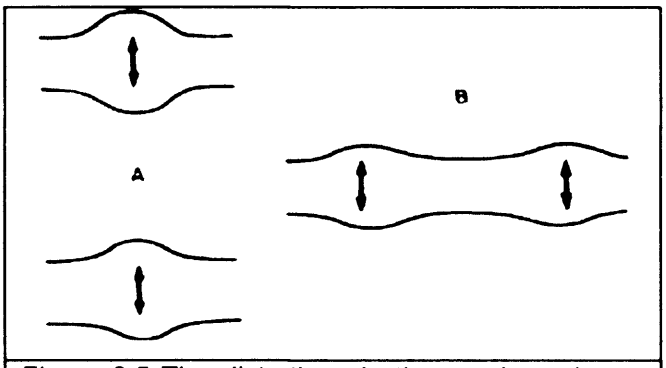

Figure 2.5 The distortions in the graphene layers surrounding an intercalant can be modelled as elastic dipoles in order to explain the ordering in graphite intercalate. Interlayer interactions, on the left, are repulsive and intralayer interactions, on the right, are attractive.

A combination of the electrostatic repulsion and the intralayer elastic attraction forms the intralayer ordering in the graphite intercalates. It is common to refer to the intralayer structure by reference to the intralayer spacing of the intercalants in units of the graphite unit cell length, 2.456Å. The intralayer structures are therefore summarised in *Figure 2.6* [Lindsell 1998]. It is the number of inequivalent intercalant positions in each of these in-plane structures that determines the stacking sequence.

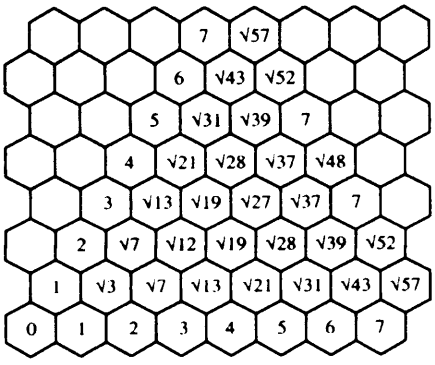

Figure 2.6 Intercalants form an ordered superlattice in the plane of the intergraphene space, or gallery. This image shows the position of an intercalant with respect to the origin for a given superlattice [Lindsell].

The standard non-idealised structural model of graphite intercalates is that of Daumas and Hérold [Dresselhaus 1981]. A staging transition is illustrative of this model, and is shown in *Figure 2.7* [Misenheimer 1983]. In the Daumas and Hérold model intercalation progressively lowers the number 'n' of graphene sheets between intercalant layers.

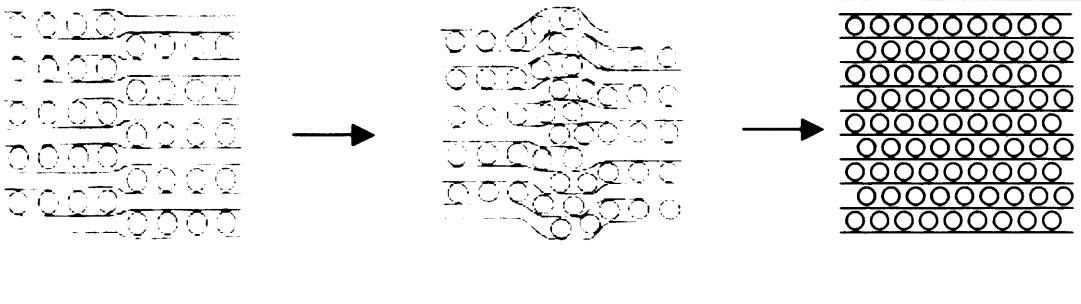

Figure 2.7 The circles represent intercalant and the lines graphene layers. On the left is a representation of two domains of stage 2 intercalation, with 2 graphite layers between each intercalant layer. In the centre is shown the process by which two stage 2 domains become a single stage 1 domain. On the right is shown a single stage 1 compound [Misenheimer 1983].

2.2.2 Electrons in graphite intercalates

Electron and phonon band structures for stage 1 graphite intercalates may be calculated by assuming a rigid band model [Dresselhaus 1981]. This involves folding the graphite bands into a smaller Brillouin zone appropriate to the new in-plane superlattice. *Figure 2.8* illustrates the effect of this folding, showing the in-plane structure determines the relative size and orientation of the intercalate Brillouin zone. Essentially the intercalate band structure is then calculated by a perturbation of the graphite band structure.

Graphitic π-antibonding bands have charge donated to them by the electron donor, and a cylindrical Fermi surface that undulates along the k_z direction forms from the electron pocket originally at the K-point. *Figure 2.9* shows a comparison of the lower band of the Fermi surface for C_6Li and C_8K showing the clear distinction. In the case of C_6Li the entire electron is transferred to the π band [Dresselhaus 1981] and no spherical region at the zone centre is apparent, whereas in C_8K there will be some charge that is not transferred to

the π band and a spherical region of electron Fermi surface is apparent at the zone center [Wang 1991].

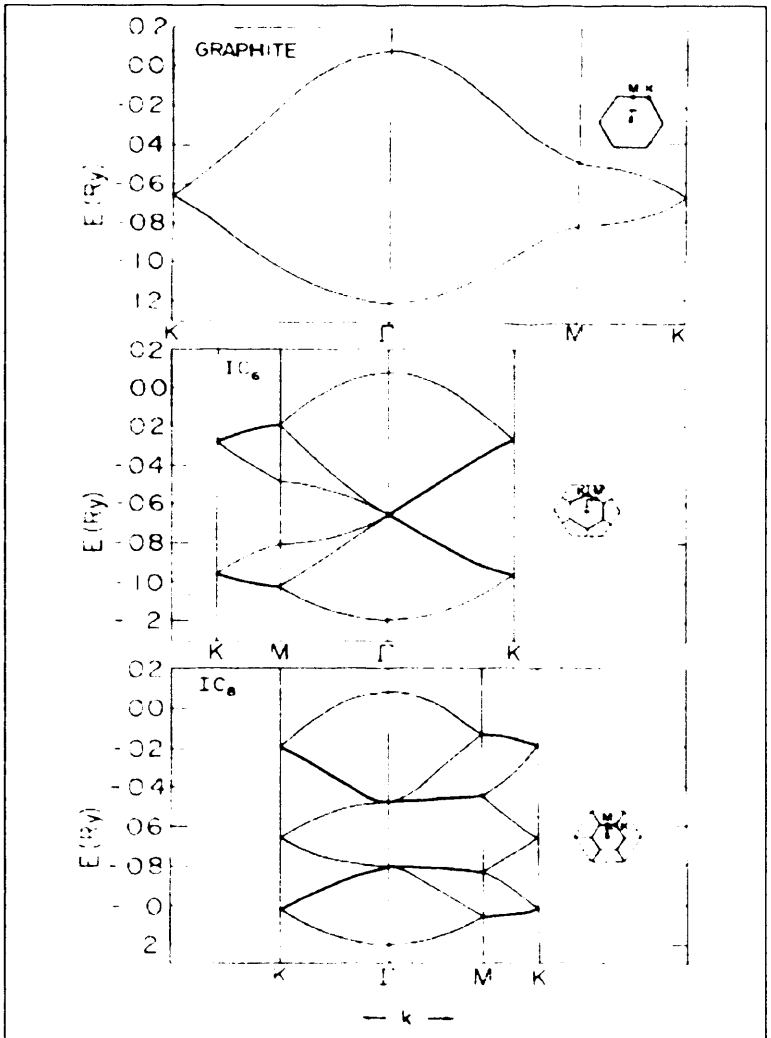

Figure 2.8 This figure illustrates the effects of zone folding on the π band structure of graphite (upper image) when it is folded into the Brillouin zone for a √3x√3 in-plane structure (labelled IC_6) and the 2x2 in-plane structure (labelled IC_8) [Holzwarth 1978]

Disagreement arose between different calculations over the location and character of the remaining charge in the C_8K system. According to early calculations on the C_8K system by Inoshita the charge not located in the π-band is 4s like and nearly isotropic [Inoshita 1977], later Ohn et al. calculated the charge transfer from first principles [Ohn 1979], where Inoshita et al had determined it empirically by fitting to the C_8K Knight shift, the two sets of calculations were essentially in agreement. Strong disagreement arose when

DiVincenzo and Rabii calculated that there was no nearly isotropic K(4s) band [DiVincenzo 1982]. Posternak et al. then asked the question 'is the electron confined between the two layers, or is it already bound to a single graphite layer?' [Posternak 1983] and using the Local Density Approximation predicted the unoccupied interlayer state in graphite, later confirmed experimentally [Maeda 1988, Strocov 2000], and calculated partial filling of it in the case of C_8K and C_6Li.

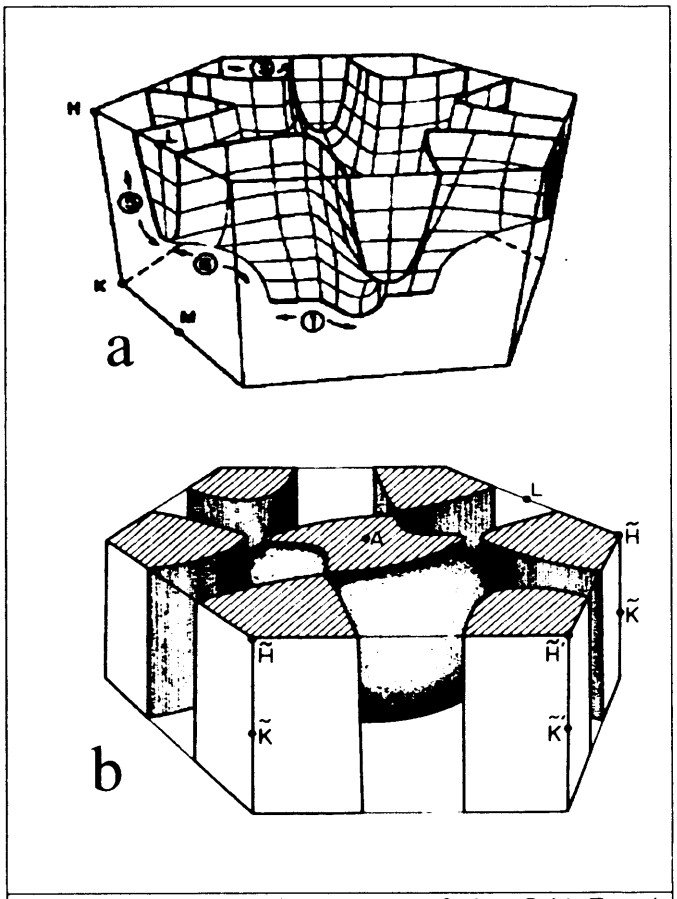

Figure 2.9 a) The lower part of the C_6Li Fermi surface [Dresselhaus 1981] and b) the lower part of the C_8K Fermi surface calculated by a semi-empirical tight-binding scheme [Wang 1991].

Preil et al. measured X-ray Photoemission Spectra (XPS) of C_8K and showed that the valence band is not like the potassium 4s states but rather like graphite states. They concluded that if an s-like band exists then only 0.04e/K is contained within it [Preil 1984]. Koma et al. used Low-energy Electron Energy Loss Spectroscopy (LEELS) to prove that the charge density has the features of the interlayer state, different to K(4s), in addition showing that the

Ohn et al. model fits the LEELS data [Koma 1986]. They also showed that the Ohn band structure is consistent with the XPS of Preil. Finally Wang et al. measured the dHvA effect for C_8K and found two frequencies, one corresponding to an isotropic portion of Fermi surface and the other to a cylindrical Fermi surface, they also found that there was a nearly full ionisation of the K [Wang 1991].

A study of the band structure of rare earth intercalates was made in Dresden by Molodtsov et al [Molodtsov 1996], using Angle Resolved Photoemission Spectroscopy (ARPES), and Local Density Approximation calculations. Their chosen set of atomic orbitals included the 5*d*, 6*s*, and 6*p* states as well as the C 2*s* and 2*p* states but not the 4*f* electrons, which, it was assumed, were localized in a non-magnetic divalent state. The interlayer state was unoccupied according to their calculations, being well above the Fermi energy in the rare earth intercalates. They showed that the rigid band model gave a reasonable qualitative description, however a more elaborate approach was adopted to account for the hybridisation between the RE 5d states and the graphite π states, which was leading to an intense structure at the Fermi level in the ARPES results.

2.2.3 Phonons in graphite intercalates

A summary of the types of phonon modes in graphite intercalates is given by Zabel [Zabel 2001], and is reproduced in *Figure 2.10*. Phonon studies of graphite intercalates have been hampered by a lack of large single crystals. However the behaviour of the breathing modes, or [00q]L phonons is not dependent on the ab-plane disorder present in large HOPG based intercalate samples. In addition the ripple or layer-bending [q00]T modes (combination of breathing and shear in *Figure 2.10*) are not strongly affected by the [HK0] powder average in HOPG, being well defined due to the elastic isotropy of the layers. Studies of other modes are rare.

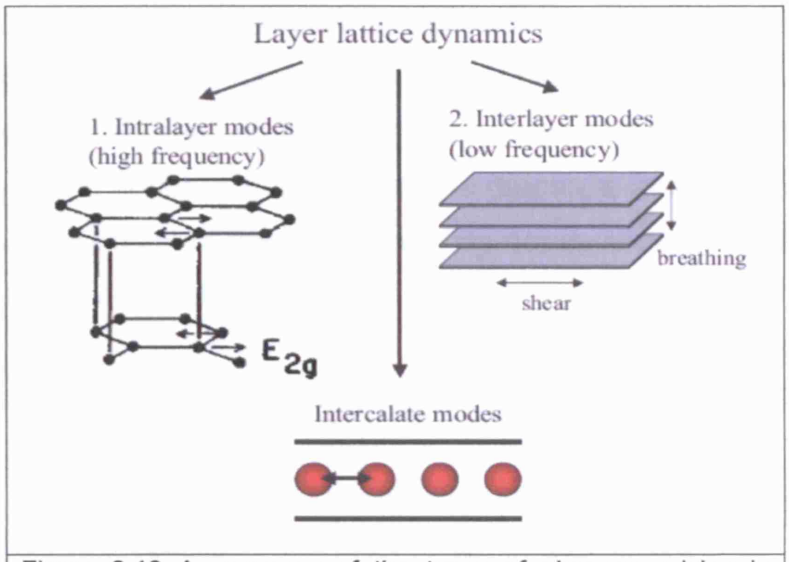

Figure 2.10 A summary of the types of phonons arising in graphite intercalates, ripple modes are a combination of shear and breathing modes [Zabel 2001].

Observations, shown in *Figure 2.11*, of the [00q]L modes in C_8K, C_8Rb and C_8Cs, using inelastic neutron scattering [Zabel 2001] demonstrate the form of the mass dependence of the interlayer breathing modes. The mass of the intercalate layer relative to the graphene layer is the dominant effect in the case of these alkali-metal intercalants. The frequency gap at the A-point (refer to the Brillouin zone in *Figure 2.2*) between the acoustic and optic branches shrinks as the mass of the intercalant approaches that of 8 carbons. In the case of Rb, a mass of 85 is to be compared to the mass of C_8 of 96.

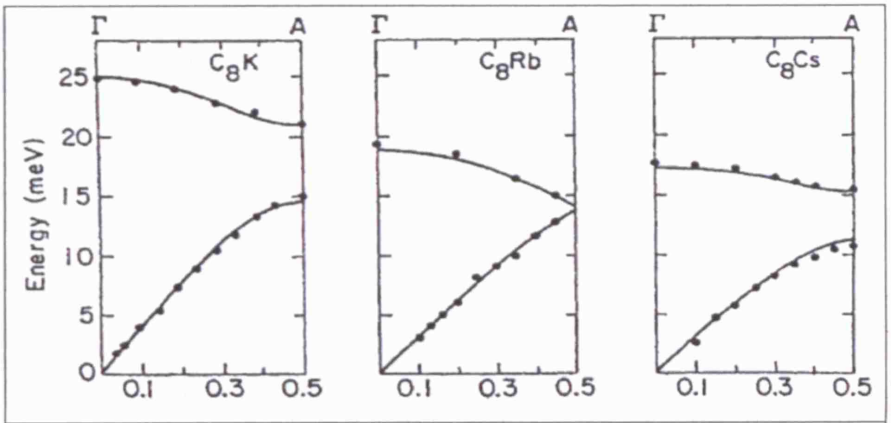

Figure 2.11 The [00q]L modes in, from left to right, C8K, C8Rb and C8Cs. The wavevector extends from 0 at the Γ point to 0.5 at the A point, from the zone centre to the zone boundary. The data was collected from inelastic neutron scattering experiments [Zabel 1982].

Figure 2.12 shows [00q]L modes in the left hand panels, and gives the [q00]T bending modes for the same three alkali metal intercalates in the right hand panels. Zabel et al. showed that the dispersion of the acoustic branch is dependent on the combined stiffness of the graphene and intercalant layers, whereas the dispersion of the optic branches depends on the stiffness of the individual layers [Zabel 2001].

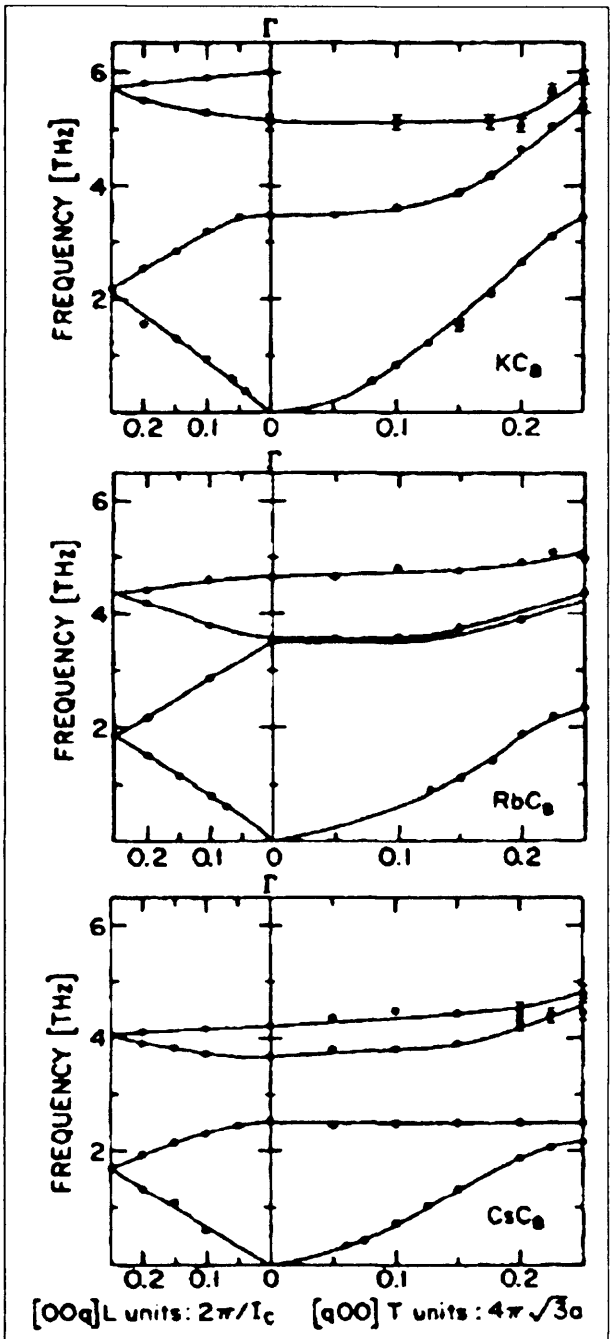

Figure 2.12 The [q00]T modes for the three alkali metal stage 1 intercalates are shown in the right hand panels, with the [00q]L modes in the left hand panels [Zabel 2001]

The in-plane intercalant modes can be studied as a phonon density of states (PDS), with thermal neutrons, and these results are shown in *Figure 2.13*. In the alkali-metal intercalates this yields a double peak structure that scales with the square root of the intercalate mass [Zabel 2001]. A model accounting for the observed PDS predicts the upper peak value to be close to the plasma frequency.

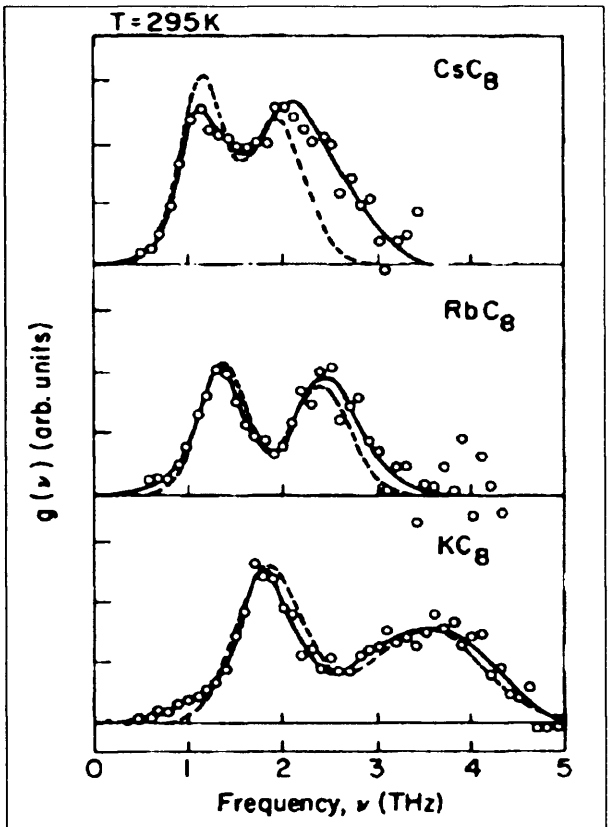

Figure 2.13 The phonon density of states for the in-plane intercalant modes of C_8K, C_8Rb and C_8Cs.

Lang et al. used a seven force constant model to predict the dynamical behaviour of the graphite intercalate family [Lang 1994]. Though they only show that their band structure accounts for a few of Zabel's data points for C_6Li. They usefully provide calculations for the Debye temperature for various intercalates including C_6Ca (585K) and C_6Yb (472K), though for C_8K the value calculated is 25% greater than the experimental value, for C_8Cs 6% smaller, for C_6Li 2% larger, and for graphite 0.6-2.6% depending on which experimental value is chosen. This lack of consistency in the error may point to a problem in the model.

2.3 Superconducting Graphite Intercalates

2.3.1 Early Motivation – Conduction Electron Manipulation

Early work demonstrating the convenient manipulation of the electron distribution in graphite by electron donor intercalation [Hennig 1951, 1952] led to the proposition that in some cases this might lead to superconductivity [Hennig 1952]. The authors of this proposal studied samples of polycrystalline artificial graphite exposed to an ammonia solution of the desired intercalant, and subsequently washed in water. Neither resistance measurements nor magnetometry showed superconductivity down to 1.25K in Br, K, Ca, B, ammonium, or bisulphate graphite compounds synthesised in this way. More than a decade later Hannay et al. [Hannay 1965] made a study using a vapour transport technique dating to 1926 [Fredenhagen 1926] involving only the metal vapour and pyrolytic graphite. This study demonstrated for the first time that alkali-metal graphite intercalates C_8M (M = K, Rb, Cs) superconduct.

Since 1965 nearly 20 superconducting graphite intercalates have been discovered. None of these have been with electron acceptor intercalants [Dresselhaus 1981, 2001]. The transitions in binary graphite intercalation compounds synthesised at ambient pressure have been consistently less than 0.2K [Kobayashi 1979, Belash 1990], ternary alkali amalgam intercalates reach higher, to just under 2K [Vogel 1981], and high metal concentration binary intercalates synthesised under high pressure conditions have given unconfirmed highs of 4.2K [Avdeev 1990]. *Figure 2.14* demonstrates that the only trend in transition temperature has been an increase in T_C with metal concentration; achieved with high pressure synthesis of binary alkali intercalates [Belash 1990].

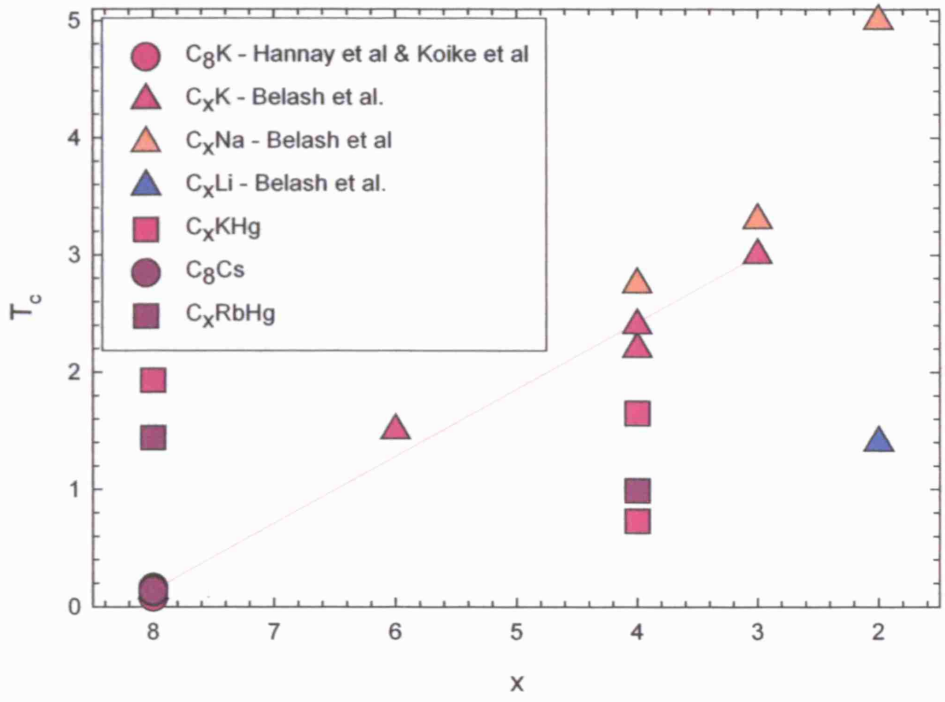

Figure 2.14 All superconducting graphite intercalates discovered so far contain electron donor species, and have the form CxMM. This graph shows T_C as a function of C stoichiometry (x). Circles represent ambient pressure synthesised intercalates. Triangles represent pressure synthesised. Squares represent ternaries with form C_xMHg. For yellow M=Li, for orange M=Na, for pink M=K, for progressively darker pinks M=Rb and Cs. The lines are simply a guide to the eye that identifies the only reported trend [Belash 1990] in graphite intercalate superconducting transitions, an increase in T_C with metal concentration.

2.3.2 C8K – The Prototypical Superconducting Graphite Intercalate

Alkali metal intercalates remain the easiest to synthesise and C_8K is the easiest of these materials to work with having a balance between intercalant mobility and metal reactivity. Consequently C_8K remains the most studied of graphite intercalates. It has quite a complex stacking structure, but its stage ordering is nonetheless typical of a stage-1 intercalate, with 1 atomic layer of potassium between each graphene layer. It can also be prepared easily with higher stages of n, with n layers of graphite between each layer of intercalate [Nixon 1968]. A single sandwich of graphite-potassium-graphite is expanded to 5.4Å from the 3.354Å of the graphite host. Of the possible in-plane

structures shown in *Figure 2.6*, C_8K takes the 2x2 60° superlattice structure, where 2x2 is relative to the graphite unit cell in-plane dimension. As a typical intercalate C_8K forms an excellent introduction to the superconductivity of graphite intercalation compounds, though as the reader will discover there are significant differences across the intercalates.

C_8K has displayed a broad range of transition temperatures. Kobayashi demonstrated conclusively that the transition temperature is highly dependent on the graphite preparation by measuring the transition in graphite powder, Grafoil, and HOPG, finding transitions of 0.08K, 0.125K, and 0.15K respectively [Kobayashi 1979]. This showed why Hannay et al. were not able to measure a consistent transition, since they were working before the advent of high quality HOPG [Hannay 1965]. Even so Koike et al reported a range of transitions between 0.128K and 0.198K for samples synthesised from HOPG, whereas Belash et al. also measured a single transition at 0.14K. The transition temperature is highly variable dependent on the type of graphite used as host, but HOPG can be used to produce a more consistent transition temperature with greater magnitude than other graphites.

Hannay et al noted the strong anisotropy in the upper critical fields of C_8K, recording, at 0.32K, $H_{C2}//ab$ = 160G and $H_{C2}//c$ = 730G for an intercalate made with excess potassium and $H_{C2}//ab$ = 25G and $H_{C2}//c$ = 250G for an intercalate made with stoichiometric amounts of potassium [Hannay 1965]. However it was the re-examination using low frequency a.c. magnetic susceptibility and electrical resistivity measurements by Koike et al that showed the interesting angle dependence of the superconducting critical fields of the C_8K [Koike 1980].

C_8K displays Type I behaviour when the field is applied H//c but type II behaviour with the field applied H//ab. The thermodynamic critical field for H//c, 6Oe at 90mK, remains constant to about 50° when, for angles <50° an upper critical field begins to appear. Within about 15° of H//ab the angular dependence of the upper critical field fits a simple geometric argument [Morris 1972] for the angular dependence of an anisotropic type II superconductor,

requiring only the relative effective mass in the two directions as well as the angle. On the basis of this so-called effective mass model Koike et al deduce a critical angle of 25°. This is where the value of H_{C2} calculated with the model becomes less than the experimentally measured value of the critical field H//c. This crossover from a positive (Type-I) to a negative (Type-II) surface energy for different angles in C_8K is unique amongst layered systems.

Given the anisotropy of the intercalates it is obvious to test the applicability of the Josephson-coupling model, parameterised by Equation 1.22. Koike et al. found that the anisotropy in C_8K was not strong enough to be described by the Josephson model and consequently rather than 2D C_8K is a 3D superconductor with a high degree of anisotropy.

Koike et al. also consider the value of the coupling constant under the BCS approximation and using the strong coupling equation of McMillan [McMillan 1968]. For C_8K they find that NV = 0.14 and that $0.31<\lambda_M<0.33$; these values are very similar to those of Ir (NV=0.12 and λ_M=0.34) and much smaller than those of Hg (NV=0.35 λ_M=1) and Pb (NV=0.39 λ_M=1.12). Consequently Koike *et al* concluded that C_8K is in the weak coupling limit.

Koike et al C_8K is a highly anisotropic, but 3D, superconductor. It is in the weak coupling limit and has a small value of the GL parameter varying between 0.32 and 1.5 depending on the field orientation. Type I behaviour is exhibited H//c and Type II H//ab.

It should be noted that both Koike *et al* and Kobayashi *et al* informed Iye and Tanuma in private communications that they could not find superconductivity in C_8Cs or C_8Rb down to 0.06K and 0.09K respectively.

2.3.3 C_8KHg & C_8RbHg – Stage 2 Alkali Ternaries

Subsequent discovery of the superconductivity of C_8KHg by Alexander et al. added the alkali-mercury ternaries to the class of superconducting intercalates [Dresselhaus 1981]. This material was found to superconduct at

1.9K, and once again it was Sei-ichi Tanuma's group who made significant efforts to measure its behaviour [Koike 1981]. This material has a triple layer of metal atoms between graphene layers, with a stacking CKHgKC, as shown in *Figure 2.15*. However C_8KHg is a stage 2 compound and will have two graphene layers between each metal triple layer.

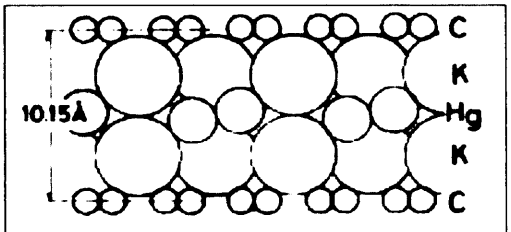

Figure 2.15 The structure of a single potassium-mercury metal layer between two graphene layers [Iye 1982].

Koike et al. used AC magnetic susceptibility measurements to determine transition temperatures of 1.7K and 1.9K in two different samples. They studied the upper critical field and were able to model this on the basis of the effective mass model, and whilst they found that the γ-parameter (*Eqn 1.22*) value for the Josephson model was too large to represent a 2D system, they did find a large effective mass anisotropy of Γ~30. Despite this much larger anisotropy the amalgams appear to be Type II superconductors in both field orientations.

Subsequently superconductivity was also found in C_8RbHg at 1.44K [Iye 1982].

2.3.4 C_4KHg and C_4RbHg – Stage 1 Alkali Ternaries

Though superconductivity was initially not seen in the Stage 1 alkali-mercury ternaries this was surprising and Tanuma's group kept looking and in 1982 they reported the first observation of superconductivity in these compounds [Iye 1982]. It is interesting to note that the Stage 1 compounds have a lower transition temperature than their stage 2 equivalents, with C_4KHg having an

average transition (over three samples) of 0.77K and C_4RbHg an average of 1.14K.

The upper critical fields of the stage 1 amalgams are also described using the effective mass model. The anisotropy is once again large, but not as pronounced as for the stage 2 materials, both C_4KHg and C_4RbHg having $\Gamma \sim 10$, and the materials are Type II in both field orientations.

2.3.5 Models of superconductivity in graphite intercalates

Takada developed a model for superconductivity based on the interaction between electrons and c-axis polar phonons and associated plasmons [Takada 1978 & 1982]. This model conceives the C_8M system as consisting of $C^{-f/8}$ and M^+ ions, where f is the level of charge transfer to the π^* bands, and f=1 being complete charge transfer. Takada found that in a low carrier density system polar optical phonons, where planes of metal atoms vibrating in phase, oscillate out of phase with planes of carbon atoms vibrating in phase, can contribute significantly to superconductivity. In the case of graphite intercalates he later showed that the acoustic polar phonon can bring about an electric polarisation field only when $f \neq 1$, and that this electric polarisation can contribute to superconductivity. In his model the absence of superconductivity in C_6Li is thus elegantly explained by a complete transfer of the valence electron to the π^* band. The anisotropy of the gap function and thus the coherence length was ascribed in his model to the anisotropy in the electron phonon interaction. The results of this model gives $H_{//ab}/H_{//c} \sim 1.5$.

Radi Al-Jishi points out that $\xi_\perp/\xi_{//} \sim 1.5$ is significantly smaller than the observed values in C_8K ($\xi_\perp/\xi_{//} \sim 5$) and C_xKHg (>10 for stage 1 and >20 for stage 2). Al-Jishi presents a different model for alkali-metal intercalates [Al-Jishi 1983 & 1992] that explains the large anisotropy on the basis of the anisotropy in the C_8K electronic band structure [Inoshita 1977, Ohno 1979, Koma 1986]. Partial charge transfer to the π-band of the valence electron leads Al-Jishi to consider an effective superposition of the carbon π-band and the metal s-band and thus to base the model on coupling of Cooper pairs on

different Fermi surfaces [Suhl 1959]. In this model the electron-phonon interaction is assumed isotropic, and the only anisotropy introduced is from the anisotropy of the band structure. Thus the claim that the anisotropy of the band structure is the main factor contributing to the anisotropy observed arises from a circular argument and is not on a firm physical basis. The Al-Jishi model does however explain the absence of superconductivity in C_6Li by the requirement for both bands, of which only the π^* are available in C_6Li.

2.3.6 Pressure and Graphite and its Intercalation Compounds

Graphite and its intercalation compounds respond to hydrostatic pressure anisotropically. The contrast between weak interlayer and strong intralayer bonds leads to pressure variations in the ab-plane that can usually be neglected in comparison to variations in the interlayer spacing. The in-plane compressibility of graphite, usually assumed shared by intercalates, is $k_{ab} = 1 \times 10^{-4}$ kbar^{-1} and the c-axis compressibility some 28 times larger, *Table 2.1* [Clarke 1984]. Hydrostatic pressure on graphite and graphite intercalates is consequently near-uniaxial.

Compound	k_c (10^{-3} kbar^{-1})	Technique
C_6Ba	0.8	INS
C_6Li	1.16	INS
C_8Cs	1.58	X-ray
C_8Cs	1.74	INS
C_8K	2.09	INS
C_8Rb	2.24	INS
$C_{24}K$	2.7	INS
$C_{12}Li$	2.72	INS
Graphite	2.77	X-ray
$C_{24}Rb$	2.85	INS
$C_{24}Cs$	3.27	INS
C_4KHg	4.4	INS

Table 2.1 Measured compressibilities for graphite and graphite intercalation compounds taken from [Clarke 1984] and [Fischer 1987].

Graphite has a delicate electronic structure and is highly sensitive to the effects of hydrostatic pressure. A very small ambient pressure band overlap means that there will be relatively large changes to the electronic structure from small volume changes. Experimentally the Fermi surface has been observed to swell on application of pressure with an increasing carrier concentration of $d\ln N/dP = 37 \times 10^{-3} kbar^{-1}$ [Anderson 1967] and it has been confirmed from deHaas-vanAlphen measurements that extremal cross sections of the Fermi surface and effective mass increases are approximately linear up to 12 kbar [Clarke 1984].

In comparison to the electronic structure it is believed that the change in the phonon spectrum is small, but experiments of resistivity at low temperatures have not been carried out to determine the effect of pressure on the electron-phonon interaction [Clarke 1984].

2.3.7 Application of pressure to C_8KHg

Application of hydrostatic pressure is observed to reduce the superconducting transition temperature in C_8KHg [Yeh 1982]. The superconducting transition was found to decrease linearly with increasing pressure at a rate dT_c/dP = -0.65 K/GPa. The data shown in *Figure 2.16* are taken on two cycles of pressure increase and decrease, showing that the behaviour is reversible. The gradient is similar to typical values for three-dimensional elemental superconductors such as tin, aluminium, and lead [Buzea 2004].

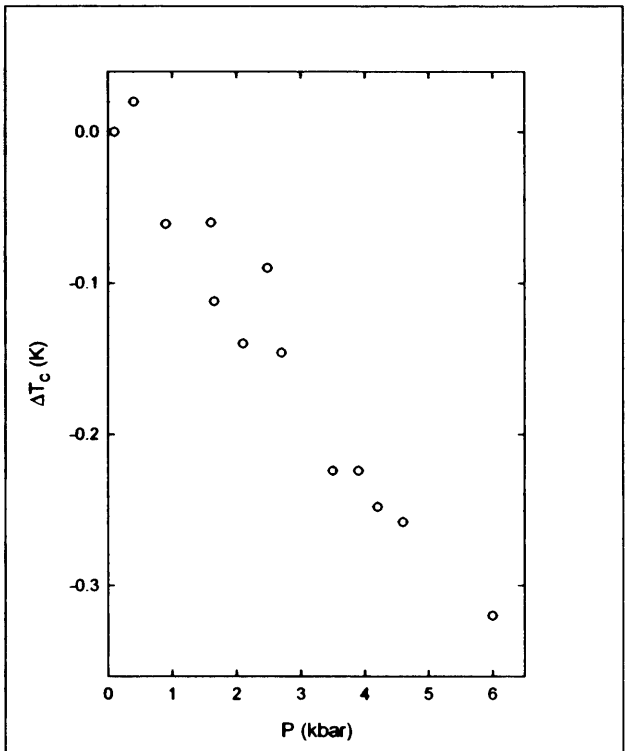

Figure 2.16 Superconducting transition temperature in C_8KHg, as a function of applied pressure [Yeh 1982]. The superconducting transition decreases linearly with increasing pressure at a rate dTc/dP = -0.65 K/GPa. The data is taken on two cycles of pressure increase and decrease, showing that the behaviour is reversible.

Observations made on C_4KHg, *Figure 2.17*, show an initial increase and distinct sharpening of T_c at 0.8kbar, followed by a linear decrease thereafter

of dT_c/dP = -0.5 K/GPa. A pressure cycle causes the transition to be narrowed, leading to the suggestion that either a first order phase transition or a disorder order transition is occurring at about 1kbar [DeLong 1983]. Clarke et al are of the opinion that the explanation in terms of a phase transition is more plausible based on the reproducibility and reversibility of the data. As an alternative a charge density wave (CDW) state, by analogy to transitions metal dichalcogenides (TMDCs), may be invoked for the large positive low pressure dT_c/dP that changes abruptly, becoming smaller and negative at greater than 0.8kbar [DeLong 1983].

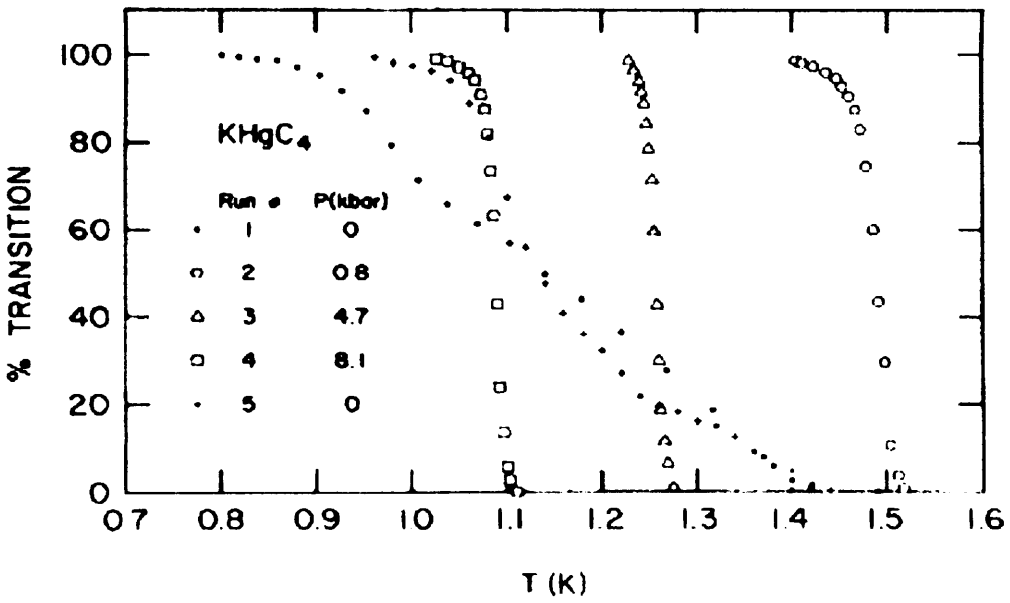

Figure 2.17 Normalised magnetization for C4KHg, shown at various pressures. The data shows an initial increase and distinct sharpening of Tc at 0.8kbar, followed by a linear decrease thereafter of dTc/dP = -0.5 K/GPa. On removal of pressure there is a significant change in the form of the ambient pressure transition, though not in the onset value. The sample that DeLong and Eklund (DE) use has two steps in it, after the pressure cycle the first step is quite strongly suppressed. DE therefore suggested a first order phase transition at about 1kbar or a disorder to order transition with a small amount of hysteresis.

2.3.8 Application of pressure to C_8K

Figure 2.18 shows the effect of small pressures on the form of the transition in C_8K. The data shows that there is a growth of a second phase with a much higher transition temperature. In a second sample, *Figure 2.19*, using a larger

clamp cell the authors claim to see a first order phase transition, which appears to be irreversible. Solin has suggested a change in stacking sequence may be the phase transition observed [DeLong 1982]. X-ray diffraction has also shown that reversible changes of stage can be induced by pressure in the $C_{24}K$ system, accompanied by changes in the in-plane density of the potassium [Clarke 1980].

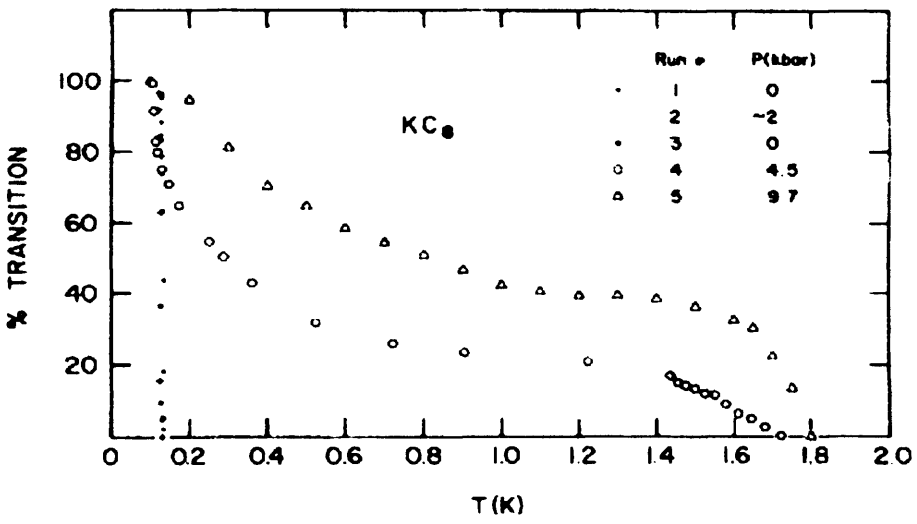

Figure 2.18 The effect of small pressures on the form of the transition in C_8K. The data shows that there is a growth of a second phase with a much higher transition temperature. 100% Transition refers to maximum diamagnetic signal, and 0% Transition to the normal state.

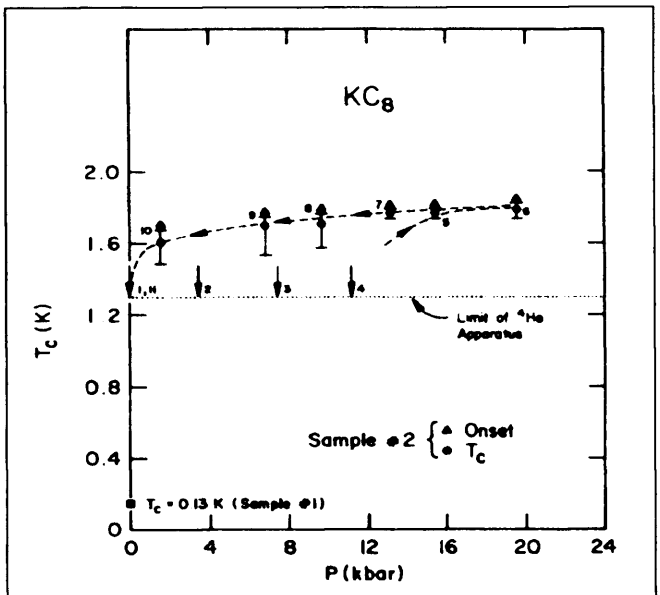

Figure 2.19 The same study as *Figure 5.3*. The data appear to show an irreversible phase transition between 11 and 16kbar.

2.3.9 High Pressure Synthesised Alkali Intercalates with High Metal Concentration

In the late 80s Avdeev et al discovered that higher metal concentration C_xK (x=6, 4) compounds had superconducting transitions at higher temperatures than C_8K. Samples synthesised with stoichiometries C_6K and C_4K were cooled to liquid nitrogen temperatures at 1GPa before the samples were recovered, this prevented the samples from degrading to C_8K and potassium.

C_6K was found to superconduct at ~1.5K, the transition is sharp and indicates a single phase material [Avdeev 1990], Avdeev et al point out that this transition is the same as that observed by DeLong et al as shown in *Figure 5.4*. Avdeev et al. therefore concur with DeLong et al. in concluding that the higher transition temperature for the C_8K under pressure is due to a structural phase transition to C_6K. The hysteresis is consistent with phase changes reported by John Fischer's group in 1985 [Bloch 1985], wherein they observed a $\sqrt{3}$ x $\sqrt{3}$ structure, typical of C_6M stoichiometries, appearing at about 15 kbar that did not revert to the original 2 x 2 structure until the pressure was fully released. C_4K however displayed a diffuse superconducting transition beginning at 5.5K.

Belash *et al* followed on from this work, studying lithium and sodium pressure synthesised intercalates, as well as potassium [Belash 1990]. Their work is hampered by the difficulties of synthesis, stability and characterisation of these materials. For instance in the case of the lithium series both C_3Li and C_2Li were characterised only by the disappearance of X-ray reflections from the C and Li starting components and distinct different superconducting transitions. In the sodium series the same is true of C_2Na, and likewise C_3K. The C_3Na was identified with 2 phases, and only C_6K was found to have a characteristic single phase X-ray pattern, with a lattice spacing equivalent to C_8K. These ambiguous and incomplete characterisations nonetheless, when coupled with magnetometry and resistivity measurements, identify a distinct trend for an increase in superconducting transition with metal concentration. Additionally, the C_xK system critical field behaviour was studied, and it was shown that the materials can all be characterised with the effective mass

anisotropy model. Furthermore Γ decreases with metal concentration, with C_3K having nearly isotropic behaviour Γ=1.1, as shown in *Table 2.2*.

Stoichiometry	T_c (K)	ξ//c (nm)	ξ//ab (nm)	Γ
C_8K	0.155	175	810	4.63
C_6K	1.5	50.1	100.2	2
C_3K	3	20.9	23.2	1.11

Table 2.2 The transition temperatures, coherence lengths and Γ values for the concentration series studied by Belash et al [Belash 1990].

Chapter 3

Synthesis, Structure and Morphology

This chapter discusses the synthesis of graphite intercalation compounds. In particular it focuses on the alkali-earth and rare-earth binaries. A detailed report on the novel synthesis technique developed for the production of C_6Yb and C_6Ca is given. The structure and morphology of these samples are demonstrated through the use of X-ray diffraction (XRD) and scanning electron microscopy (SEM) with energy dispersive analysis of X-rays (EDAX).

3.1 Intercalating Metals – Thermodynamic Stability and Microscopic Process

The microscopic process of intercalation is not well described in the literature, however assessing the thermodynamic stability is not dependant on this process and a basic assessment of the viability of a compound can be made upon the energy difference between the compound and its constituents. In the case of the graphite intercalates a first consideration may include the energy change when: widening the inter-graphene distance; taking an electron off the donor; placing an electron in the graphite; and letting a positive intercalant ion fall into the Coulomb potential of the graphite host. This latter is related to the charge on the ion, in coulombs, and the ionic radius. There are more complex factors that can be brought in but more importantly beyond the consideration of the energy stability of the compound there are a number of empirically determined factors of importance that will be discussed, along with what is known about the microscopic process of intercalation.

Van der Waals forces have long been known to dominate the interlayer interaction in graphite [Richardson 1977]. The presence of this weak bonding between the graphene layers allows a variety of more than 100 intercalants. In order to describe the Van der Waals force the Lennard Jones potential

$$U(x) = -A/x^6 + B/x^{12} \qquad (3.1)$$

was introduced. It is from this potential and the parameters in Table 3.1 [Girifalco 2000] that the energy cost of opening the lattice to accommodate the donor ion may be computed.

	$A\ (eV x Å^6)$	$B\ (eV x Å^{12})$
Graphene-Graphene	15.2	24.1×10^3

Table 3.1 The Lennard-Jones parameters for the graphene-graphene spacing, as published by Girifalco et al. [Girifalco 1976].

It is accepted that charge transfer drives the initial stages of intercalation [Dresselhaus 2001], but to translate this into the simple picture of assessing thermodynamic stability some measure of the ease with which charge transfers must be sought. The first ionisation energy is a measure of the energy required to remove one electron from one mole of gaseous atoms or ions. It consequently provides a basic measure of how easily charge transfer can occur. *Figure 3.1* gives the first ionisation energies of a variety of metallic elements. The electron affinity of graphite, defined as the energy gained in bringing an electron from the vacuum level to the bottom of the antibonding pi* band, is 4.6eV [Kelly 1981], equivalent to 444kJ/mol. The difference between this energy and that required to remove the electron from the ion is the energy required (or gained) for the transfer of one electron.

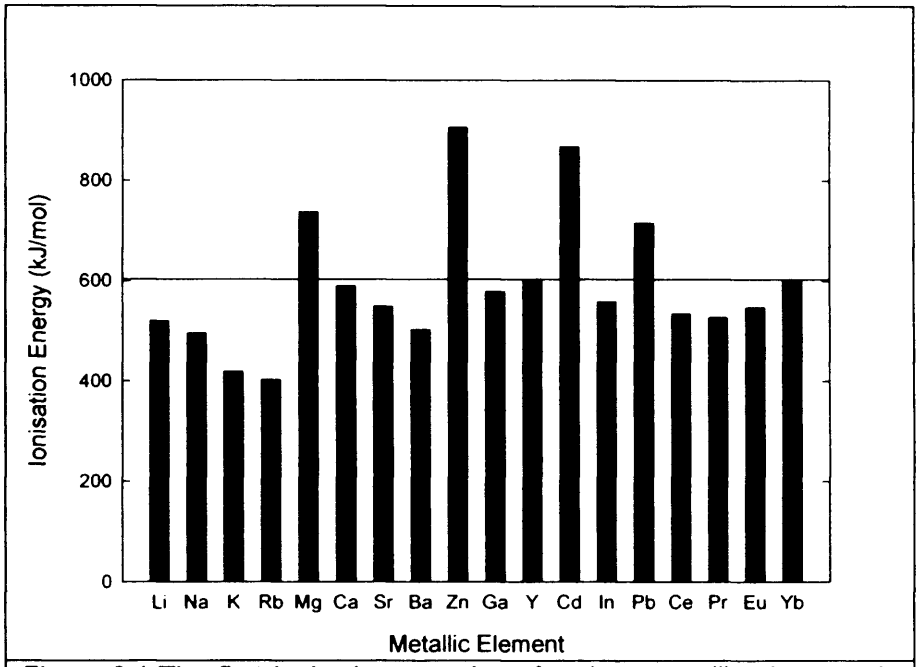

Figure 3.1 The first ionisation energies of various metallic elements in units of kJ/mol. The horizontal line corresponds to the value of ionisation energy for ytterbium.

The intercalation of metallic donor species by vapour transport is reliant upon the vapour pressure of the metal, under the pressure and temperature conditions imposed, having greater than some threshold value [Dresselhaus 2001]. A metal with a saturated vapour pressure equal to the external pressure will sublime [Lide 1994]. Under a vacuum of 2×10^{-6}mbar the pressure of metal vapour will be close to the saturated vapour pressure once equilibrium is reached. The saturated vapour pressure may be calculated

according to Alcock *et al* [Lide 1994] and *Figure 3.2* shows vapour pressure curves for various metallic elements.

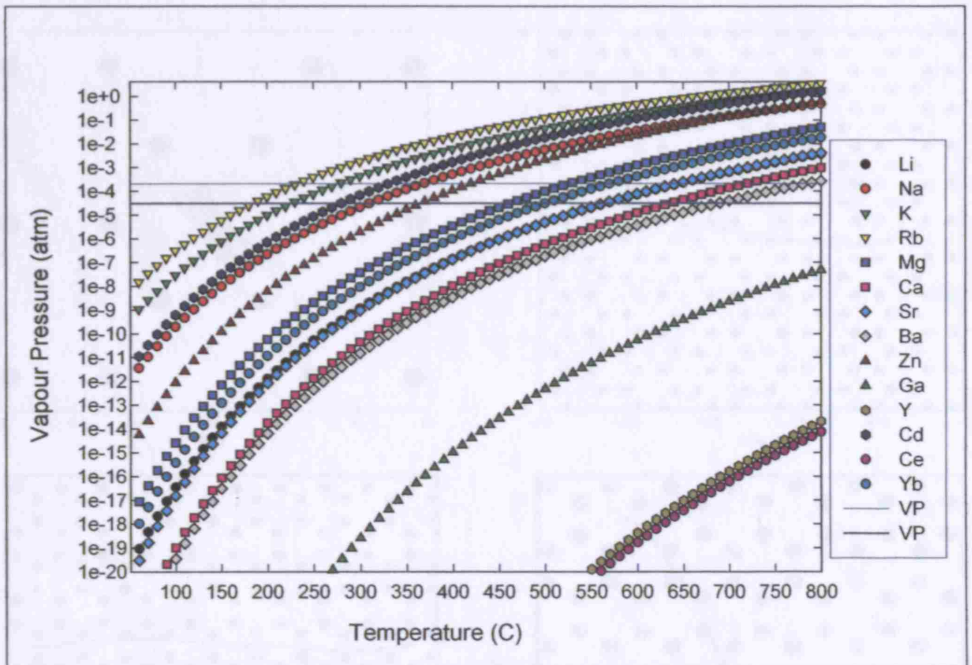

Figure 3.2 The vapour pressure, in atmospheres, of various metallic elements. The horizontal lines give the approximate range of vapour pressures at which the intercalation of ytterbium is successful.

Nucleation of intercalate phases is dependent on the availability of entry points for the intercalant ions into the graphite interlayer spaces. Dislocations and stacking faults in graphite thus play an important role in the nucleation of the intercalate phase. The precipitation of intercalant ions at dislocations is also important for preventing deintercalation on pressurisation [Clarke 1980].

Diffusion rates of intercalant ions are dependent on the temperature of the host graphite, the size of the ion, the mass of the ion, and the ion concentration [Kamitakahara 1985]. The most important of these is the host temperature, as there is evidently a threshold temperature below which an intercalant ion of given mass and size is not mobile. This has been shown theoretically in the case of C_8K and $C_{24}K$ using finite temperature first principles molecular dynamics [Bernasconi 2002]. *Figure 3.3* shows images depicting the path of a potassium atom through the graphite lattice. The potassium is immobile at 373K in stage 1 C_8K, though mobile in the more dilute $C_{24}K$. Between 373K and 573K the ion becomes mobile, demonstrating

the presence of a threshold in the mobility, even at the higher concentration C_8K.

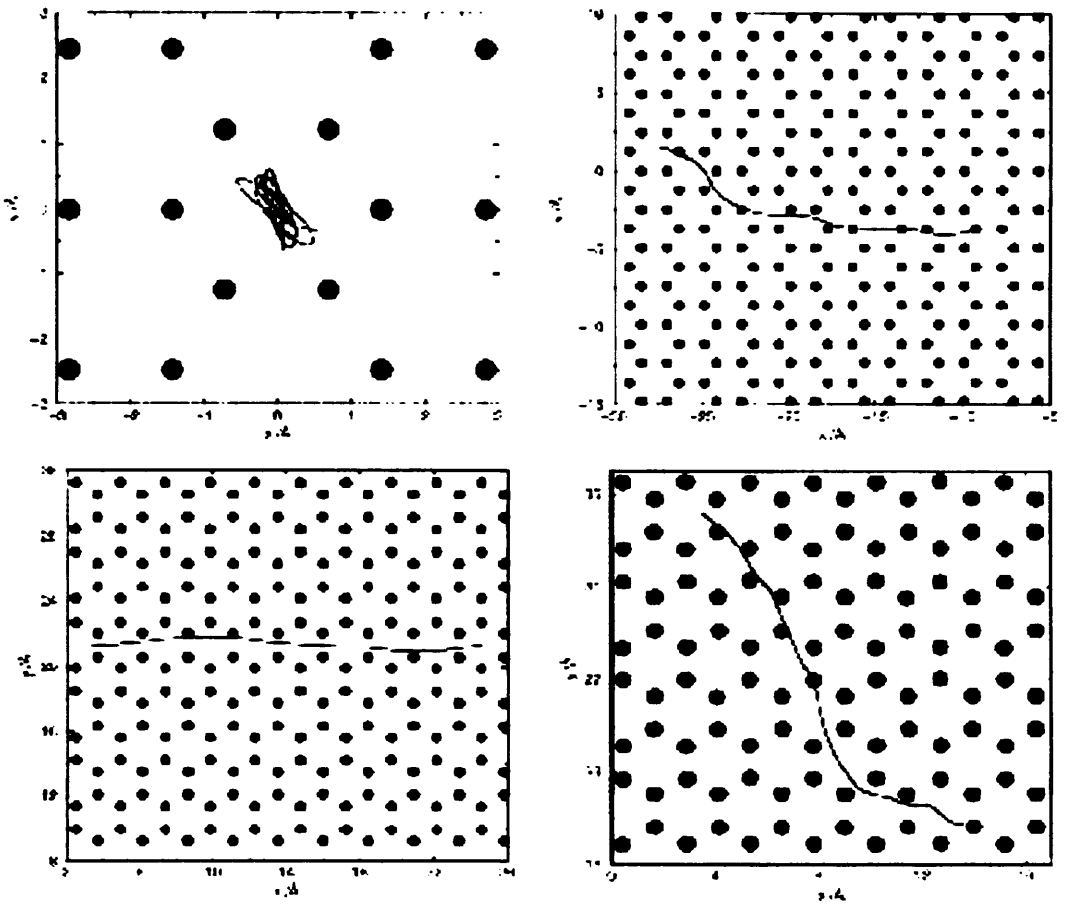

Figure 3.3 Potassium ion trajectories computed by Bernasconi and Madden with first principles molecular dynamics [Bernasconi 2002]. The images on the left show trajectories at 373K, those on the right 573K. The top images are for stage 1 C_8K and the bottom for stage 2 C24K.

3.2 Intercalating Divalent Metals

The difficulty of preparing divalent donor graphite intercalates is widely recognised and has hampered the pursuit of a full understanding of these materials. Intercalation of metallic donor intercalants is most commonly undertaken by two-zone vapour transport, a technique dating back to 1926 [Fredenhagen 1926]. This technique is subtly different to the novel method that is presented in this chapter.

The synthesis of binary earth metal intercalates was first carried out in 1976 when Girifalco and Montelbano reported a BaC_8 composition [Girifalco 1976]. Then in 1979 and 1980 a group at Nancy University led by Profs. Lagrange and Herold reported the insertion of alkali-earth and rare-earth metals into graphite [Guerard 1979, El-Makrini 1980].

The field of graphite intercalate synthesis has long been led by the Nancy group. They were the first to report observing the intercalation of lithium into graphite [Hérold 1955, Guérard 1975]. The ground breaking C_6Li compound led to a surge in intercalate research, eventually fulfilled in the use of C_6Li in rechargeable batteries still studied by a large number of researchers today [Tarascon 1993, Broussely 1997, Song 2004]. Energy generation has remained the principle focus of this group since its earliest days. Their stated motivation for the dry synthesis of divalent metal intercalates came from the possibility of better in-plane electrical conductivity than is achievable with monovalent alkali metals [El-Makrini 1980].

The Nancy group synthesised C_6Yb, C_6Eu, and C_6Ca, amongst others, by the direct action of metal vapour on HOPG or SCG in a single temperature zone ampoule and by the compaction and heating of mixtures of metal and graphite powders [El-Makrini 1980, Guérard 1980]. They do not specify clearly the details of the synthesis method, though they give temperatures and lengths of exposure for the compaction work [El-Makrini 1980, Guérard 1979]. Initial work at UCL sought to reproduce the work of the Nancy group using the single temperature zone ampoule [Gallagher 2001].

C_6Eu was heralded as an intercalation system with magnetic ions interacting little with their host [Kaindl 1983] and during the first half of the 1980s its magnetic behaviour was studied extensively [Suematsu 1981]. Following motivation by this unique opportunity for growing magnetic structures [Shikin 1995] photoemission spectroscopy was used to carry out studies of the electronic structure of lanthanide intercalates in Dresden [Molodtsov 1996].

In Dresden *in situ* vapour deposition and subsequent annealing allowed large single crystal flakes (Madagascar) to be surface intercalated sufficiently for LEED and ARPES experiments. Some samples synthesised in this way were studied during work preparatory to this thesis. These proved insufficiently intercalated to show 00l structure or magnetic or superconducting behaviour in bulk characterisation techniques such as laboratory x-ray diffractometry or SQUID magnetometry. This demonstrated that there was only surface intercalation in these materials.

The *in situ* methods of the Dresden group stimulated a revision of the single temperature zone ampoule method. The authors revised method was to use a two zone tube, with metal in one and HOPG in the other. This allowed the deposition of metal to be followed by annealing, by first heating one end and then the other. This revised method gave promising results but the yield seemed to be limited by the amount that could be deposited at one time. A method of simultaneous deposition and annealing was therefore sought.

This technique is detailed in *Section 3.3* and is subtly different from the standard two-zone vapour transport technique. The two zone technique is typically employed to control the staging of the alkali metal intercalates and has always involved the HOPG being hotter than the vapour end, it is a standard for alkali-metal intercalate synthesis but has never previously been discussed with respect to the heavier metals.

3.3 Synthesis of C6Yb and C6Ca

The difficulty of the intercalation of divalent metals, recognised in the literature, has been compounded by a lack of detail in the reporting of intercalation processes. The literature on graphite intercalates is often confusing, incomplete or even contradictory due to differences in sample preparation procedures [Chaiken 1998]. In general graphite intercalate sample quality, stage and homogeneity are all sensitive to small changes in the synthesis process [Dresselhaus 2001]. It is therefore of great importance that the fine details of sample synthesis and handling be conveyed.

3.3.1 Working Materials

Graphite is available in many types, these are summarised in *Table 3.2*.

Type	Form	Typical size	Production Method
Single crystal	Flakes	~1mm diameter ~1/10 thickness	Separated from limestone rocks
Kish	Several large single crystals		Crystallization of carbon from molten steel
HOPG	Polycrystalline	~1micron crystallites with near perfect c-axis alignment	High temperature hydrocarbon cracking, annealing, pressure
Grafoil	Sheet	~1mm thickness	exfoliated and rolled

Table 3.2 This table gives brief details of the various types of graphite available. The common name, the form, typical sizes, and a note on the production method.

In this study samples have been prepared from highly oriented pyrolytic graphite (HOPG) of Grade ZYA, supplied by GE Advanced Ceramics [GE Quartz Europe]. The grade refers to the mosaic spread of the crystallites with respect to the c-axis, ZYA is the best grade with a mosaic spread of 0.4° ± 0.1°. The mosaic spread is the full width half maximum of the rocking curve on the 002 diffraction peak. The purity of the HOPG supplied is 99.99% pure carbon, with a total metallic impurity content of 10ppm.

In this case HOPG is the best compromise, it has plenty of sites at which the intercalant can enter at the surface as well as the edges so that intercalation of samples can be achieved more readily through the process of nucleation whereas the process of diffusion and long range order formation is better in pure single crystal graphite.

Single crystal graphite often contains magnetic impurities such as iron that could be detrimental to the studies performed, HOPG on the other hand is man made and can be synthesised carefully to give high purity samples. Additional motivation to employ HOPG comes from the finding of the Nancy group that the action of vapour is more successful on bulk samples than on powders [Guérard 1979], and that in the case of C_6K the HOPG samples yielded the cleanest transitions at the highest temperatures [Chaiken 1998].

3.3.2 Graphite Preparation

The HOPG used was supplied with dimensions 12mm * 12mm * 2mm. It is found that the most waste free way to cut this into appropriately sized pieces is to cleave the HOPG once or twice to give 12mm * 12mm pieces with a thickness approximately 2/3mm. It is something of an art to cleave these crystals cleanly. Cleaving consistently may be achieved by making a very light nick with a scalpel blade at the corner of the crystal and, whilst very delicately transversely working the blade to extend the nick in the plane, allow the whole edge of the blade to come to *rest* against the edge of the crystals such that the plane of the blade is parallel to planes of the HOPG. As the blade comes to rest a *light pressure* will reveal if the HOPG will then cleave easily. This can be repeated to give thicknesses down to about 0.5mm, it is easier to cleave a thin layer off a thick piece and consequently the number of cleavings from one crystal is limited.

Once a 12mm * 12mm square has been cleaved it may be precut into strips of just over 1mm wide. This may be done most efficiently by lightly scoring a line into the surface of the HOPG and repeating this scoring until the blade passes through the HOPG. If this sawing technique is not used a great deal of wastage can result as the HOPG is prone to cracking.

From these strips bars a little larger than (3mm x 1mm) and squares a little larger than 1mm x 1mm can be sawn in the same manner. As these pieces are sawn it is often observed that cleavings may occur naturally, this may be used to advantage in reducing the thickness of the HOPG pieces if

necessary. It should also be noted that the thickness achieved at this stage has a minimum associated with the need to further cleave the sample later in the process.

The precut pieces of HOPG will now have edges with dislocations and ab-plane and c-axis crossing visible to the naked eye. It is possible to more easily cleave these pieces to achieve thinner HOPG pieces if necessary, though in some cases the edge will be too spoilt to achieve this.

Once the pre-cut pieces of HOPG are prepared they are air-abraded to provide well-defined edges with open interlayer spaces and minimised short-circuiting between the layers. It is important that the interlayer spaces are easily accessible to the intercalant and it was observed in the early stages of the study that c-axis like behaviour could be observed in ab-plane resistivity measurements. The abrasion is carried out with 50micron SiO_2 glass beads blasted at the sample with air at a pressure of 4psi. In order to shape the samples appropriately dies have been cut from PEEK. Ideally the dies would be very long and the abrasion carried out from some distance to achieve a square edge. However this is constrained to be about 150mm long, by the size of the box that houses the blasting nozzles. The die must be held vertically over the pre-cut HOPG, it must be held delicately as the HOPG pieces are exceedingly slippery. It is possible to hold them with your fingers at this stage. At all times the HOPG pieces are not under the die one must attempt to hold them between the finger and the cutting board. The cutting board is simply a small square of PTFE.

Once the edges are prepared in this way the HOPG pieces must be checked for glass beads under a microscope. Then, using scotch tape, they can finally be cleaved to give good surfaces. The most effective way of achieving this is to place the pieces on a clean, smooth, hard surface and to lay the tape over them and then peel it back flat against the surface. This ensures that only the top surface is removed rather than the entire piece cleaved, it also prevents

the piece being lost as it is lifted by the tip and flicked off by the peeling motion. The pieces are checked under a microscope.

3.3.3 The Metal and Its Preparation

Metals were prepared in an MBraun high purity argon glove box. In order to achieve the cleanest metal surface possible the pieces of appropriate size for the tubing are cut inside the glove box using tungsten carbide heavy-duty wire cutters. The metal should only be prepared at the last moment before being placed in the tube. The pieces must be not so small as to pass through the dimpled section of the tube but small enough to pass down the narrower of the two tube inner diameters (ID).

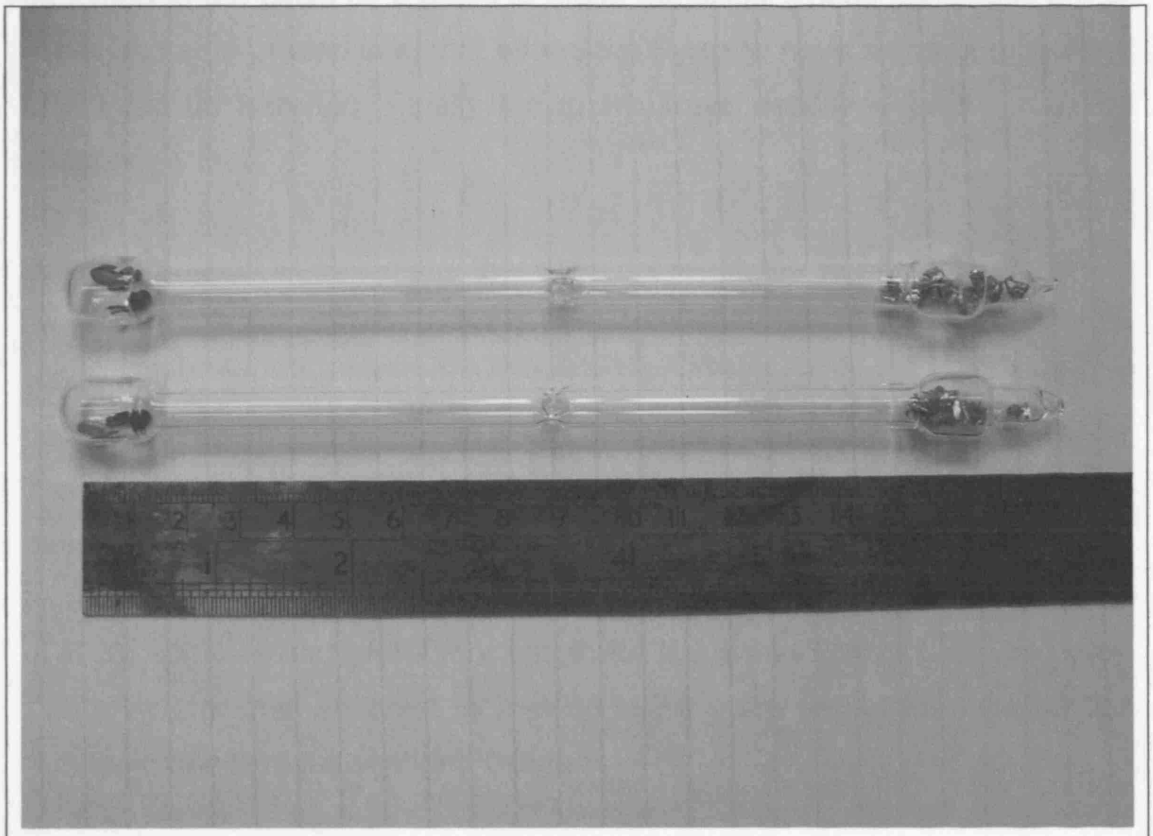

Figure 3.4 Ampoules ready for heat treatment. The HOPG can be seen at the left hand end of the tubes, with the dimples located at the middle of the tube, and the metal in the right hand end. When the seal is made the metal is at the dimple. These tubes are of a slightly different length to that quoted in the text.

3.3.4 Ampoule Preparation

An ampoule, see *Figure 3.4*, with a bulb at each end is prepared from quartz glass to contain the vapour transport process. Quartz glass is used, as it is easier to seal under vacuum than Pyrex, having a higher softening point. Pyrex, or borosilicate glass, has a softening point of 821°C [UDEL 2006], whereas that of quartz is 1683°C. Using a higher softening point glass allows higher outgassing temperatures and reduces the number of tube failures during the preparation process.

The processing requires various outgassing stages and consequently the tubes are fitted with a DN25KF flange, supplied by Caburn. The flange must be joined to the glass by a glass to metal transition. These transitions are of Pyrex and so a graded seal that allows the Pyrex to have a quartz tube fitted to it must be attached. Finally the quartz tube, described below, may be attached.

Vapour transport wastes metal that does not reach the site of intercalation. In order to minimise surface area in the containing ampoule, and therefore waste metal, the tube through which the vapour passes (transport tube) is of narrower gauge than the tube in which the metal and graphite is stored (bulb). The glass blower prepares tubes with two bulbs of 10mm outer diameter (OD) quartz glass tubing cut to 1cm length at each end of narrow quartz glass tubing with 8mm OD. The narrow tubing is of 140mm length for the production of C_6Yb samples and of 100mm length for the production of C_6Ca samples. The tubes are then attached by melting to the glass end of the tube section with the glass to metal seal and flange.

Preparation of glass parts often introduces soot, resinous materials, and general dust and dirt into the tube so that it is important to clean the tubes thoroughly. Small quantities of standard detergent and distilled water are used with pipe cleaners to dislodge and rinse away any material associated with manufacture of the tubes. The tubes are then rinsed three times with distilled water, this is followed by rinsing with isopropanol. The isopropanol is

kept in the tube during sonication of the tube using a standard ultrasonic bath. This ensures the complete mixing of the remnant water and the isopropanol, which can mix with the water. The process is then repeated replacing acetone for isopropanol. Subsequently the tube ends are covered to prevent dust settling in transfer and placed in a vacuum oven at 60°C for 12 hours. The tubes are then considered to be free from all but molecular impurities.

In order to remove molecular impurities the tube is then heated under vacuum. Fitted with Edwards's valves they are connected to a turbopump and the ampoule end is placed in a furnace. Outgassing is then carried out at a pressure of 2×10^{-6}mbar whilst heating at 700°C for a period of 24 hours.

Graphite is subject to similar outgassing. The graphite (HOPG or Grafoil) is placed inside the tubes, in the bulb at the very end. The outgassing of the graphite itself is then undertaken at the same pressure, but with a reduced temperature of 600°C, for 60 hours. If graphite powder is to be used then a glass tube of narrower OD than the 6mm inner diameter (ID) of the 8mm OD tubing must be inserted to the bottom of the tube. The graphite powder can then be poured down this tube. This prevents a graphite powder coating, with high thermal conductivity, from transferring heat away from the sealing point and preventing the quartz from softening.

Small pieces of very clean graphite are very mobile in the ampoule and the specific placement of the metal in succeeding steps in the process requires a barrier to prevent the metal and the graphite from exchanging bulbs. The Edwards valves are sealed after outgassing the graphite and the tubes are taken to the glass blower whilst under vacuum. The glassblower presses a set of three or four small dimples into the transport tube around its middle. This narrowing of the tube forms the required barrier.

Outgassing of the ampoule and graphite must be carried out after the introduction of the metal into the tube. In order to introduce the metal into the ampoule the tubes are placed in an MBraun Argon glove box. Appropriate quantities of metal are introduced to the tube but kept near to the glass to

metal transition. This allows for the outgassing of the graphite to remove any argon and oxygen introduced whilst in the glove box, without the metal being heated. This outgassing is once again carried out at 2×10^{-6}mbar and 600°C, but for 24 hours. In order to prevent the contamination of the tube by air the pump must be allowed to achieve at least 10^{-3}mbar before the (Edwards) valve is opened. The ampoule is now clean, with graphite in place and under a vacuum.

In order to seal the ampoule and remove it from the tubing a temperature of approximately 1600°C will be used, this would vaporise the metal if the metal was within about 10mm of the flame. After outgassing the Edwards valve is shut and the tube removed from the furnace. The tube cools during the journey to the glass workshop. The metal is very carefully allowed to slide down to the dimpled midpoint of the narrow tubing. This prevents the heat of sealing from vapourising the metal. The tube may now be sealed as it is, under vacuum, beyond the second bulb on a narrow section of tubing. Once the tube is sealed and has been allowed to cool the metal may be returned to the empty bulb. Holding the tube horizontal and tapping carefully is usually sufficient.

3.3.5 Ampoule Heating

The ampoule is placed in a Vecstar three zone furnace with the graphite end 100mm from the opening. The entire furnace is then brought to 395°C at a rate of about 50°C per hour. The temperature of 395°C is that reported to give an intercalant concentration that increases with the length of the reaction in the case of a powder mix compacted pellet [El-Makrini 1980]. The system is allowed time enough to reach equilibrium. The temperature at the end of the tube containing the metal is then brought to about 500°C, this is the lowest temperature that produces a metal vapour that can be observed by eye to coat the inside of the ampoule. This temperature may require adjustment to obtain a metal vapour. Various environmental factors, such as ambient room temperature, may affect the temperature in the furnace, or an oxide coating may need to be broken to release the metal vapour.

The protocol for preparing C_6Ca is identical to that for C_6Yb, except for the length of the tubing, and the temperatures. The length of the tubing for the C_6Ca is shorter, as discussed in *Section 3.3.4*, to prevent metal condensation occurring part way down the tube. The entire furnace is brought to 450°C at a rate of about 50°C per hour, and after equilibration the temperature of the middle section of the furnace is brought up to around 600°C.

The tube is then left for a period of two weeks. This is the time period over which it was reported that a maximum yield of intercalate for the C_6Yb was obtained, after this time it was reported that the graphitide begins to disappear [El-Makrini 1980]. The literature often records the time period for intercalation but there still occur differences in practice [Chaiken 1998].

3.3.6 Ampoule recovery

After two weeks the ampoules must be removed, one or two days longer will not make a noticeable difference. The removal should be done rapidly. This allows the exterior to cool more rapidly than the interior so that metal remaining in the tube condenses onto the inner side of the tube and not onto the sample. Early in the study a great deal of metal was condensing onto the sample as the removal was done slowly to prevent cracking of the tube.

Typically the two-zone technique would have the graphite region of the ampoule at temperatures higher than the metal region. In the case of the materials synthesised here this would not provide a vapour and leave the graphite at the temperature required. One advantage of the graphite region being hotter than the metal region is that no metal condenses, due to the temperature gradient, on the surface of the sample. So by removing the ampoules swiftly most of the vapour in the ampoule condenses onto the inner surface of the ampoule. In the early stages of development of this sample preparation technique the presence of a layer of magnetic Yb_2O_3 was discovered, this was of great significance to the hypothesis, and it was found that by removing the ampoules swiftly this layer could be greatly reduced.

How the intercalation ampoule was transferred into and out of the furnace receives little attention in the literature [Chaiken 1998]. Though it can be of great importance if for instance one quenches in a high temperature phase where the system would otherwise have taken on a low temperature phase if cooled slowly. In the work presented by Chaiken in her thesis there are inconsistencies in the transfer, the furnace was always cooled down to about 70°C before the ampoules were removed, but sometimes the furnaces were cooled down overnight. Chaiken records that at the University of Kentucky, it was customary to remove ampoules while they were still hot. Sometimes the ampoules were even quenched in liquid nitrogen when they were removed from the oven. It is important to consider which is the most appropriate to yield a desired final product.

3.3.7 Premeasurement Sample Preparation

Samples were prepared before measurement by scraping off the surface coating of oxide. During the XRD and SEM studies of these samples it became obvious that there was a phase of Yb_2O_3 present in the case of the ytterbium-intercalated sample, as mentioned in section 3.3.6, and this was later confirmed by SQUID. This was found to reduce, as discussed in the next section, on scraping of the surface. This scraping was achieved by delicate use of a scalpel blade.

The sample is placed on Scotch Tape and the scalpel blade is drawn transversely across the surface. A light sprinkling of black powder may be observed on the tape. If the sample face is scraped carefully enough then the entire surface of Yb_2O_3 can be removed from the sample as the Yb_2O_3 is rather brittle whereas the intercalate is not. The surface colour of pale gold is thus revealed from underneath the purple of the coating. The edges may be cleaned in a similar manner though care must be taken not to damage the edges that have been so carefully prepared. Using the Scotch Tape the sample can be stood on its edge and held carefully with non-magnetic tweezers whilst the edge is scraped. It can then be turned or rolled across the

tape, between scrapings, until no further black powder appears on the tape. This is a reasonable indication that the majority of Yb_2O_3 has been removed.

3.4 X-ray Diffractometry

3.4.1 Experimental Details

X-ray diffractometry measurements were performed on an as supplied Philips X'Pert X-ray Powder Diffractometer with a custom-made sample environment case.

As the X'Pert is a powder diffractometer it requires some custom additions to the sample goniometer. The laboratory diffractometer is not set up to handle air sensitive materials so that further custom additions are required. The sample environment, designed and built for use in gathering data for this thesis. The casing may be moved in the z-direction to account for varying sample height. It consists of a back plate and sample platform with a cover having a Mylar window. This cover is steel and may be made air tight by means of an indium seal, it may then be pumped out through a valve attachment.

XRD is used in this thesis as the principle means by which to identify the phases present in samples synthesised by the methods set out herein. In the geometry employed only the (00l) reflections are available.

It is typical practice to identify graphite intercalation compounds by their c-axis repeat distance I_c [Dresselhaus 1981]. The Bragg equation is thus sufficient, in most cases, for the confirmation of the presence of a graphite intercalate with a particular stage. The Bragg equation, specific to graphite intercalates, may be derived by considering sets of planes with a common spacing I_c [Kittel 1996]. In specular reflection, when the angle of incidence equals the angle of reflection, each plane will reflect some of the incident light and some will pass to the next plane. If the path difference between any two rays is a half integer number of wavelengths then they will interfere constructively. The path

difference depends on the angle and elementary trigonometry will show that it is $l_c \sin\theta$. Thus the Bragg law specific to graphite intercalates is

$$2l_c \sin\theta = l\lambda$$

and a series of (00l) peaks in an X-Ray diffractogram (XRD) allow l_c to be well determined.

The stage index n can be determined from the relation

$$l_c = (n-1)c_0 + d_s$$

Where c_0 = 3.35Å and d_s is the depth of a graphene intercalant graphene sandwich [Dresselhaus 1981]. Stage fidelity, the presence of a single stage, is established by the absence of satellite diffraction peaks due to small quantities of admixed stages, and by the absence of broadening of diffraction lines at large diffraction angles due to an average over a distribution of stages.

A single stage sample will show full widths at half maximum (FWHM) roughly equivalent to those of pristine graphite, since the crystallites will share the same size and strain properties. A mixed stage sample with macroscopic regions that have stage n and other regions n-1 or n+1 will show reflections broadened relative to those of a single stage sample, with some that can be identified as one constituent, and some that appear shifted due to unresolved $2\theta_l$ components. A randomly staged material with a random arrangement with various stages will show a well-defined diffraction pattern if one phase is dominant but with extensive line broadening. No systematic study of this phenomenon has been carried out for anything other than $FeCl_3$ [Dresselhaus 1981]. A further infidelity that occurs is interstratification, where intercalated regions more or less extensive in the c-axis direction are interspersed with similar graphite regions [Lindsell 1998].

3.4.2 Samples Synthesised with HOPG and Yb

Figure 3.5 shows the c-axis oriented XRD data from a sample prepared from HOPG and ytterbium under the conditions given in the preceding sections. The data may be indexed if considered as three phases with preferred orientation. The indexing is given in *Tables 3.3*, *3.4*, and *3.5*. An explanation of the presence of each phase accompanies the indexing. Each peak is fitted individually with a Pseudo-Voigt function to determine the peak position, intensity, and full width half maximum. Present are HOPG (00l) reflections, C_6Yb (00l) reflections, and a single Yb_2O_3 <111> reflection.

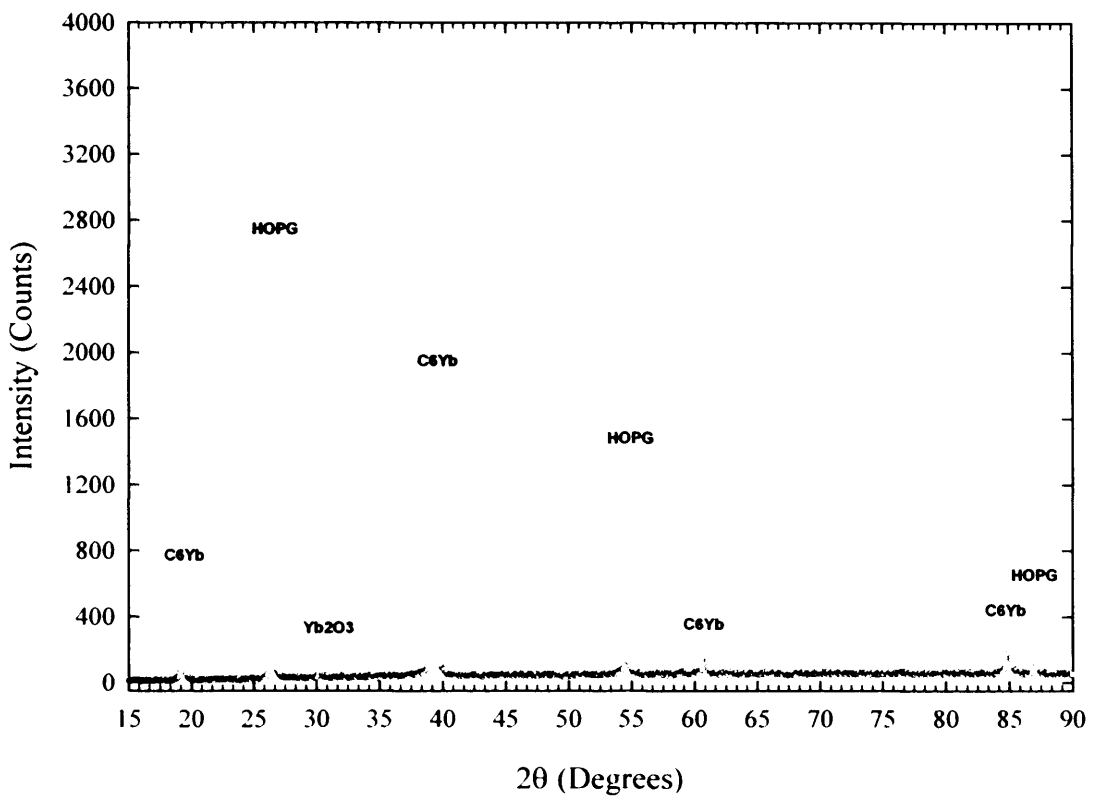

Figure 3.5 The full X-ray diffraction pattern from a sample prepared with ytterbium according to the process detailed in Sections 3.3. The strongest peak is off-scale. A Philips X-Pert X-ray Diffractometer with a CuKα source gave this diffraction pattern typical of the best C_6Yb samples synthesized in this study.

HOPG shares the 3.354Å interlayer spacing of Bernal graphite. The average spacing exhibited in the data indexed in *Table 3.3* is 3.357Å. This represents less than 0.1% error in the d-spacing due to the experimental setup.

Data				Indexing HOPG	
2θ (Degrees)	Intensity (Counts)	100 x I/I_{max}	d (Å)	l_c	D x l_c (Å)
26.517	13069	100	3.357	2	6.715
54.617	1420	11	1.678	4	6.713
87.012	269	2	1.118	6	6.711

Table 3.3 Part of the data from *Figure 3.5* indexed as HOPG. There is a small variation of peak positions away from the average unit cell depth of 6.71 ±0.01Å, this may indicate interstratification.

The third peak evident in *Figure 3.5* may be indexed as the <111> reflection of Yb_2O_3. The appearance of only this reflection from this impurity phase may be understood quite clearly when one observes the hexagonal symmetry of the crystal along this direction. This phase is growing on a hexagonal substrate so that it would be expected to have a strong preferred orientation in the hexagonal direction.

Data				Indexing Yb_2O_3	
2θ (Degrees)	Intensity (Counts)	100 x I/I_{max}	d (Å)	$l_{a,b,c}$	D x l_a (Å)
30.311	60	100	2.945	111	

Table 3.4 Part of the data from *Figure 3.5* indexed as Yb_2O_3. Only the (111) peaks appear due to the preferred orientation in the growth of the oxide due to the hexagonal substrate, the <111> is the only peak to be resolved.

Table 3.5 shows those parts of the data indexed as C_6Yb and may be compared to the data recorded by the Nancy group (*Table 3.6*). Stage 1 C_6Yb was identified in 1980 as having a space group $P6_3mmc$ [El-Makrini 1980]. The Nancy group interpreted the X-ray diffractometry data to show a stacking of AαAβ. The sandwich depth they gave on the basis of a stage 1 C_6Yb with this stacking was 4.57Å. *Figure 2.4* shows the unit cell of this structure.

Data				Indexing C_6Yb	
2θ (Degrees)	Intensity (Counts)	100 x I/I_{max}	d (Å)	l_a	D x l_a (Å)
19.413	629	36	4.567	2	9.134
39.466	1739	100	2.280	4	9.122
60.860	112	6.44	1.520	6	9.122
84.965	136	7.8	1.140	8	9.121

Table 3.5 Part of the data from *Figure 3.5* indexed as C_6Yb. There is a small variation of peak positions away from the average unit cell depth of 9.13 ±0.01Å, this may indicate interstratification.

Data				Indexing C_6Yb	
θ (Degrees)	Intensity (Counts)	100 x I/I_{max}	d (Å)	l_c	D x l_c (Å)
4.48		42.4	4.540	2	9.08
8.94		100	2.282	4	9.128
13.48		22.2	1.521	6	9.126
18.10		33	1.141	8	9.128
22.90		7	0.911	10	9.110
27.80		7.5	0.760	12	9.120

Table 3.6 Data given by El Makrini et al. using MoK_α. The average unit cell depth is 9.12 ±0.01Å.

The average value of l_c observed in these measurements is in accord with that observed by the Nancy group. The relative intensities are also in agreement, although the 006 and 008 reflections are lower in intensity in this study.

3.4.3 Samples Synthesised with HOPG and Ca

Figure 3.6 shows the c-axis oriented X-ray diffractometry data from a sample prepared from HOPG and calcium under the conditions given in *Section 3.3*. The data may be indexed if considered as four phases with preferred orientation. Present are HOPG (001), C_6Ca (001), CaO <111>, Ca <200>. The indexing is given in Table 3.4.2.1,2,3, and 4.

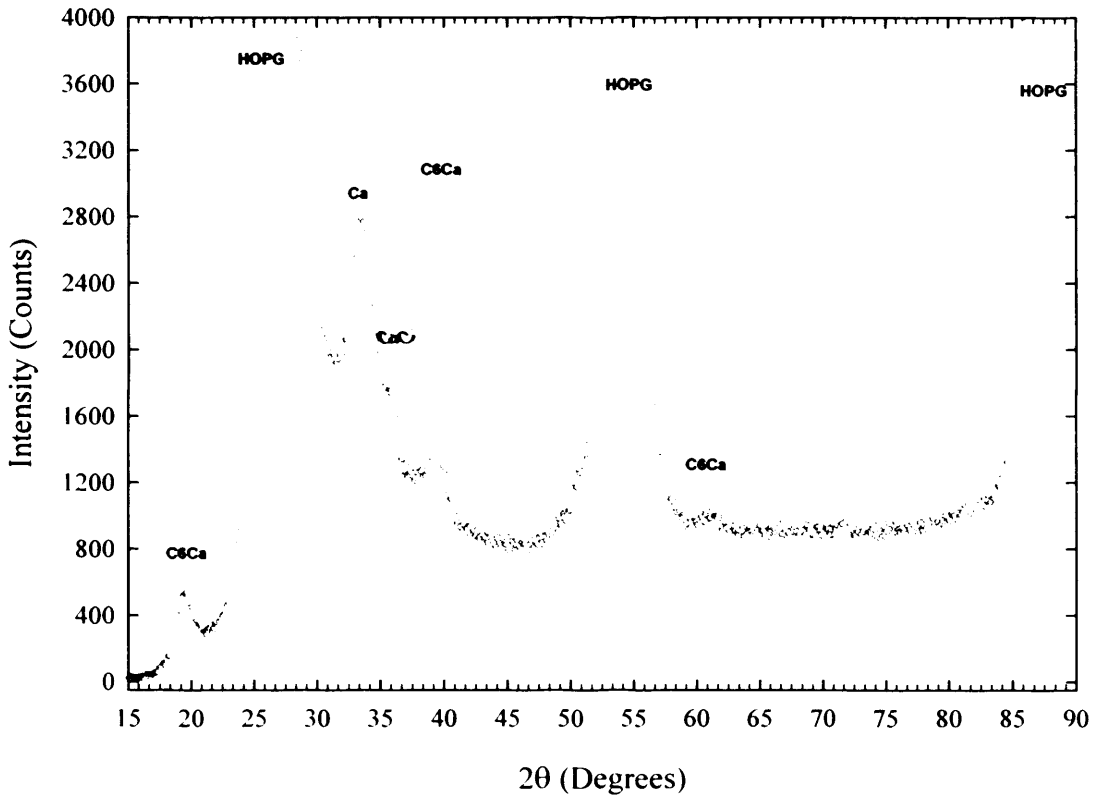

Figure 3.6 The full X-ray diffraction data set for the calcium exposed HOPG. The data set was taken using a laboratory diffractometer according to *Section 3.4.1*. It shows 8 diffraction maxima analysed in this section.

The average HOPG spacing exhibited in the data indexed in *Table 3.7* is 3.38 ±0.01Å. This represents only a 0.8% error in the d-spacing due to the experimental setup. Since the sample height was adjusted to maximise the signal on the C_6Ca 004 peak it might be expected that the error might be less.

Data				Indexing HOPG	
2θ (Degrees)	Intensity (Counts)	100 x I/I_{max}	d (Å)	I_a	D x I_a (Å)
26.102	24346330	100	3.410	2	6.820
54.266	2018673	8.291	1.688	4	6.753
86.733	233289	0.958	1.121	6	6.728

Table 3.7 Part of the data from *Figure 3.6* indexed as HOPG. There is a small variation of peak positions away from the average unit cell depth of 6.77 ±0.01Å, this may indicate interstratification.

The other peak is the <200> reflection from Ca. The origin of this preferred orientation is in the triangular symmetry in the (200) direction of Ca.

Data				Indexing Ca	
2θ (Degrees)	Intensity (Counts)	100 x I/I_{max}	d (Å)	$I_{a,b,c}$	D x I_a (Å)
33.655	927	100	2.660	200	-

Table 3.8 Part of the data from *Figure 3.6* indexed as Ca.

CaO, or lime, is the most stable oxide of calcium. CaO, like Yb_2O_3, is a cubic system. Consequently it is the (111) reflection that is observed for the oxide impurity phase in the data in *Figure 3.6*. The (111) in CaO is 2.778 Å. The CaO is rather disordered and the peak is therefore broad.

Data				Indexing CaO	
2θ (Degrees)	Intensity (Counts)	100 x I/I_{max}	d (Å)	$I_{a,b,c}$	D x I_a (Å)
35.825	527	100	2.504	111	-

Table 3.9 Part of the data from *Figure 3.6* indexed as CaO. The d-spacing is to be compared to the recorded value of 2.78Å.

Table 3.10 shows the C_6Ca in the sample may be indexed on the same basis as the indexing made by Guérard et al. in 1979. The Nancy University group were able to index the (002) peaks to give an average c-axis unit cell depth of 9.10Å ± 0.02Å. *Table 3.10* shows that the C_6Ca, synthesised by the method

detailed in *Sections 3.3*, shares this average. The Nancy group were not able to confirm the space group of the C_6Ca, however they were able to identify it as a hexagonal system [Guérard 1980].

Data				Indexing C_6Ca	
2θ (Degrees)	Intensity (Counts)	100 x I/I_{max}	d (Å)	l_a	D x l_a (Å)
19.525	529	18.14	4.541	2	9.082
39.440	2916	100	2.282	4	9.128
60.678	924	31.69	1.524	6	9.146

Table 3.10 Part of the data from *Figure 3.6* indexed as C_6Ca. There is a small variation of peak positions away from the average unit cell depth of 9.12 ±0.01Å, this may indicate interstratification as discussed in *Section 3.4.1*.

3.5 Studies of Sample Morphology

Scanning electron microscopy (SEM) has been used in conjunction with energy dispersive analysis of X-rays (EDAX) to observe the sample morphology in much more detail than is possible with XRD. For a material density of 2g/cc (HOPG) the penetration of the SEM electrons into the material will be 30nm at 1kV, and 1.5μm at 10kV, for a material density 3.59g/cc (C_6Yb) the electrons will penetrate to 20nm for a 1kV potential and 0.9μm for a 10kV potential.

3.5.1 Yb and Yb_2O_3 Overlay the Sample

Slow cooling recovery of the ampoules gives a surface covering of ytterbium and ytterbium oxide. Images in *Figure 3.7* show dendritic structures that EDAX determines are ytterbium metal, with a darker surface in between these, which EDAX shows to be ytterbium oxide. The faster removal of ampoules from the furnace reduces the ytterbium and the Yb_2O_3 surface layer according to the XRD evidence. The remaining overlayer is brittle and may be removed by scraping.

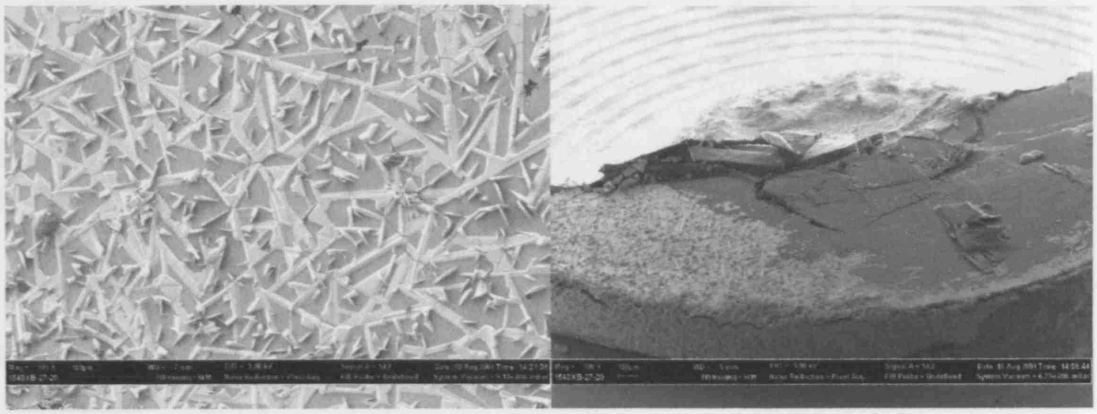

a) b)

Figure 3.7 Image (a) is 1mm across and shows the oxide and ytterbium coating, image (b) shows a 5mm disc broken in half with the oxide and ytterbium layer partially scraped off.

3.5.2 Yb intercalant ions penetrate from the edge

Figure 3.8 shows a sequence of images of a cleaved 1mm disc. EDAX confirms the dark central region to be pure carbon, and the bright edge ring to be close to the appropriate stoichiometric ratio for C_6Yb. The cleaving reveals the interior of the sample and demonstrates that the intercalant atoms penetrate about 0.1mm from the edge of the HOPG after two weeks. Penetration of the electron beam through to pure graphite regions beneath intercalate layers prevents the exact stoichiometry from being identified by this method, since carbon atoms are over counted. The edge of the intercalated region is richly structured and reveals a number of qualitative conclusions of importance.

Figure 3.9 shows more clearly the patterns and structures that arise in the intercalation process. Steps in the HOPG can be observed and the growth pattern of the intercalant regions follows the patterns that might be expected from multiple nucleations of new intercalate regions into the same crystallite. The curved edges are clearly diffusion limited boundaries, and where two diffusion limited boundaries meet they flatten out as in the area just above the triangular feature where four different nucleations in fairly close proximity have led to 4 different regions of intercalation with straight boundaries where they touch.

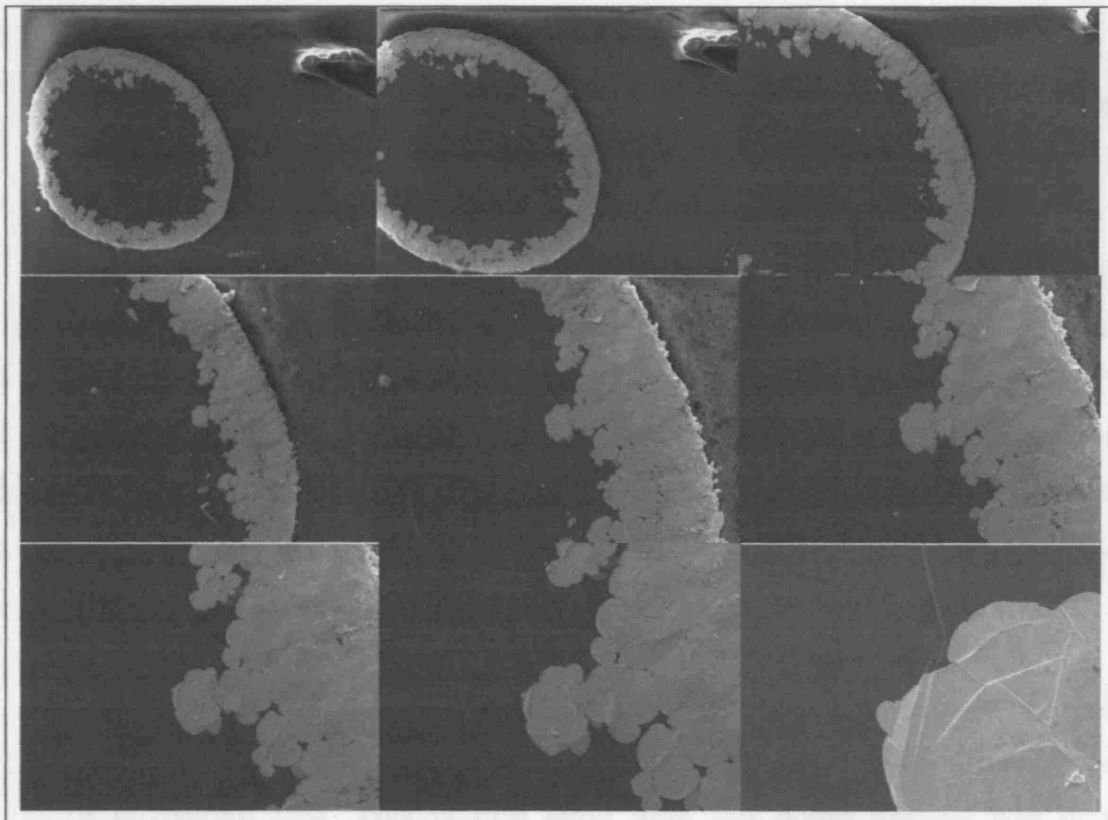

Figure 3.8 The images show a sequence of SEM images that zoom in (top left to bottom right) from the entire sample to a triangular structure about 7.5μm on a side, seen at the right of the bottom right hand image. The sample has been cleaved so that the interior is observed.

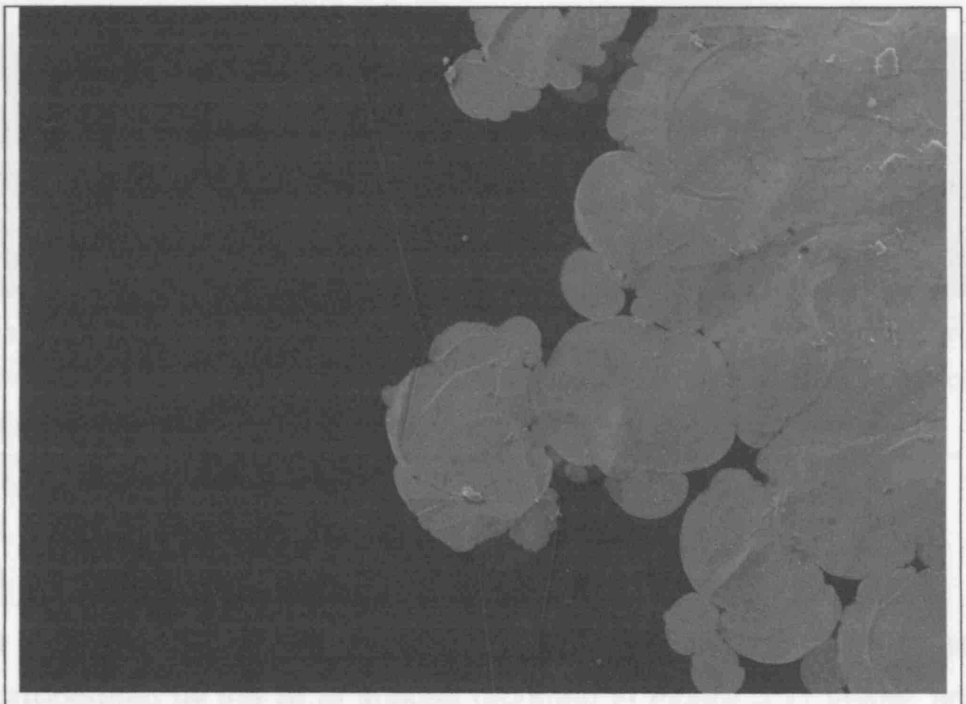

Figure 3.9 The rich texture of the intercalant boundary.

3.5.3 Interstratification and oxidation

Interstratification is clearly observed at the boundary between the intercalated region and the pure graphite. *Figure 3.10* shows the triangular feature seen in *Figure 3.9*. In *Figure 3.10*, from top to bottom, the images are made with a progressive increase in the energy of the electrons, so that they penetrate deeper into the sample. In this case we are observing a C_6Yb region upon HOPG, a region where the ytterbium ions have not penetrated as far into the substrate. This reveals that the C_6Yb region toward the centre is less deep. The implication is that at the boundary between the completely intercalated region and the pure HOPG region there is significant interstratification [Lindsell 1998].

Only the open edges of C_6Yb are air sensitive. Observing the cleaved sample with SEM and EDAX in conjunction it may be noted that the interior region of C_6Yb is oxygen free. This is true even after the entire sample has been exposed to air for some time on more than one occasion. This demonstrates that if there is no direct contact between the Yb ions and oxygen that the sample will not oxidise. The carbon provides sufficient protection to the ytterbium against oxidation.

Figure 3.10 The left image shows the triangular feature from Figure 3.9 in close up. From left to right the penetration depth of the electrons is increased showing the interstratification of the boundary region.

3.5.4 C_6Ca

C_6Ca gives a lower yield than C_6Yb according to the XRD data, this seems to be corroborated by the SEM images recorded in *Figure 3.11* below, and will be further clarified by the form of the magnetisation data in *Chapter 4*. The surface is clearly mottled, there are many gaps between bright regions. The

gaps are more carbon rich according to EDAX than the islands, which are Ca rich, so that we may conclude that the bright islands are intercalated regions.

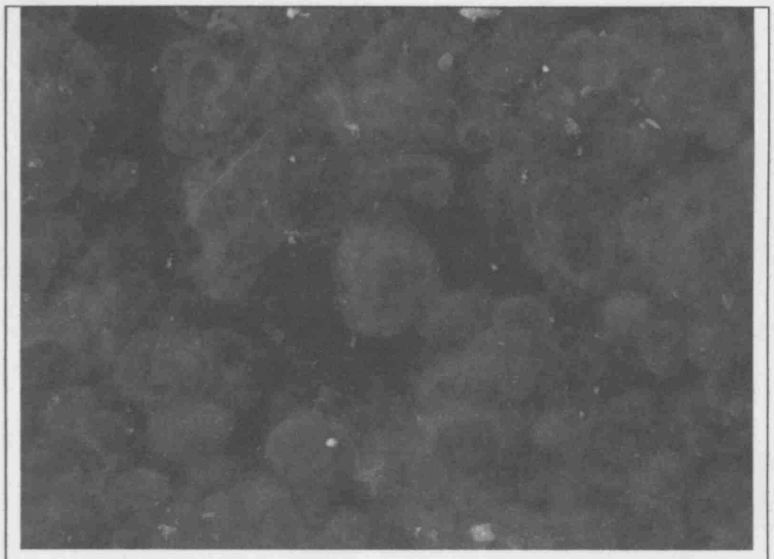

Figure 3.11 An SEM image of the surface of a C_6Ca sample, about 150μm across. The bright regions show up the intercalated material, and the dark regions the HOPG. It is clear that the sample is quite inhomogeneous.

Bright regions become denser closer to the edge of the sample disc, as can be seen from *Figure 3.12*. This may be explained as the surface penetrating islands overlapping with the edge penetrating islands.

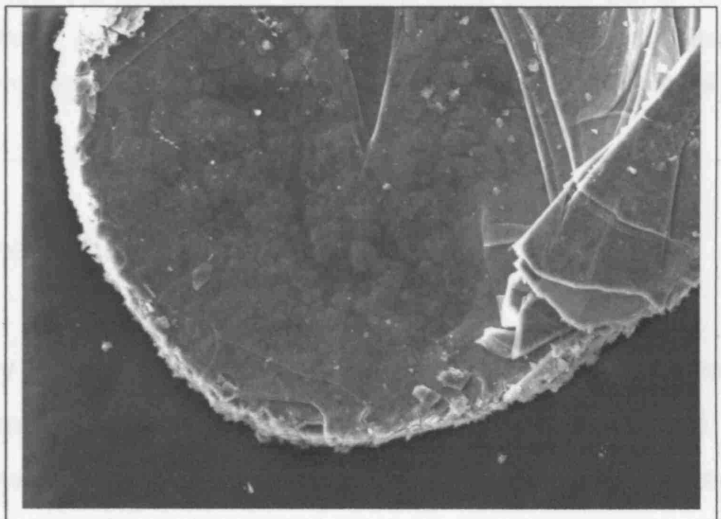

Figure 3.12 An SEM image of a 1mm C_6Ca disc sample. Bright regions show the C_6Ca and the darker regions the HOPG. The sample is more homogeneous closer to the edge.

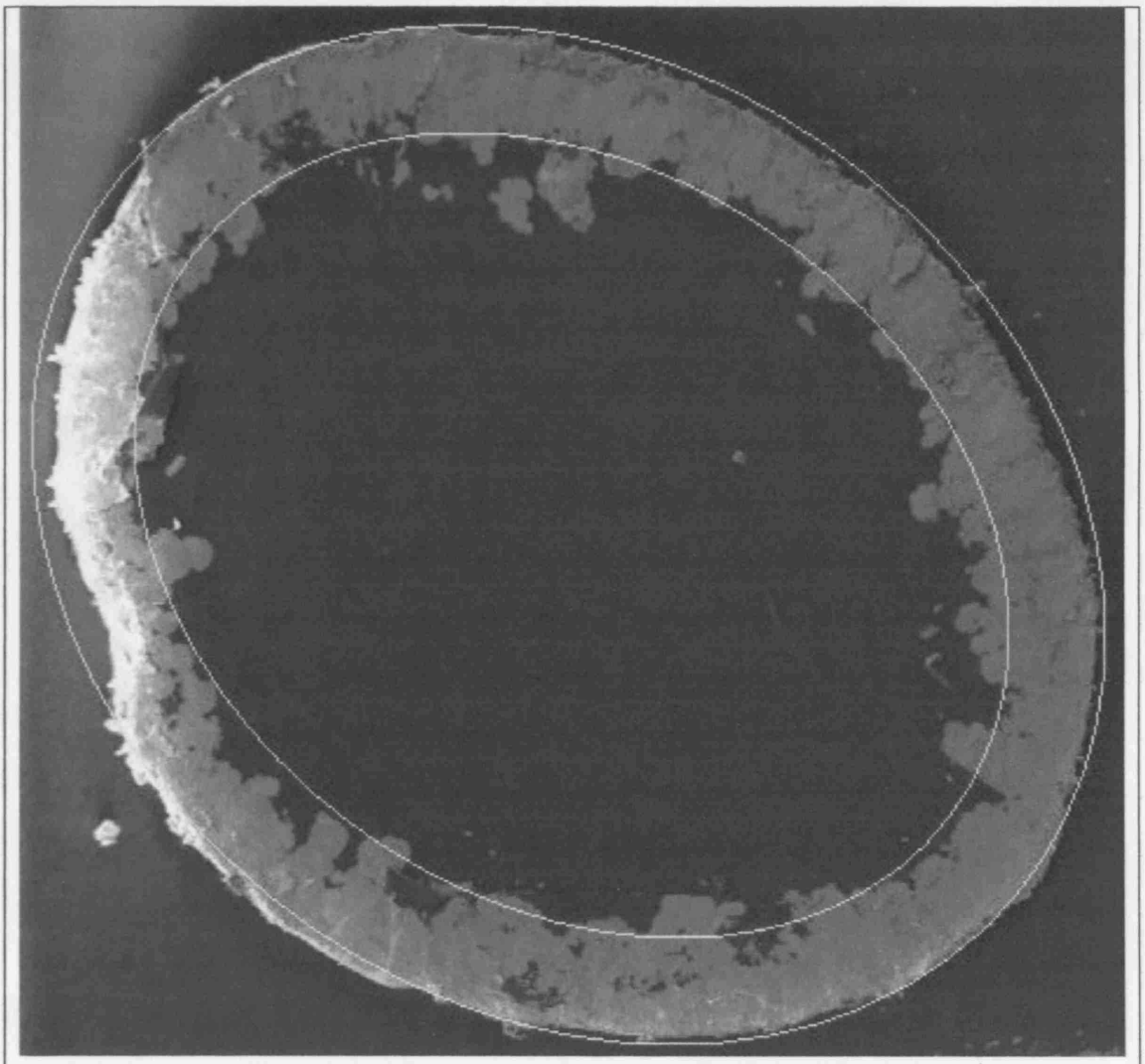

Figure 3.13 The interior region of a cleaved 1mm disc sample showing C_6Yb around the edge where the ytterbium intercalants have penetrated about 0.1mm during the 2-week vapour transport. The large yellow ellipse is 1mm x 0.817mm and the smaller is 0.821mm x 0.635mm. The smaller ellipse is thus 64% of the larger, giving an estimate of 36% C_6Yb in the sample.

3.5.5 Volume Estimate

The geometry of the C_6Yb sample is such that the XRD estimate of the volume of sample that is intercalated must be underestimated. Consider that the SEM shows that the sample is a disc of HOPG surrounded by a ring of intercalate. The HOPG supplied has a density of 2.26g/cc [GE 2006] and consequently a normal attenuation depth of just over 1mm [LBL 2006]. This is in stark contrast to the C_6Yb that at 3.59g/cc has a normal attenuation length

of 27microns. These attenuation lengths are for normal penetration, even so the depth to which the average X-ray of 1.54Å will penetrate in the HOPG is 38 times greater than in the C_6Yb. The top surface of C_6Yb will be uniformly penetrated by the X-rays, underneath the HOPG will be penetrated to a depth of 460microns at 26.6°, the angle at which the HOPG <002> is observed, whereas at 19.5°, the angle at which the C_6Yb <002> is observed, the C_6Yb will only be penetrated to 9.1microns. Once the top-most surface of C_6Yb is penetrated the remainder of the sample will appear to contain a disproportionate amount of HOPG.

A volume estimate based on the SEM images seems therefore more reliable. Taking the image of the cleaved C_6Yb sample and overlaying it with two ellipses, *Figure 3.13*, an estimate of the volume can be made. The smaller ellipse is 64% of the larger. An estimate of 36% C_6Yb is therefore given.

3.6 Summary

The method detailed in this chapter successfully produces C_6Yb and C_6Ca. The C_6Yb 1mm disc samples are ~36% intercalated HOPG, they are closed cylindrical regions of C_6Yb containing a core of HOPG. The boundaries between the HOPG and the intercalate are interstratified. There may be Yb_2O_3 and Yb present on the outer surface of the C_6Yb samples, and CaO and Ca on the outer surface of the C_6Ca samples. These impurities may be removed by scraping the sample, and reduced during the synthesis process by rapid removal of the ampoules from the furnace. There are many HOPG regions separating C_6M regions in both materials, however the homogeneity of C_6Yb is much better than that of C_6Ca.

Chapter 4

Magnetisation Data & Analysis

This chapter presents data gathered with a Quantum Design MPMS7 SQUID magnetometer from measurements on samples described in detail in *Chapter 3*. Data from supplementary measurements on ZYA HOPG and Yb_2O_3 is also included for the purpose of analysing the data and determining that behaviour attributable to the C_6Yb and C_6Ca.

4.1 Experimental Details

Magnetometry measurements were performed using an as supplied Quantum Design MPMS7 Magnetometer and sample rod. Details of the instrument and its parameter control can be found in the relevant manuals, available from Quantum Design. For historical reasons the instrument measures the moment (m) of the sample in emu, this is a non-SI unit, and the reader should make careful use of appropriate units for different aspects of magnetisation data analysis.

As a sample mount a drinking straw was prepared with a pair of narrow slits cut halfway along its length. These slits are oriented either in line with the axis of the straw or perpendicular to it, to support the sample either with the field in the ab-plane (H//ab) or with the field along the c-axis (H//c). Whilst in a Braun Argon glove box the sample is sandwiched in a fold of Kapton tape. This protected the sample from the atmosphere during the mounting stage, and allowed it to be fixed securely in the slits. A straw was placed in the glove box and the Kapton envelope containing the sample was fed through the pairs of slits in the straw. The tape was then secured to the outside of the straw. The straw, containing the sample in its Kapton envelope, was later removed from the glove box and hastily transferred to the end of the sample rod, where it was fitted over a coil of Kapton tape snugly enough to hold it securely. Additional security was provided by a single coil of Kapton around the top of the straw. The sample was then placed in the airlock on the MPMS7 and the airlock purged. The amount of tape around the sample was always minimised and a consistent use of the same amount of tape was made between different measurements. This ensured that the background signal from the Kapton and the gap in the sides of the straw was accounted for in the sample data by the subtraction of the data from measurements of HOPG.

The size of the samples available for measurement in this case is small compared to the calibration sample, and the scan length used (4cm) was

identical to that used for the calibration scan. Thus ensuring that the voltage response fit produces a good measurement of the magnetisation.

During measurements it was important to keep track of the immediate history of the sample. Remnant fields unaccounted for in a magnetic or superconducting sample can interfere with measurement of true magnetisation values. In order to ensure the effects of such fields are minimised the sample is always warmed well above the superconducting transition, and the magnet quenched between measurements.

4.2 Magnetisation and susceptibility of ZYA HOPG

Chapter 3 demonstrated that a percentage of the samples synthesised remained HOPG. In order to account for the HOPG in the sample a background subtraction will be carried out. This will be made on the basis of the magnetisation (M = m/V), in emu/cc, of HOPG as measured using the MPMS7. The correct HOPG background magnetisation, for any given sample, may then be calculated from knowledge of the sample volume and the superconducting volume estimate made in *Chapter 3*.

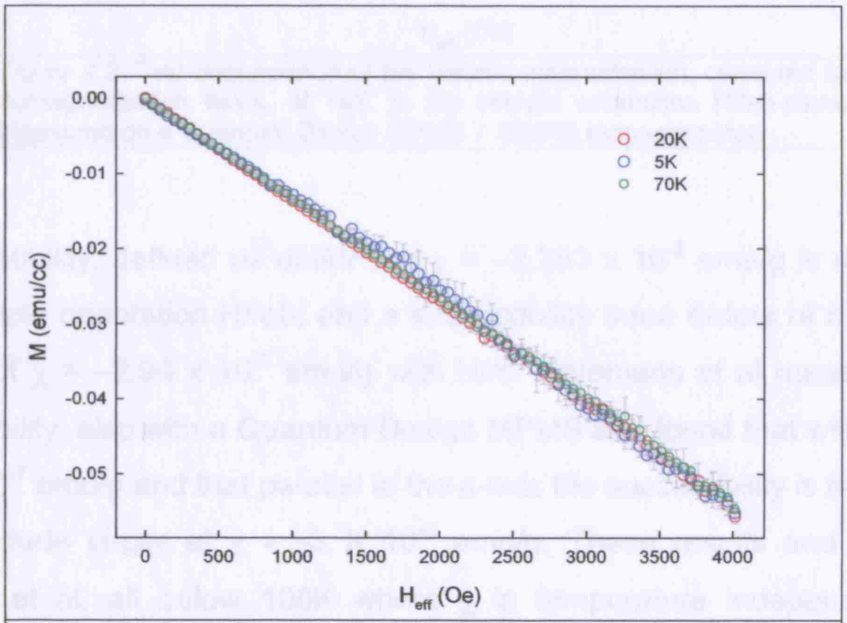

Figure 4.1 Field dependence of the H//c volume magnetization of ZYA HOPG, corrected for demagnetisation fields, at 5, 20, and 70K, in the sample orientation.

Observations at constant temperature made on ZYA HOPG, prepared according to *Chapter 3*, show that it has a diamagnetic response to a magnetic field that is temperature independent to about 100K, in agreement with the literature [Heremans 1994]. *Figure 4.1* gives the field dependence up to 4000Oe for temperatures of 5, 20, and 70K with the sample orientation H//c. *Figure 4.2* gives the field dependence up to 4000Oe at 10K with the sample orientation H//ab.

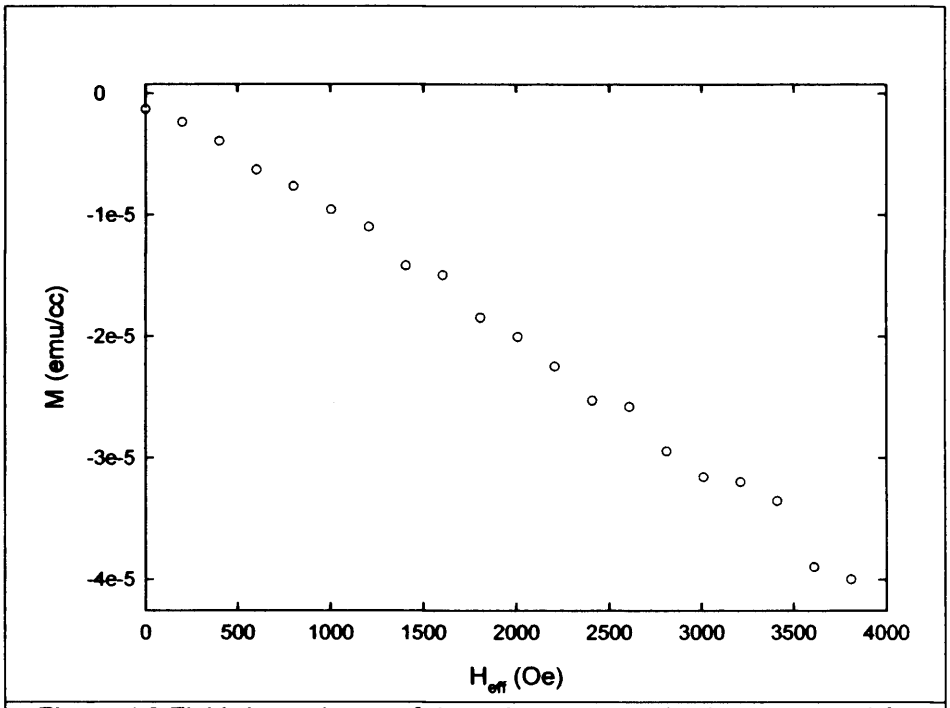

Figure 4.2 Field dependence of the volume magnetisation, corrected for demagnetisation fields, at 10K, in the sample orientation H//ab-plane. Measured on a Quantum Design MPMS 7 SQUID magnetometer.

A susceptibility, defined as dM/dH, of χ = –2.283 x 10^{-8} emu/g is measured with sample orientation H//ab, and a susceptibility three orders of magnitude greater of χ = –2.94 x 10^{-5} emu/g with H//c. Heremans et al measured the susceptibility, also with a Quantum Design MPMS and found that with H//ab χ = -5 X 10^{-7} emu/g and that parallel to the c-axis the susceptibility is two orders of magnitude larger at χ = -3 X 10^{-5} emu/g. These results and those of Bandow et al, all below 100K where χ is temperature independent, are summarised for clarity in *Table 1*. The diamagnetism of the C^{4+} ion has χ = -1.2 X 10^{-8} emu/g [Bandow 2001].

	$\chi_{H//ab}$ emu/g	$\chi_{H//c}$ emu/g
Weller 2005	$-2.28 \pm 0.02 \times 10^{-8}$	$-2.94 \pm 0.01 \times 10^{-5}$
Heremans 1994	-5×10^{-7}	-3×10^{-5}
Wilkinson 1989	-6×10^{-7}	-2.1×10^{-5}
Bandow 2001	-6×10^{-6}	-3×10^{-5}

Table 4.1 A comparison of the results of various studies of the susceptibility of HOPG.

The background for the C_6M H//c-axis data will be taken from the 20K data set in *Figure 4.1*, as this data set has the lowest uncertainty it will provide the best fitting. The dependence takes the form:

$$M = 2.68 \times 10^{-5} - 1.36 \times 10^{-5} \times H_{eff}$$

The background for the C_6M H//ab-plane will be taken from the 10K data set in *Figure 3.2*. The dependence takes the form:

$$M = -1.08 \times 10^{-6} - 8.99 \times 10^{-9} \times H_{eff}$$

These forms will give the volume moment of the HOPG and will be adjusted for the volume of HOPG present in the sample based upon the SEM estimate.

The background subtraction introduces uncertainties. The significance of these uncertainties is once again dependent on the field orientation. In H//ab-plane the magnitude of the moment due to the HOPG substrate is insignificant compared to the overall moment due to the C_6Yb. In the H//c-axis measurements it does create a small but significant shift, that is however within the error due to the demagnetisation correction.

4.3 Demagnetisation Corrections

The demagnetisation correction, discussed in *Chapter 1*, makes the values given for the field at which transitions occur more accurate, but introduces errors that make the value less precise. This is because the demagnetisation correction shifts the field value to more appropriately reflect the true field experienced by the sample. However it relies on a number of elements each with their own associated errors.

The uncertainty on the effective field (H_{eff}) is composed of the uncertainty on the true applied field, the uncertainty on the geometric demagnetisation factor, the uncertainty on the measurement of the magnetisation, and the uncertainty on the volume. In turn the uncertainty on the demagnetisation factor and the uncertainty on the volume are dependent on the uncertainty on the dimensions. The uncertainties due to the volume estimate and the measurements of dimension of the sample produce the largest uncertainty.

The die with which the sample is made is accurate in its dimension and the size of the sample makes it easy to cut accurately to the die. As there is not expected to be any change in the ab-plane dimensions of the sample due to intercalation there is not expected to be any significant uncertainty, and so the uncertainty on the radius of a 5mm disc sample is taken as 1%.

Whilst the radius of the disc may be determined with some accuracy the thickness must be estimated. The cleanliness required of the sample means that its thickness could not be measured with a micrometer prior to preparation for loading into the magnetometer. A thickness of 0.5mm is estimated by eye, with the help of Vernier callipers, an error of 0.05mm, 10% is reasonable.

The demagnetisation correction is only significant in the H//c-axis orientation and only for values of H_{C1}. Applied field bares a relation to the internal field that is discussed in *Chapter 1*. In the H//c orientation the demagnetisation factor is ~0.8, whereas in H//ab it is ~0.08, see *Figure 1.5*. This is due to the

difference in the profile that the sample presents to the field between the two orientations. *Equation 1.23* gives $H_{int} = H_{app} - N(m/V)$ so that as M tends to zero H_{int} tends to H_{app} and consequently at H_{C2} there is no demagnetisation correction. Thus the error introduced by the demagnetisation correction is only significant to the value of H_{C1} in H//c.

4.4 C_6Yb

4.4.1 C_6Yb Tc = 6.5K

Figures 4.3 & 4.4 show a sharp transition to a diamagnetic state at 6.5K, for both field orientations, measured in 50Oe.

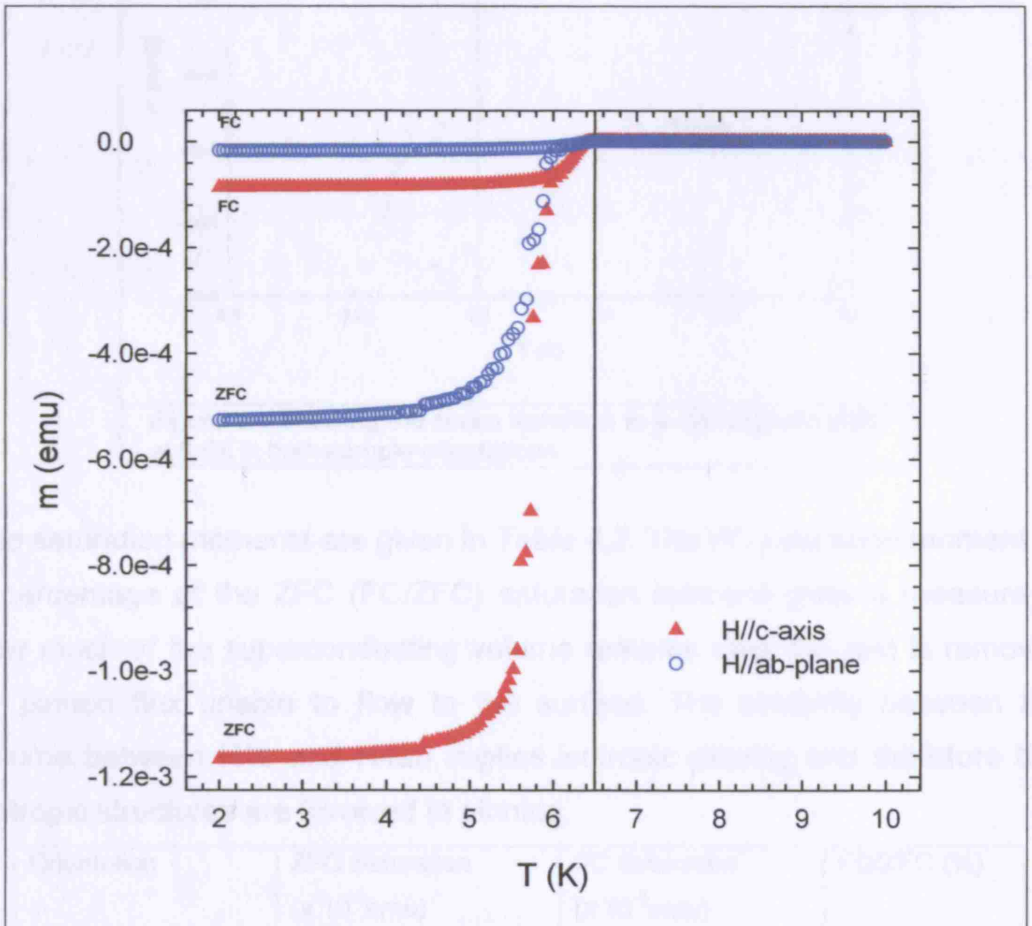

Figure 4.3 Temperature dependence of the magnetization, in 50Oe applied field, of C_6Yb samples showing hysteresis due to flux pinning in both sample orientations. In each orientation the greater magnitude of saturation is for a zero field cooled (ZFC) measurement and the smaller magnitude of saturation is for a field cooled (FC) measurement.

Figure 4.3 gives the full data set showing saturation of the diamagnetic signal. In each orientation the greater magnitude of saturation is for a zero field cooled (ZFC) measurement and the smaller magnitude of saturation is for a field cooled (FC) measurement. The hysteresis may be explained by flux pinning. In the ZFC measurement the full Meissner state is eventually reached through most of the material, and the saturation magnetization is at its maximum. In the FC measurement flux is trapped by defects, grain boundaries, and impurities, and a smaller saturation is achieved.

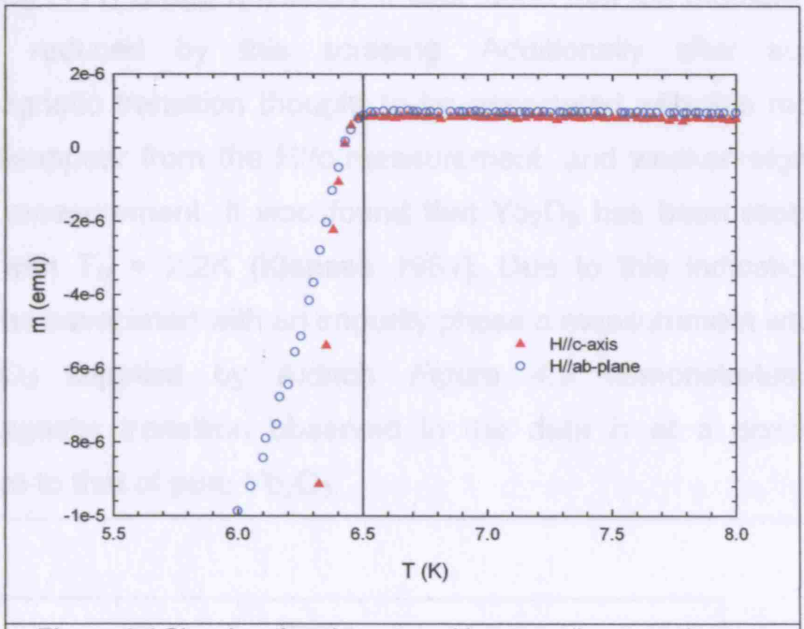

Figure 4.4 Showing the sharp transition to a diamagnetic state at 6.5K in both sample orientations.

The saturation moments are given in *Table 4.2*. The FC saturation moment as a percentage of the ZFC (FC/ZFC) saturation moment gives a measure of how much of the superconducting volume remains after the rest is removed by pinned flux unable to flow to the surface. The similarity between this volume between H//c and H//ab implies isotropic pinning and therefore that isotropic structures are involved in pinning.

Orientation	ZFC Saturation (x 10^{-3}emu)	FC Saturation (x 10^{-5}emu)	FC/ZFC (%)
H//c	1.17 ± 0.001	8.58 ± 0.001	7%
H//ab	0.526 ± 0.0001	1.67 ± 0.001	3%

Table 4.2 Magnitude of the saturation magnetization for ZFC and FC scans in each orientation. The table shows the ratio FC/ZFC as a percentage, as well as (ZFC-FC)/ZFC the difference as a percentage of the ZFC.

4.4.2 Antiferromagnetic Transition is due to Yb_2O_3

Early measurements on the samples synthesized by the method in *Chapter 3* showed a Curie-Weiss behaviour which suggested a small moment on the ytterbium ion. This small moment initially implied that the hypothesis was realised, that magnetically mediated superconductivity was potentially present in C_6Yb. However, as demonstrated in *Section 3.4.1*, there was an Yb_2O_3 impurity present and scraping the surface of the sample reduces the intensity of the Yb_2O_3 (111) Bragg reflection. It was found that the moment measured was also reduced by this scraping. Additionally after scraping an antiferromagnetic transition thought to be associated with this moment was found to disappear from the H//c measurement, and weaken significantly in the H//ab measurement. It was found that Yb_2O_3 has been reported to be magnetic with T_N = 2.2K [Klaasse 1981]. Due to this indication that the moment was associated with an impurity phase a measurement was made on pure Yb_2O_3 supplied by Aldrich. *Figure 4.6* demonstrates that the antiferromagnetic transition observed in the data is at a nearly identical temperature to that of pure Yb_2O_3.

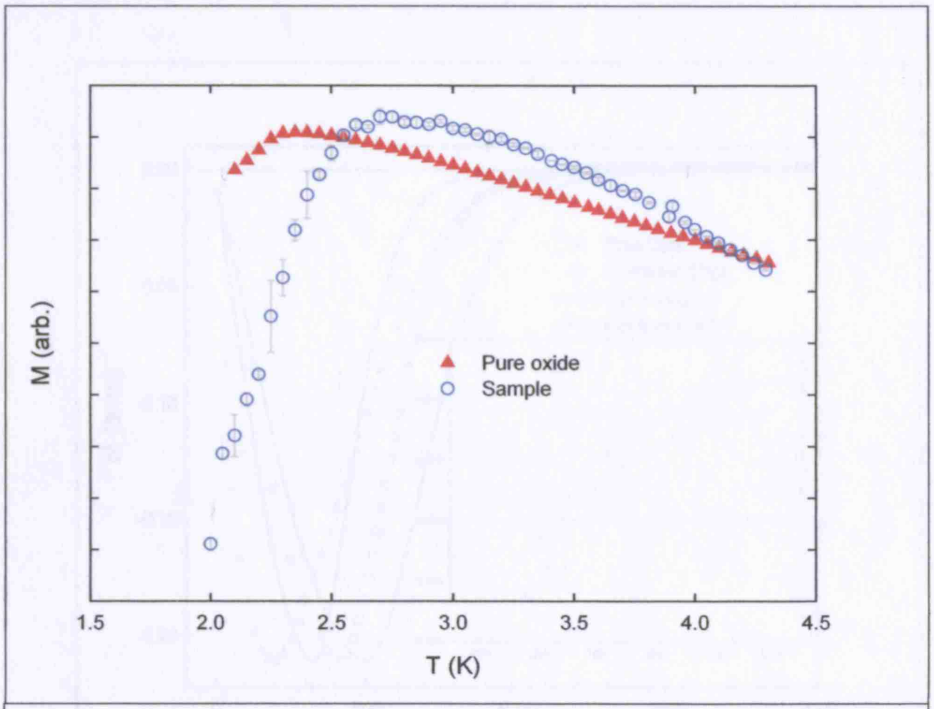

Figure 4.6 Temperature dependence of the magnetisation for a C6Yb sample at 2600Oe compared to pure Yb2O3 at the same field. The magnitudes have been scaled for easy comparison.

4.4.3 C_6Yb is Type II with Low Critical Fields and Low Anisotropy

Corrections to M(H) data are necessary for a realistic determination of the Critical Fields. *Figure 4.7* shows raw data (red circles) from measurements taken at 2K on a 5mm disc sample with an H//c-axis orientation. The effects of the corrections can be clearly seen. The form of the data is very similar, though the gradient up to the minimum is flatter in the corrected data. A diamagnetic component is observed to rise to a maximum and then decrease in strength until the magnetisation becomes small and positive.

Black lines showing an envelope about the corrected data in *Figure 4.7* demonstrate the significance in the H//c-axis of the uncertainty introduced by the corrections to the data. The inset shows the region where M is very small, though it appears that the precision is very bad it should be noted that the value of H_{c2} may be taken from the uncorrected data since the demagnetisation correction is negligible, as discussed above. At temperatures close to the transition temperature however the value of the HOPG background becomes more significant and the two begin to diverge, but only by 20Oe in 290Oe, about 7% and less than the error on the raw data.

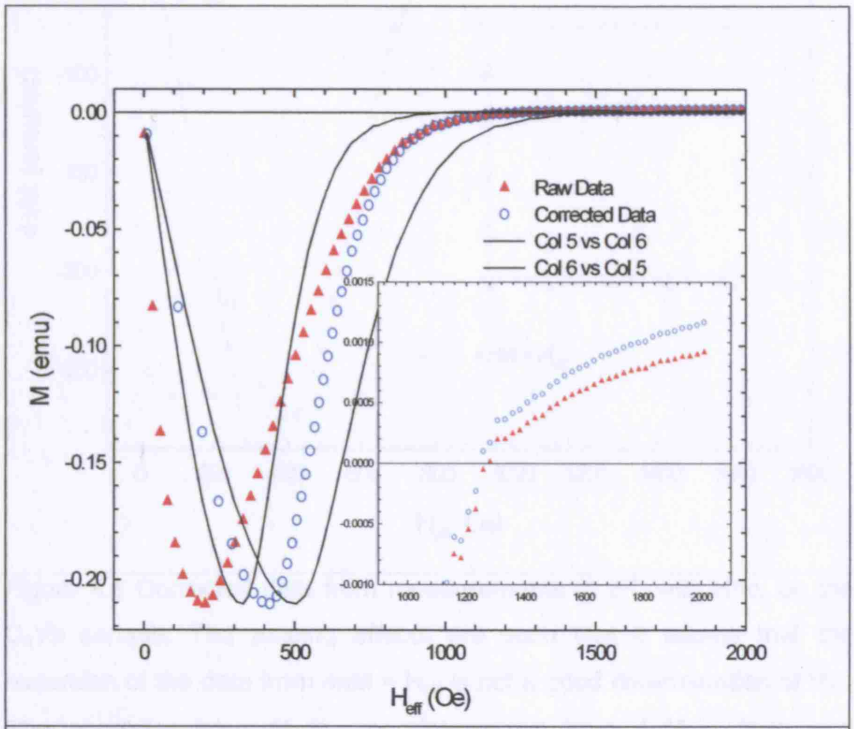

Figure 4.7 Raw data (red circles) and corrected data (blue circles) from measurements at 2K on a 5mm disc sample with H//c-axis.

The behaviour demonstrated by *Figure 4.7* is consistent with a Type II superconductor, as discussed in *Chapter 1*.

Figure 4.8 shows the corrected data from measurements at 2K, with H//c-axis, and a straight line $-4\pi M = H_{eff}$. The deviation from $-4\pi M = H_{eff}$ is not a good determination of H_{c1}, since it occurs before a significant number of data points are available. The physics of the first penetration of flux into the sample makes the determination of H_{c1} difficult, however the true shape of the curve is dependent on the configuration of the pinning sites, which will be independent of temperature. This means that in the absence of an accurate absolute value of H_{c1} at least the relative temperature dependence can be determined by using the position of the minimum of the curve as the value of H_{c1}. The absolute value of H_{c2}, as determined from $4\pi M = 0$ is more easily determined, within the experimental error.

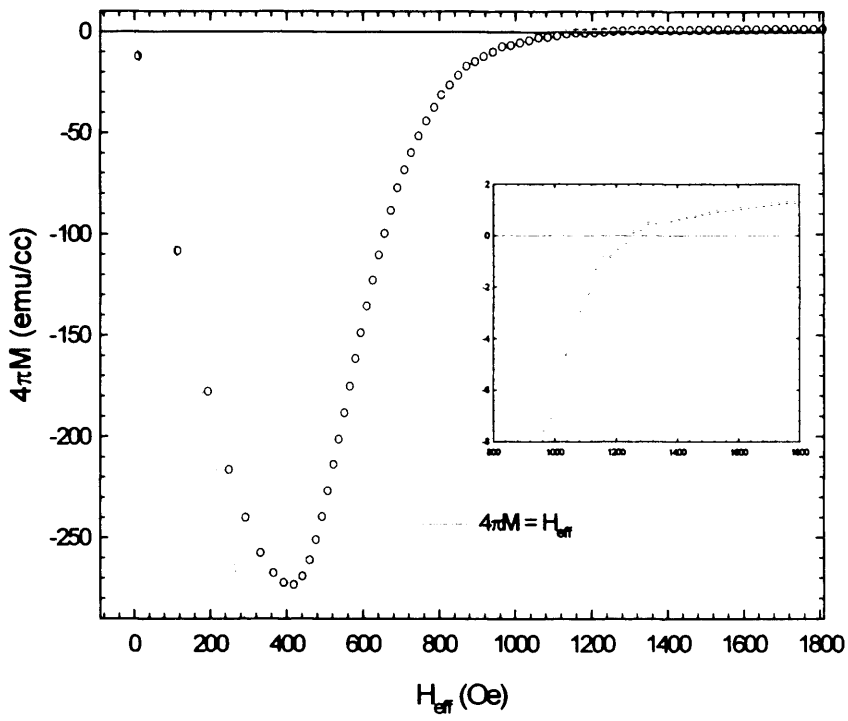

Figure 4.8 Corrected data from measurements at 2K, with H//c, on the C_6Yb sample. The pinning effects are such that it seems that the excursion of the data from $4\pi M = H_{eff}$ is not a good determination of H_{c1}. The absolute value of H_{c2} as determined from $4\pi M = 0$ is well determined, within experimental error.

A comparison of the initial slope of the data with H = -4πM suggests a superconducting fraction of ~96%, as the initial slope of the data in *Figure 4.8* is -0.957. This is in contrast to the superconducting fraction that would be expected from *Chapter 3*, where a core of HOPG is identified, and SEM was used to estimate a volume fraction of 36%. However the superconducting fraction estimate of ~96% may be understood as consistent with the conclusions of overall morphology of the sample. A closed hollow cylinder of superconductor will expel flux the same as an otherwise identical filled cylinder.

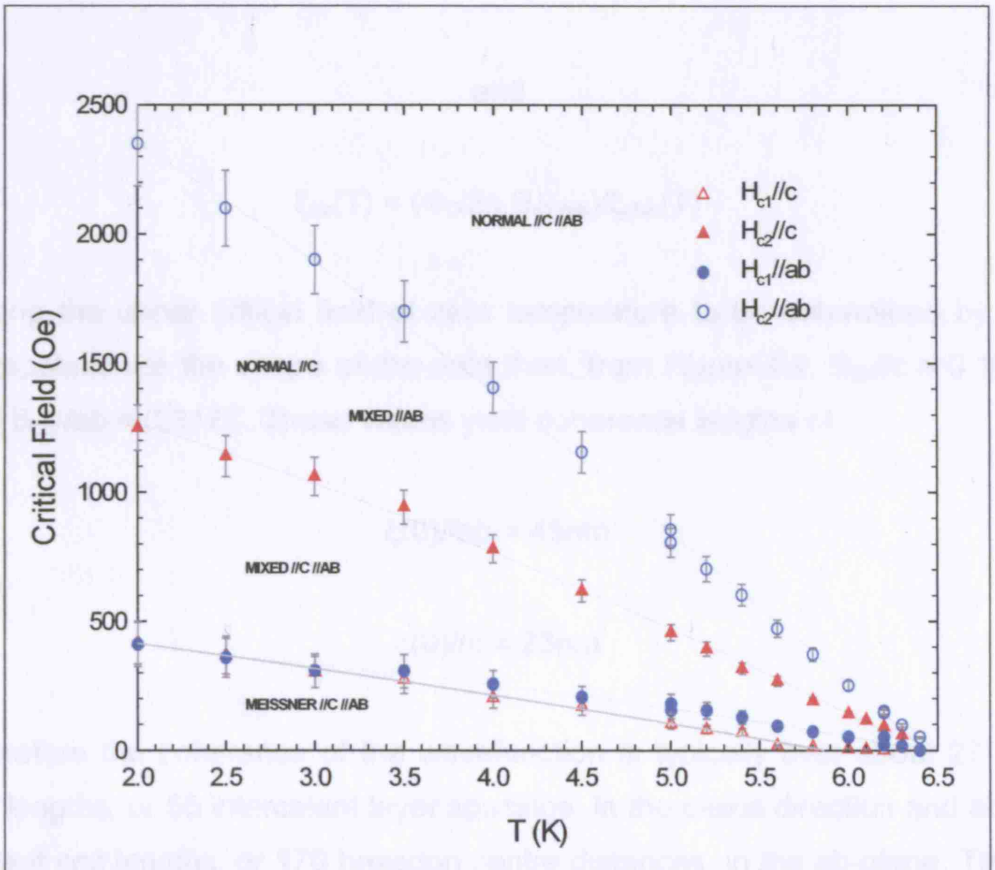

Figure 4.9 Field-temperature phase diagram for C_6Yb. Showing H_{C1} and H_{C2} in each field orientation. Below H_{C1} is the Meissner state where no flux penetrates the sample, between H_{C1} and H_{C2} is the mixed state where flux gradually penetrates, up to H_{C2}. The lines are a guide to the eye, and provide an extrapolation to $H_{C2}(0K)$.

Figure 4.9 shows the Field Temperature phase diagram plotted from measurements of the field dependence of the magnetisation made for various temperatures in both field orientations, *Figure 4.8* being an example for 2K. The three distinct phases of the Type II superconductor are clearly present.

The anisotropy parameter Γ, discussed in *Chapter 2*, is temperature independent and takes an average of 1.84 ± 0.04 below 4.5K.

4.4.4 C_6Yb - Short Anisotropic Coherence Lengths but in the Dirty Limit

Coherence length may be determined from the value of H_{c2} according to *Equation 1.14(a)&(b)*, which may be rearranged to give

$$\xi_{//ab}(T) = \sqrt{(\Phi_0/2\pi.B_{c2//c})}$$

and

$$\xi_{//c}(T) = (\Phi_0/2\pi.B_{c2//ab})/\xi_{//ab}(T)$$

Taking the upper critical field at zero temperature to be determined by the extrapolation to the shape of the data then, from *Figure 4.9*, $B_{c2}//c$ = 0.164T and $B_{c2}//ab$ = 0.317T. These values yield coherence lengths of

$$\xi(0)//ab = 45nm$$

and

$$\xi(0)//c = 23nm$$

Therefore the coherence of the wavefunction is typically over about 27 unit cell lengths, or 55 intercalant layer spacings, in the c-axis direction and about 97 unit cell lengths, or 170 hexagon centre distances, in the ab-plane. These are short compared to the entire range of mean free paths at 4K reported for the class of donor intercalates: 100nm – 100000nm [Dresselhaus 2001], suggesting that C_6Yb may be in the clean limit of type II superconductivity according to *Equation 1.6*.

Figure 4.10 shows values of $\xi(T)$ calculated from $H_{c2}(T)$ and plotted as a function of reduced temperature $t=T/T_C$. The form of $\xi(t)$ is consistent with the predictions of the GL theory, as embodied in *Equations 1.17 & 1.18*, and used

to fit the lines shown in *Figure 4.10*. The constant factor can be used to calculate the values of ξ_0. Given the order of magnitude of $\xi(0)$ in both orientations and an estimate of the ab-plane electron mean free path $\Lambda_{//ab}$ = 44nm, from *Chapter 5*, it is likely that C_6Yb is in the dirty limit.

According to *Figure 4.10*, and assuming the dirty limit, *Equation 1.18* can be arranged to give

$$0.855(\xi_{0//c}\Lambda)^{1/2} = 24.15\text{nm},$$

and

$$0.855(\xi_{0//ab}\Lambda)^{1/2} = 31.08\text{nm}.$$

Thus $\xi_{0//c}\Lambda_{//c} = 797.8\text{nm}^2$ and $\xi_{0//ab}\Lambda_{//ab} = 1321\text{nm}^2$. An estimate of $\Lambda_{//ab}$ = 44nm therefore yields an estimate of $\xi_{0//ab}$ = 30nm. Lacking an estimate of $\Lambda_{//c}$ from ρ_0 it is not possible to estimate $\xi_{0//c}$, however it is expected that $\Lambda_{//c} << \Lambda_{//ab}$ so that $\xi_{0//c} > 18$nm.

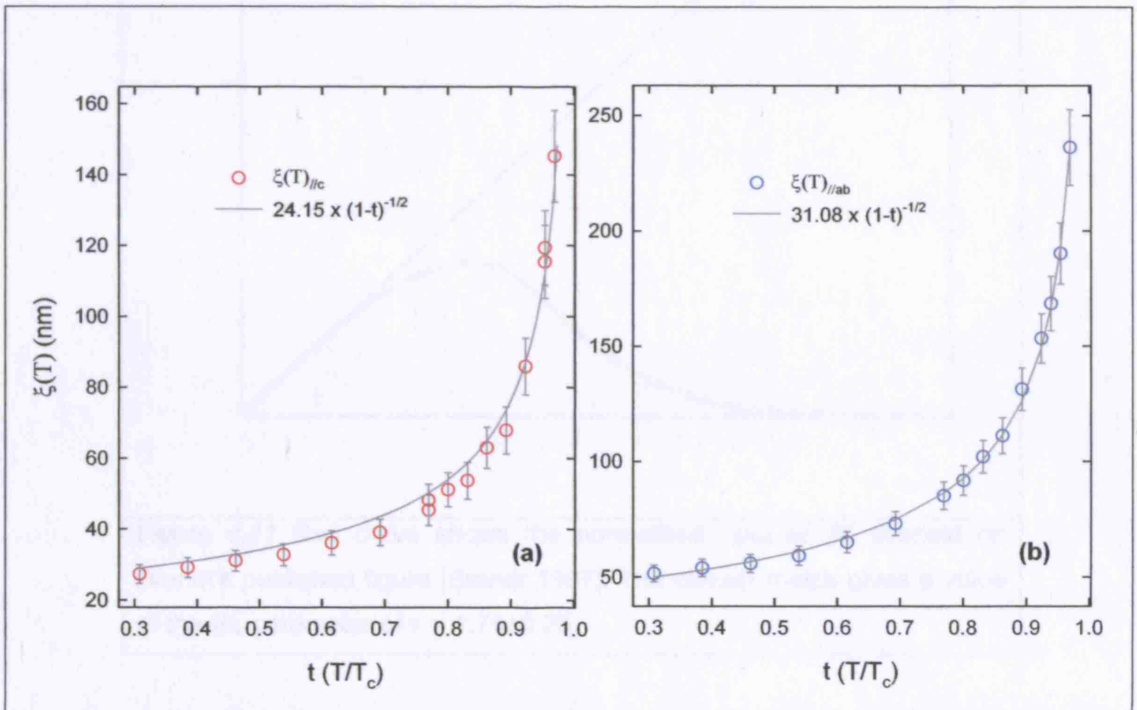

Figure 4.10 Coherence lengths, calculated from *Figure 4.8* according to *Equation 1.14(a)&(b)*, as a function of reduced temperature t = (T/T_c). Lines are a fit to the data with the formulae shown and R values of (a) 0.9935 and (b) 0.9984.

4.4.5 C_6Yb Ginzburg-Landau Parameter is Small

An estimate of the penetration depth in C_6Yb can be gained from the comparison of Brandt's curves [Brandt 1997] to the magnetisation curves in reduced dimension, see *Section 1.4*. *Figure 4.11* shows the experimental data at 2K for both field orientations which fall onto the same curve (red) when using Brandt's renormalization scheme of $B(T)/B_{C2}$ for the abscissa, and an appropriate normalisation for experimental data, namely to $-4\pi M$. The value of κ to which the data qualitatively matches is $\kappa = 1.8 \pm 0.3$, with pinning effects considered. *Figure 4.10* gives approximate values for $\xi_{//ab}(2K) = 50nm$ and $\xi_{//c}(2K) = 27nm$, so that from *Equation 1.7* values for $\lambda(2K)$ can be calculated $\lambda_{//ab}(2K) = 90 \pm 13nm$, and $\lambda_{//c}(2K) = 49 \pm 7nm$.

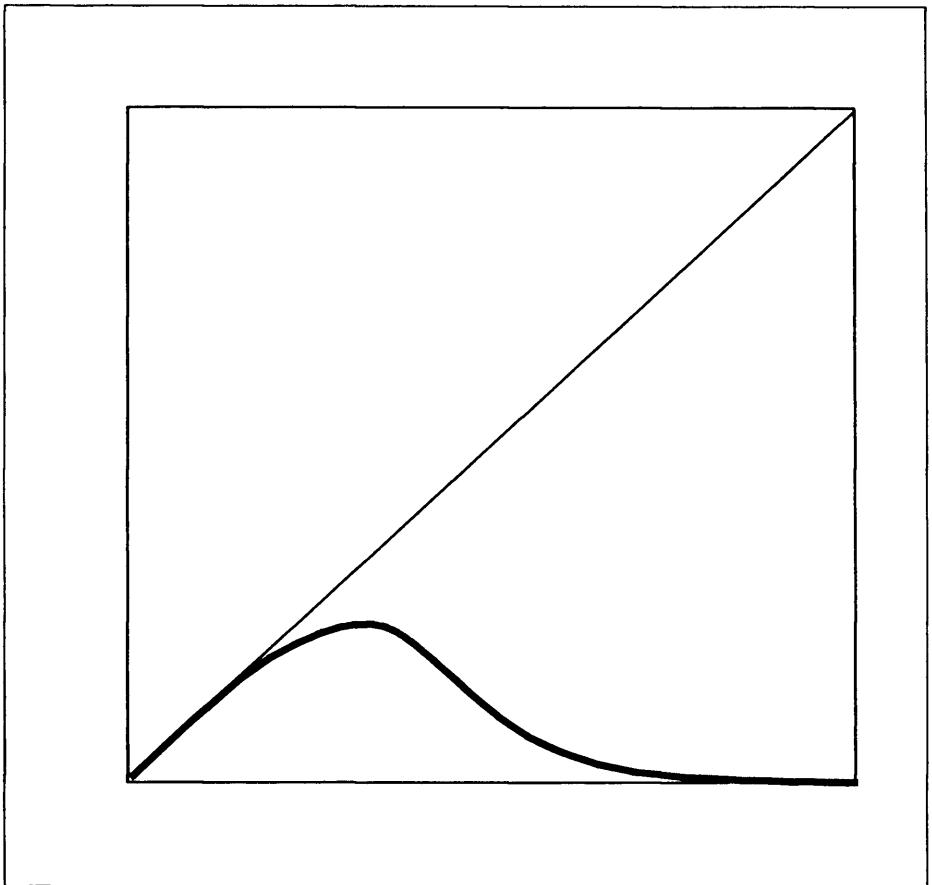

Figure 4.11 Red curve shows the normalised data at 2K overlaid on Brandt's published figure [Brandt 1997]. The closest match gives a value of the GL parameter of $\kappa = 1.75 \pm 0.25$.

4.5 C_6Ca

4.5.1 Superconducting Transition in C_6Ca

Figures 4.12 & 4.13 show a broad transition with a sharp initial drop to a diamagnetic state at 11.5K, for both field orientations, measured in 50Oe.

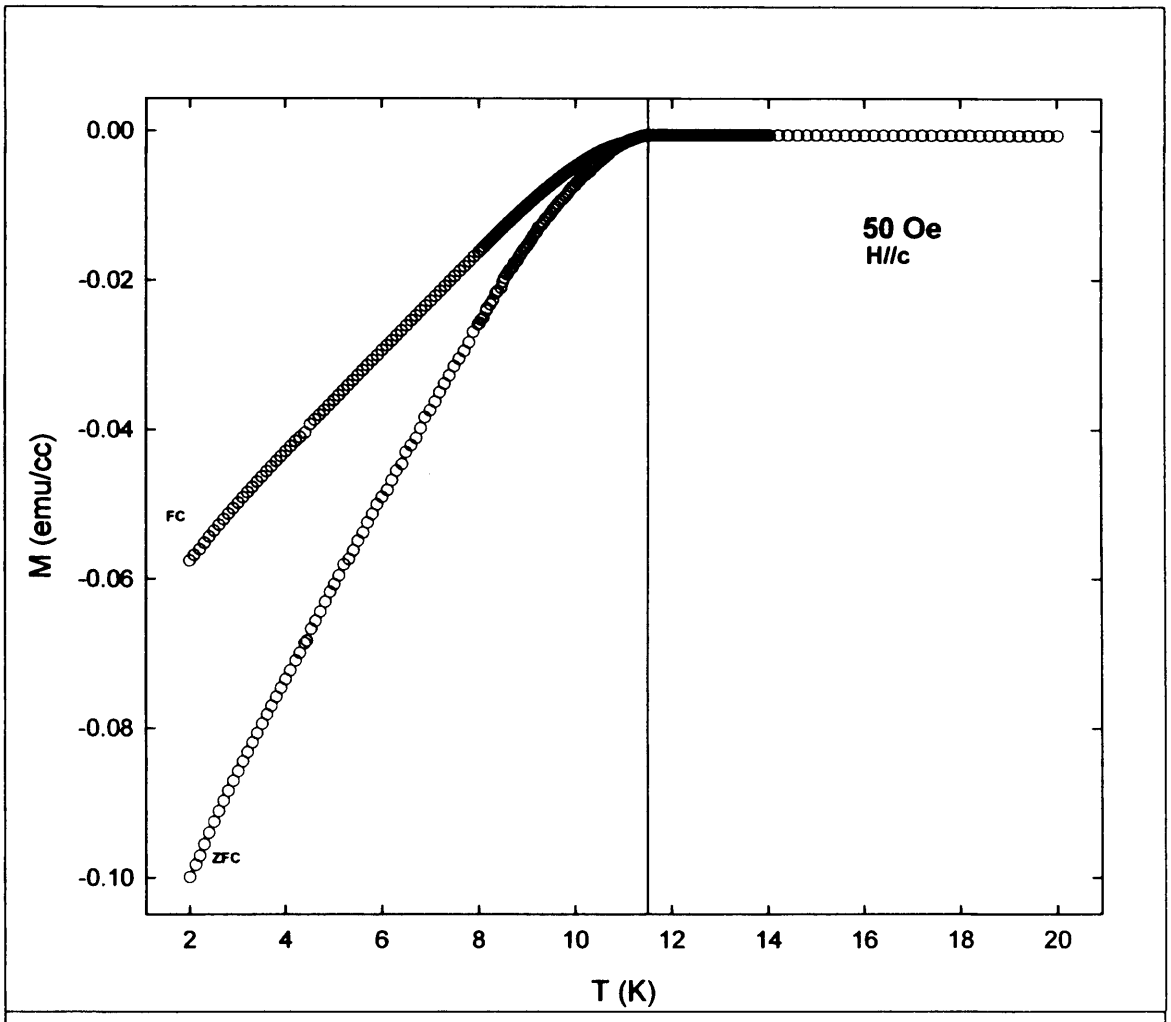

Figure 4.12 Temperature dependence of the magnetization of C6Ca samples showing hysteresis due to flux pinning in both sample orientations. In each orientation the greater magnitude of saturation is for a zero field cooled (ZFC) measurement and the smaller magnitude of saturation is for a field cooled (FC) measurement.

Figure 4.12 gives the full data set, of which *Figure 4.13* is a subset, showing that diamagnetic saturation is not reached at the lowest measured temperature. The data is gathered in ZFCFC measurements as described in *Section 4.4.1* for C_6Yb. The FC measurement once again records the effects of flux line trapping.

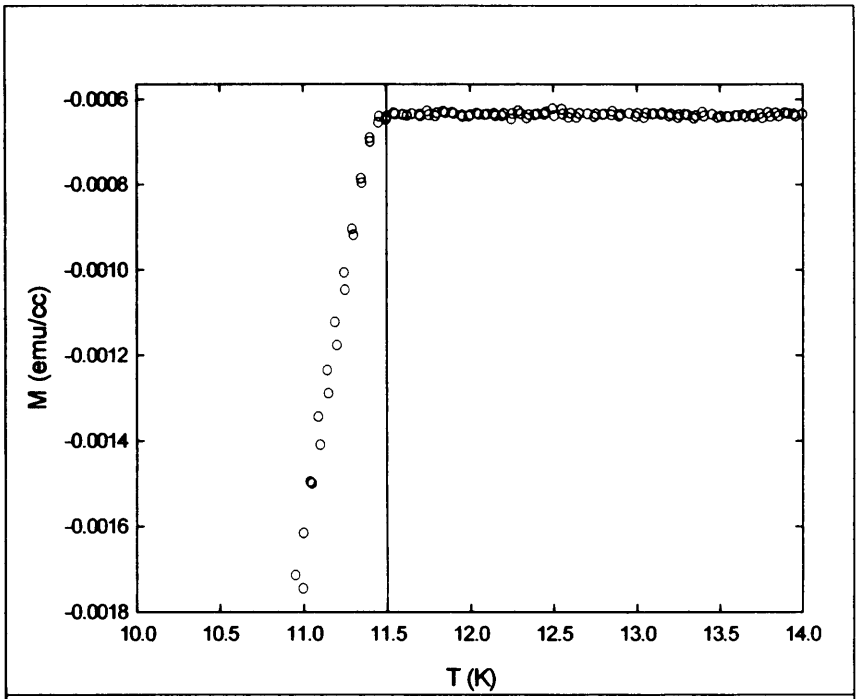

Figure 4.13 Showing the sharp transition to a diamagnetic state at 11.5K for C_6Ca in 50Oe with H//c-axis.

The maximum moments are given in *Table 4.3*. The FC saturation moment as a percentage of the ZFC saturation moment gives a measure of how much of the superconducting volume is removed by pinned flux unable to flow to the surface.

Orientation	ZFC Saturation (emu/cc)	FC Saturation (emu/cc)	FC/ZFC (%)
H//c	-0.0999 ±0.0001	-0.0576 ±0.0001	42%

Table 4.3 Magnitude of the saturation magnetization for ZFC and FC scans. The table shows the ratio FC/ZFC as a percentage as well as (ZFC-FC)/ZFC the difference as a percentage of the ZFC.

4.5.2 Critical Field Determination in C_6Ca

Signal strength from an individual C_6Ca sample disc was found to be quite weak in initial experiments. A set of samples was therefore put together for the final experiments on C_6Ca the data from which are presented here. The samples were arranged into as circular a configuration as possible so as to allow the simplest estimation of the demagnetising factor. The demagnetising field is likely to be underestimated because of the mosaic nature of the

sample in the measurement. The total area of the sample was 9.36mm^2 giving an equivalent diameter of 3.45mm and the sample was 0.5mm thick. Plotting the calculations of Osborn for the demagnetising factors of a general ellipsoid (*Figure 1.5*) and taking the c/a ratio of the sample to be 0.145 values of the demagnetising factor for both field orientations can be found. These are H//c N = 0.81 and H⊥c N = 0.087, according to *Figure 1.5*. Critical field values were determined as for C_6Yb, in *Section 4.4.3*.

4.5.3 Phase Diagram for C_6Ca

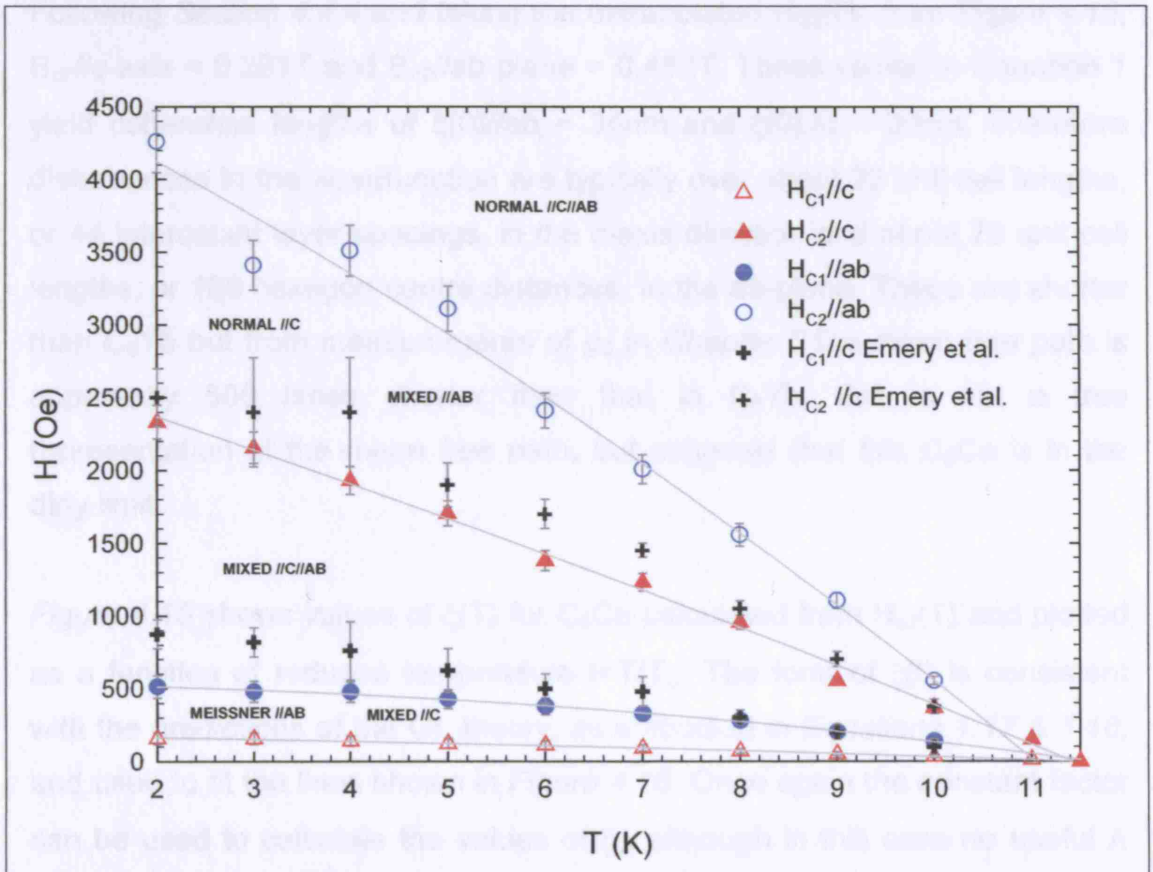

Figure 4.15 Field Temperature phase diagram for C_6Ca. Below H_{C1} is the Meissner state where no flux penetrates the sample, between Hc1 and Hc2 is the mixed state where flux gradually penetrates, up to Hc2 whereupon only the normal state may be observed by magnetometry.

Figure 4.15 gives the temperature dependence of the critical fields. The three distinct phases of the Type II superconductor are clearly labelled. The lines are a guide to the eye.

The anisotropy parameter Γ is temperature independent and takes an average of $\Gamma = 1.73 \pm 0.16$. There is also an anisotropy in the value of H_{c1}. This arises from the poor overlapping of superconducting islands, and the consequent Josephson junctions formed. Such structures are seen to be present in SEM images in *Chapter 3*, which are resolved only by fields parallel to the c-axis. Consequently the first penetration of flux occurs at a lower field with H//c.

4.5.4 C_6Ca Coherence Length - ξ

Following *Section 4.4.4* and taking the extrapolated $H_{C2}(0)$, from *Figure 4.15*, B_{c2}//c-axis = 0.281T and B_{c2}//ab-plane = 0.482T. These values in *Equation 1* yield coherence lengths of $\xi(0)$//ab = 34nm and $\xi(0)$//c = 20nm. Therefore disturbances in the wavefunction are typically over about 22 unit cell lengths, or 44 intercalant layer spacings, in the c-axis direction and about 79 unit cell lengths, or 138 hexagon centre distances, in the ab-plane. These are shorter than C_6Yb but from measurements of ρ_0 in *Chapter 5* the mean free path is apparently 600 times shorter than that in C_6Yb, this is not a true representation of the mean free path, but suggests that this C_6Ca is in the dirty limit.

Figure 4.16 shows values of $\xi(T)$ for C_6Ca calculated from $H_{c2}(T)$ and plotted as a function of reduced temperature $t=T/T_C$. The form of $\xi(t)$ is consistent with the predictions of the GL theory, as embodied in *Equations 1.17 & 1.18*, and used to fit the lines shown in *Figure 4.16*. Once again the constant factor can be used to calculate the values of ξ_0, although in this case no useful Λ values are available. According to *Figure 4.16*, and assuming the dirty limit, *Equation 1.18* can be arranged to give $0.855(\xi_{0//c}\Lambda)^{1/2} = 20.14$ and $0.855(\xi_{0//ab}\Lambda)^{1/2} = 32.5$. Thus $\xi_{0//c}\Lambda_{//c} = 554.9$ and $\xi_{0//ab}\Lambda_{//ab} = 1444.9$.

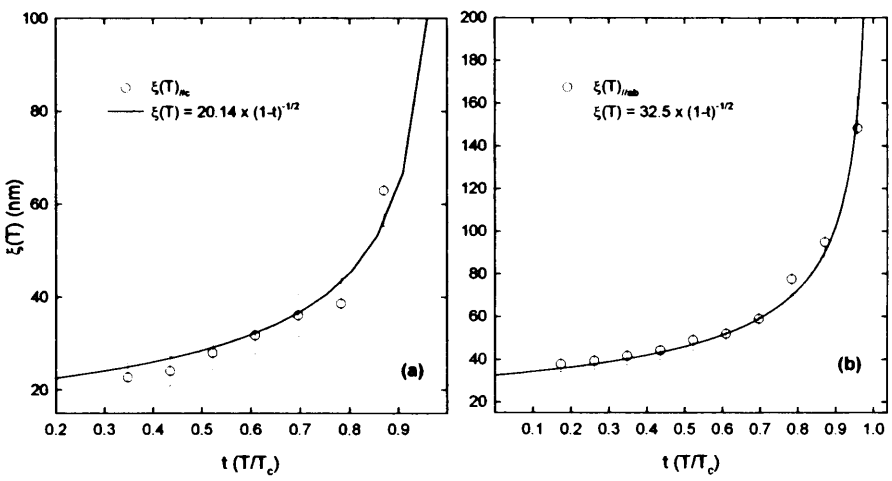

Figure 4.16 Coherence lengths, calculated from *Figure 4.15* according to *Equation 1.14(a)&(b)*, as a function of reduced temperature t = (T/T_C). Lines are a fit to the data with the formulae shown and R values of (a) 0.961 and (b) 0.993.

4.5.5 C_6Ca Ginzburg-Landau Parameter is Small

Following *Section 4.4.5* an estimate of the penetration depth in C_6Ca can be gained from the comparison of Brandt's curves [Brandt 1997] to the magnetisation curves in reduced dimension. In *Figure 4.17* the value of κ to which the data best matches is κ=5, taking into account the irreversible section of the curve arising due to pinning effects. *Figure 4.15* gives a value for $\xi_{//ab}(2K)$ = 38nm, and $\xi_{//c}(2K)$ = 21nm so that from *Equation 1.7* a value for λ(2K) can be calculated to yield $\lambda_{//ab}(2K)$ = 190nm, and $\lambda_{//c}(2K)$ = 100nm.

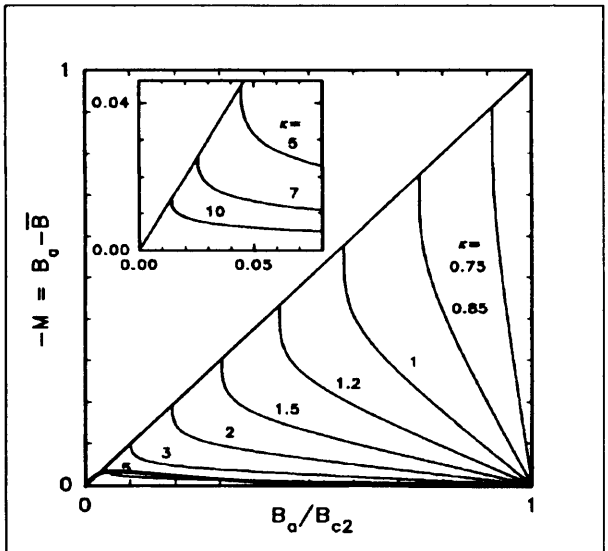

Figure 4.17 Red curve shows the normalised data for C_6Ca at 2K H//c [Brandt 1997].

4.6 Summary

The superconducting parameters for C_6Yb and C_6Ca are summarised in *Table 4.4*. The samples appear to be well described by the GL theory, in the dirty limit. They are Type II with small values of κ.

Parameter	C_6Yb	C_6Ca
T_C	6.5K	11.5K
H_{C1}//ab (2K)	400 ±90Oe	510 ±10Oe
H_{C1}//c (2K)	400 ±90Oe	160 ±40Oe
H_{C2}//ab (2K)	2400 ±170Oe	4200 ±200Oe
H_{C2}//c (2K)	1300 ±90Oe	2300 ±100Oe
Γ	1.8 ±0.1	1.7 ±0.2
$\xi_{//ab}(2K)$	51 ±4nm	38 ±2nm
$\xi_{//c}(2K)$	27 ±2nm	21 ±1nm
$\xi(0)$//ab	45 ±2nm (170 hexagons)	34 ±2nm (138 hexagons)
$\xi(0)$//c	23 ±1nm (55 layers)	20 ±1nm (44 layers)
$\xi_{0//c}\Lambda_{//c}$	797.8	554.9
$\xi_{0//ab}\Lambda_{//ab}$	1321	1444.9
$\xi_{0//ab}$	30 ±2nm	-
$\xi_{0//c}$	> 18nm	-
κ	1.8 ±0.3	~5
$\lambda_{//ab}(2K)$	~90 nm	~200 nm
$\lambda_{//c}(2K)$	~50 nm	~100 nm

Table 4.4 A summary of the superconducting parameters of C_6Yb and C_6Ca.

Chapter 5

Resistivity Measurements

This chapter presents data gathered with an Oxford Instruments MagLab cryogenic resistivity system from four-point measurements on samples synthesised according to the process described in Chapter 3. Data from measurements on ZYA HOPG is also included for the purpose of interpreting the data. Corroborating data gathered from measurements made by Robert P. Smith at the Cavendish Laboratory on samples I synthesised is also included.

5.1 Experimental Method

Resistivity measurements were performed using an as supplied Oxford Instruments MagLab, including a rotating stage. Details of instrument control can be found in the relevant manuals, available from Oxford Instruments.

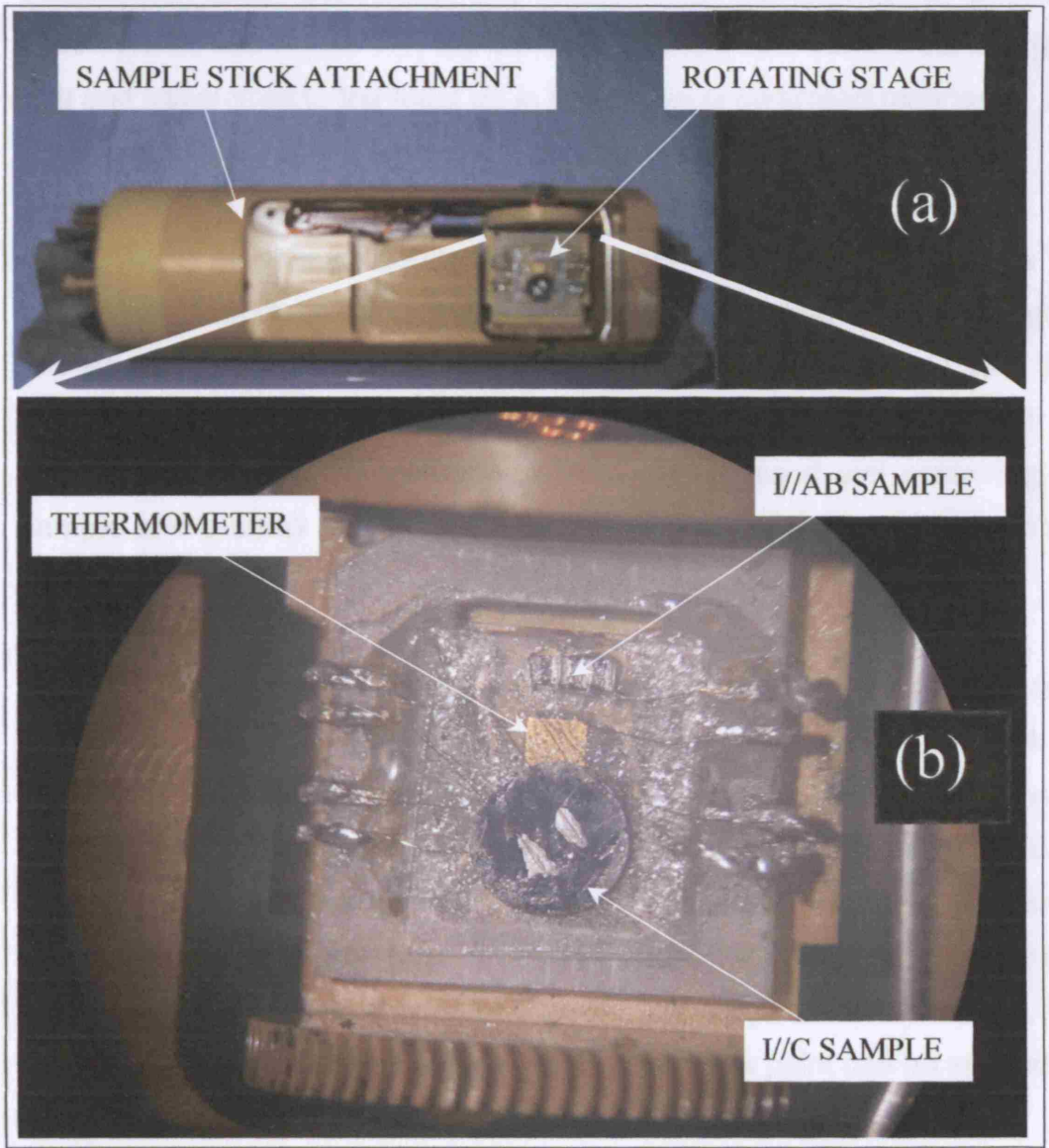

Figure 5.1 (a) The sample stick attachment, with sample stick connectors on the left and rotating sample stage on the right. (b) The rotating sample stage showing the placement of the samples, the contacts and the thermometer under a sapphire base.

The sample stick attachment used is shown in *Figure 5.1(a)*. The rotating sample stage, shown in *Figure 5.1(b)*, houses a sapphire base with solder contacts on the stage nearby. The samples can be seen with gold wire

attached with silver paint connecting them to the solder points. The solder points are connected to the sample stick connectors, as is the thermometer which sits underneath the sapphire base.

A key issue for measurements on such air-sensitive samples is the minimisation of atmospheric exposure of the sample. Since the sample stick attachment does not have any means of maintaining a controlled environment, see *Figure 5.1*, the sample mounting was carried out in a glove bag and transferred to the MagLab in the following controlled manner.

The glove bag was purged three times with helium before two vials, one containing a potassium getter and the other containing the samples and getter, were introduced from the glove box. The glove bag was then purged a further three times. The vial containing getter potassium only was then opened. The bag was considered clean when an exposed face of this potassium does not immediately blacken. The second vial containing the sample and a small piece of potassium was then opened and the contacts made.

Gold 0.25mm wire and RS silver paint with thinner were used for the contacts. The contacts are applied, see *Figure 5.2*, using a small piece of Bluetack and a toothpick as a mount, a smaller piece of Bluetack is applied to the end of the toothpick and the gold wire pressed into it such that the gold wire curves convex side down toward the sample. The position of the wire can then be adjusted using the gentle play of the Bluetack at the base of the toothpick. Once the wire is appropriately positioned with respect to the sample, with plenty of contact over a well-defined region the silver paint can be applied.

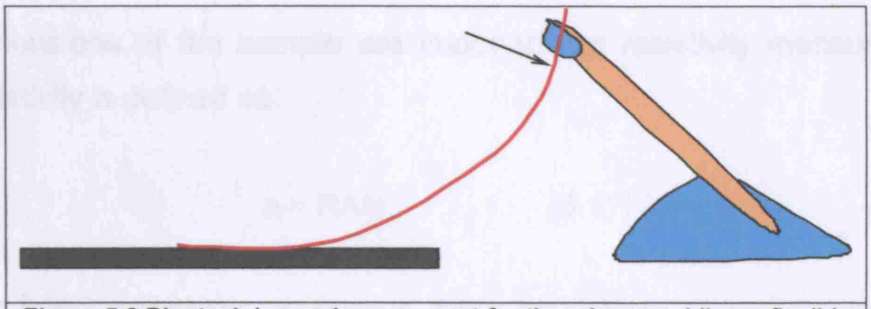

Figure 5.2 Bluetack is used as a mount for the wire, providing a flexible base to adjust the wire until it is in good contact with the sample. After the silver paint is applied and allowed to dry the gold wire (red) is cut at the point indicated by the arrow.

The consistency of the silver paint is of the utmost importance to form good contact. A small amount is applied to wet the sample and cover the wire at the contact region. The sample is then left to allow each contact in turn to cure, before the wire is snipped from close to the Bluetack, indicated by an arrow in *Figure 5.2*. Once all four wires are bonded to the sample the sample is carefully placed on the sapphire base, where it is gently fixed with a small dab of previously outgassed high vacuum grease. The wires are then carefully soldered to the contacts on the rotating stage, see *Figure 5.1*.

The grease provided some protection from the environment once the stage was removed from the glove bag. To provide further protection a plastic bag, with a small piece of potassium in it, was also placed around the sample stick attachment in such a way as to allow it to be connected to the sample stick. In this way the sample stick with attachment could be prepared for the MagLab and the bag removed just before the sample stick was introduced into the controlled environment of the MagLab.

A four wire method was used to reduce the effect of contact resistance, this is achieved since the current passing through the sense leads in a four wire measurement is negligible. A low frequency AC current was used, since lock-in techniques allow smaller currents to be generated stably. The current reversal also removes unwanted thermoelectric voltages. The current was sufficiently large to measure the desired voltage without being large enough to cause self-heating of the sample [Keithley 1998].

The dimensions of the sample are important for resistivity measurements. The resistivity is defined as

$$\rho = RA/s \qquad (5.1)$$

where R is the resistance measured, A the area of the sample perpendicular to the current (I), and s the length over which the voltage (V) is measured.

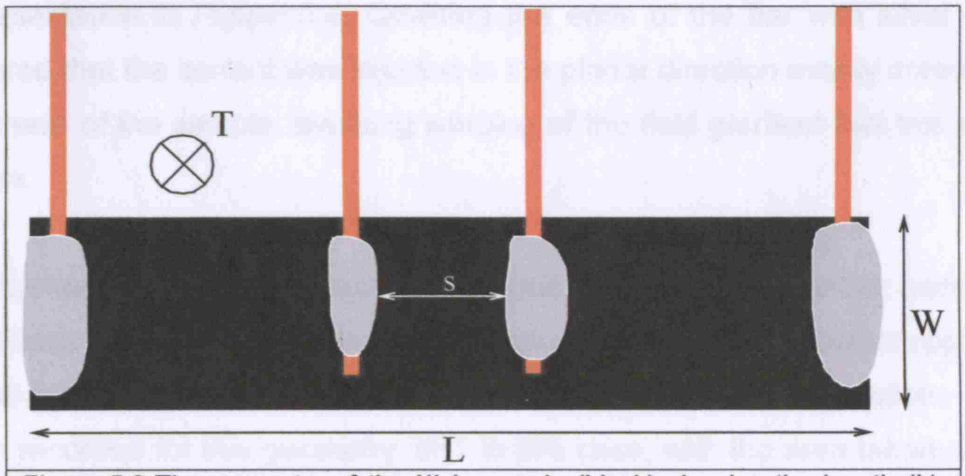

Figure 5.3 The geometry of the I//ab sample (black) showing the length (L), width (W), thickness (T), and the distance over which the measurement was made (s). The gold wires appear in red, and the silver paint contacts in grey.

Samples with appropriate geometries for ab-plane and c-axis resistance measurements were prepared by selecting appropriately shaped dies during the HOPG cutting described in *Chapter 3*. The ab-plane measurements were made on bars, see *Figure 5.3*, with L = 0.3cm, W = 0.1cm and T = 0.05cm. On the bar the potential contacts were made as close as possible to each other without letting the silver paint come into contact, an average *s* = 0.06cm was achieved, measured using a Vernier scale under a microscope. The current contacts were made near the ends of the bar and the silver paint covered the ends of the bar ensuring the current was injected evenly into the layers.

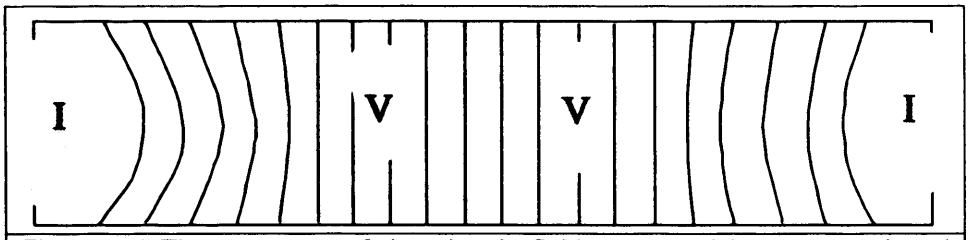

Figure 5.4 The geometry of the electric field generated by contacts I and measured by contacts V.

Minimising *s* ensured that the field lines were as planar as possible before the points at which the measurement was made, as illustrated by the schematic representation in *Figure 5.4*. Covering the ends of the bar with silver paint ensured that the current was injected in the planar direction evenly across the thickness of the sample, avoiding warping of the field gradient that this could cause.

The bar sample and its contacts correspond closely to the optimum geometry [Stephens 1971], thus requiring no correction to measure the correct apparent resistivity. The disc however is not well optimised, and no corrections have been recorded for this geometry, s=T in this case, with the area taken as the area of the disc.

Additional measurements for calibration of the system using, for instance, a well characterised 1Ω resistor have not been made. Consequently the absolute value of resistivity cannot be obtained, however the main goal of this work is to confirm the superconductivity demonstrated in *Chapter 4*.

5.2 Resistivity of Graphite

Measurements of the behaviour of the HOPG, the basis for the samples measured, allow the behaviour of the underlying material to be distinguished from that of the new material. Measurements of the resistivity of HOPG have been made before [Matsubara 1990, Uher 1987, Du 2005]. Additional measurements for HOPG using the same MagLab as used for the samples of interest are required. This is not only because they can be taken in the same

ranges as the experiments on C_6M but also as no calibration data has been taken.

Figure 5.4 shows data from a measurement of the ab-plane (i//ab) and c-axis (i//c) resistivity of ZYA HOPG, taken in zero field with an AC current of 1mA and a frequency of 110Hz, thus avoiding potential interference from UK mains at 50Hz – this is rarely exactly 50Hz and the interested reader is pointed toward the tracking websites available [UK Mains]. The samples have effective dimensions s=0.06cm and A=0.1cm x 0.05cm and s=0.05cm and $A=\pi \times 0.25^2 cm^2$, for i//ab and i//c respectively.

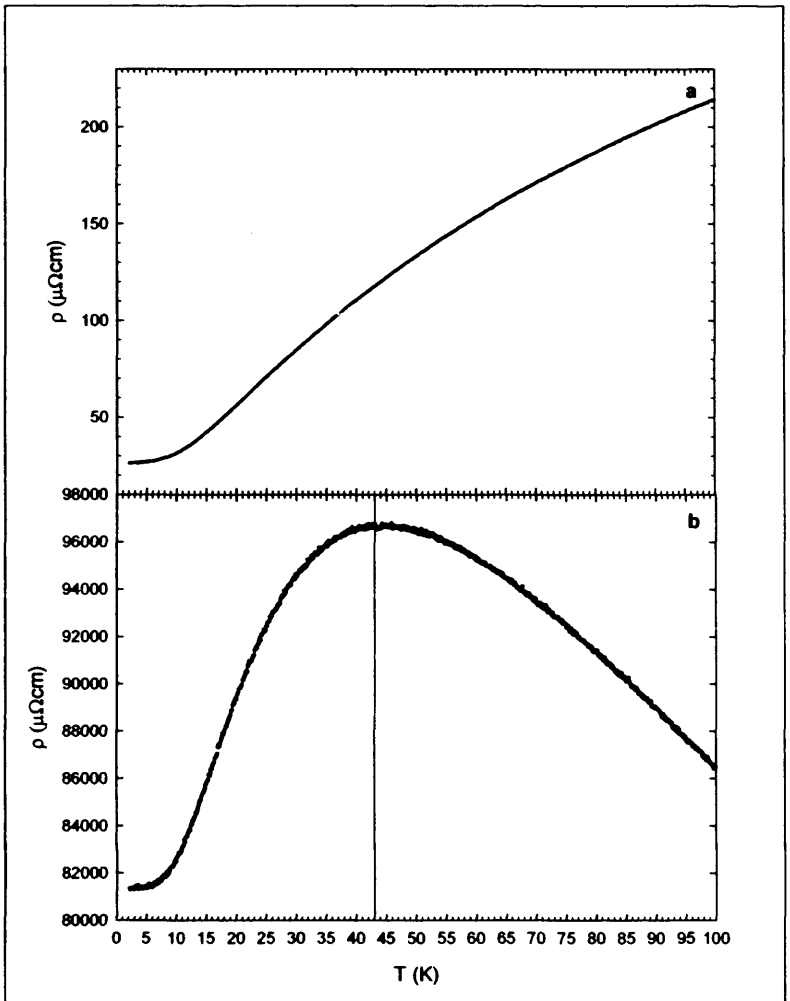

Figure 5.4 Graphite, in the form ZYA HOPG, measured in zero field with an AC current of 1mA and frequency 110Hz. a) The current in the ab-plane (i//ab) with effective dimensions s=0.06cm and A=0.1cm x 0.05cm. b) The current along the c-axis (i//c) with effective dimensions s=0.05cm and $A=\pi \times 0.25^2 cm^2$. The distinctive anisotropy is typical of HOPG.

Residual resistivity ratios (RRR), given in *Table 5.1*, are in reasonable agreement with previous measurements. The RRR of Du et al. for the i//ab geometry is equivalent to the data presented here, to two significant figures. The i//c data of Matsubara et al. is of the same order. The published resistivities at each temperature are an order of magnitude lower in the i//ab geometry and an order of magnitude higher in the i//c geometry. Given that the MagLab is not calibrated it must be accepted that the absolute values of resistivity are unavailable from this data. These measurements therefore form a basis for the qualitative analysis of the succeeding data on C_6Yb that is consistent with previous measurements but carried out in a near identical fashion.

	ρ_{200K} (ρ_{273K}) - μΩcm	$\rho_{4.2K}$ - μΩcm	RRR	Author
i//ab	16.6 (200K)	1.5	11.06	Du 2005
i//ab	287.2 (200K)	26.52	10.83	Weller
i//c	109300 (273K)	188900	0.579	Uher 1984
I//c	600000 (273K)	580000	1.034	Matsubara 1990
i//c	81340 (273K)	49080	1.657	Weller

Table 5.1 This table gives the resistivities published for i//ab and i//c [Du 2005, Uher 1984, Matsubara 1990] and compares this to the values from data gathered here.

5.3 Resistivity of Samples with C_6Yb and HOPG substrate

Resistivity measurements on C_6Yb at various temperatures and in various applied fields were performed on samples with an AC current of 1mA and 110Hz, in the cryogenically temperature controlled environment provided by an Oxford Instruments MagLab. The voltage was measured in the i//ab geometry with A=0.1cm*0.05cm and s=0.06cm, and in i//c with $A=\pi*0.252cm^2$ and s=0.05. The field was applied in one of these two directions, H//ab and H//c. The resistivity was then calculated and is presented here. Measurements were also made by R. P. Smith at the Cavendish Laboratory, using an Adiabatic Demagnetisation Refrigerator, without active temperature control.

5.3.1 Resistivity Confirms Transition in C_6Yb

Figure 5.4 presents the temperature dependence of the resistivity of the C_6Yb sample measured on the MagLab in zero field with the AC current of 1mA and 110Hz. The data confirms the transition to a zero resistance state for current in both directions. The zero resistance state is manifest in fluctuations about zero between small negative and positive resistivities. At 7K ρ_0 in the ab-plane is 12.47μΩcm and in the c-axis direction it is 2627μΩcm.

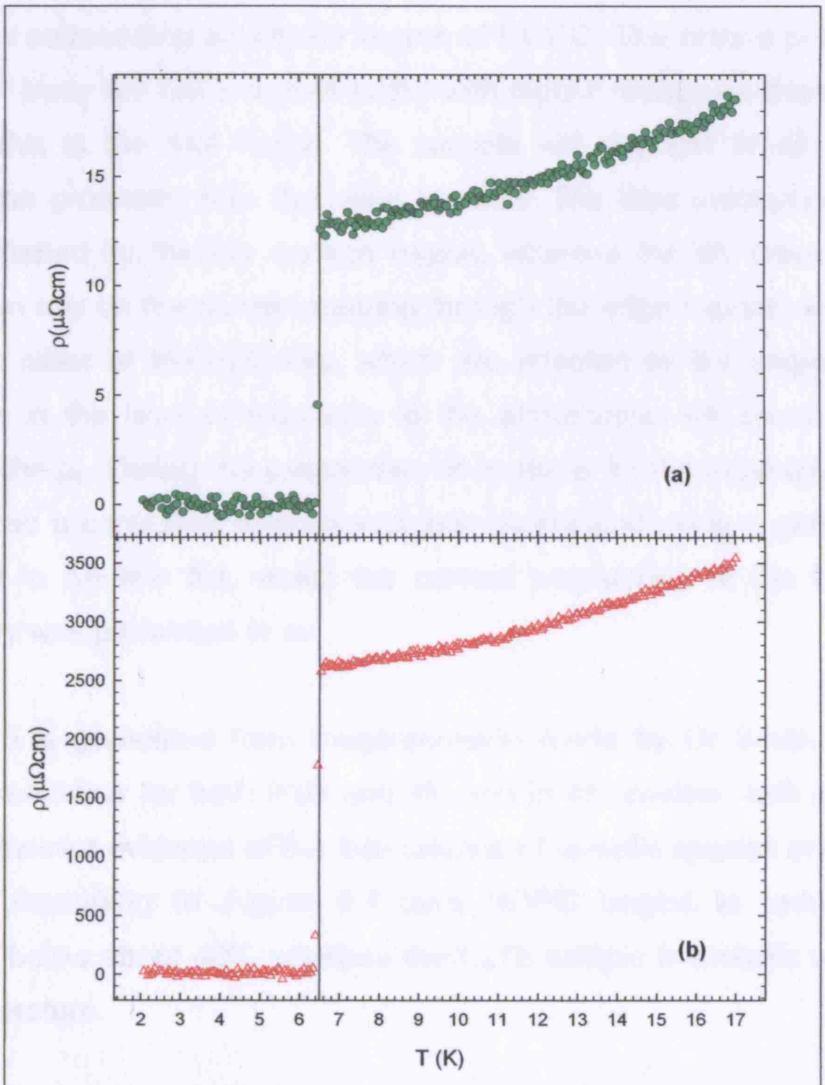

Figure 5.5 Resistivity measurements performed in zero field on samples of C_6Yb with (a) i//ab-plane, A=0.1cm*0.05cm and s=0.06cm (green) and (b) i//c-axis, A=π*0.25^{2}cm^2 and s=0.05cm (red) using the MagLab and a four-point probe technique. At 7K the residual resistivity in the ab-plane is 12.47μΩcm and in the c-axis direction it is 2627μΩcm.

The ρ_0 values exhibited in *Figure 5.4* compare favourably with values of 15.05μΩcm and 6900μΩcm measured since by Dr. R. P. Smith. However, there is a discrepancy in the ρ_0 values for i//c. This discrepancy of 4273μΩcm makes the value recorded by Dr. Smith 263% of the value recorded here. There are two factors that may separately or in combination cause this discrepancy. A 5mm disc sample supplied to Dr. Smith was cut into three, and the middle section was used for the measurements. The sample is understood from *Chapter 3* to be composed of a cylindrical region of intercalate surrounding an interior region of HOPG. The central part with the edges cut away will have current paths with higher resistance than an intact sample, this is the first factor. The sample will degrade in air, and that degradation proceeds from the edge inwards. The i//ab measurements are mainly affected by the top surface region, whereas the i//c measurements once again rely on the current passing through the edge regions, what are in effect the sides of the cylinders, which are affected by the degradation. A difference in the level of exposure to the atmosphere will cause a strong effect on the ρ_0. During the preparation of contacts for the measurements on the MagLab a controlled environment was maintained using a glove bag as described in *Section 5.1*, whilst the contact preparation at the Cavendish Laboratory was performed in air.

Figure 5.5 is generated from measurements made by Dr Smith. It shows metallic behaviour for both i//ab and i//c and in comparison with *Figure 5.4* provides indirect evidence of the intercalation of metallic species into the host graphite. According to *Figure 5.4* pure HOPG begins to reduce c-axis resistivity below about 40K, whereas the C_6Yb sample is metallic well above this temperature.

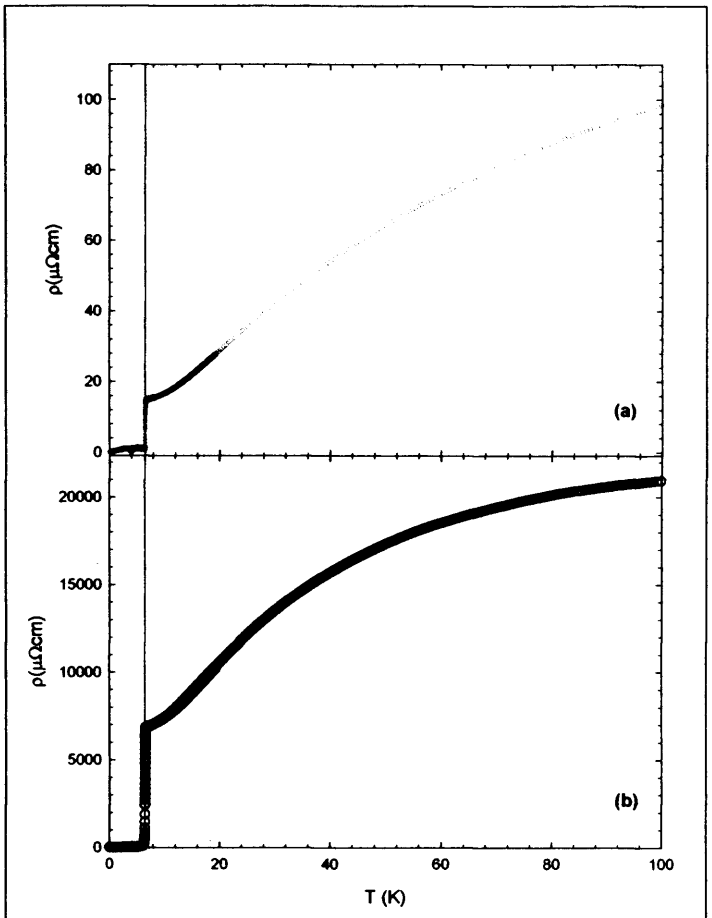

Figure 5.6 Data gathered by Dr R. P. Smith of the Cavendish Laboratory. This data shows the metallic nature of the sample in both high symmetry directions. a) i//ab b) i//c.

Figure 5.6(a) shows the ab-plane resistivity, this may be compared to *Figure 5.1(a)* in conjunction with *Tables 5.1 & 5.2*. The introduction of the metal species produces a smaller RRR suggesting the new metal, though it has a lower resistivity, has more impurities. This can be understood to arise from the additional effect of intercalation, in sum with the original impurity level of the HOPG host.

Figure 5.6(b) may likewise be compared to *Figure 5.1(b)*, in conjunction with the *Tables*. The metallic behaviour shown in *5b* is in sharp contrast to the behaviour of pure HOPG that only becomes metallic below about 40K. The RRR, given in *Table 5.2*, also becomes typical of an alloy, rather than of a semiconductor. This metallic component is indirect evidence of the

intercalation of metal ions into the graphite lattice, and the consequent formation of an alloy like metal in the c-axis direction.

Comparison of *Figure 5.5(a)* and *Figure 5.5(b)* highlights that the ab-plane resistivity is more than two orders of magnitude lower than the c-axis resistivity.

	ρ_{100K}	$\rho_{6.8K}$	RRR	Author
i//ab	98.85μΩcm	14.95μΩcm	6.612	Smith
i//c	20959μΩcm	6870μΩcm	3.051	Smith

Table 5.2 RRR for both current directions from measurements by Smith.

5.3.2 Field Dependence of T_c and ρ_0

Measurements of the temperature dependence of the resistivity of the C_6Yb sample were made at a series of 5 fields, 0 to 5000Oe in steps of 1000Oe, using the MagLab. The measurements were made using a four point probe technique on the MagLab with a current of 1mA at 110Hz. *Figure 5.6* shows this series of superconducting transitions for C_6Yb measured in *a*) the i//ab geometry and *b*) the i//c geometry both with the field in the ab-plane, H//ab. *Figure 5.7* shows the same, but with H//c. In order to achieve the two different field orientations a rotating stage sample stick was used to rotate the samples with respect to the field.

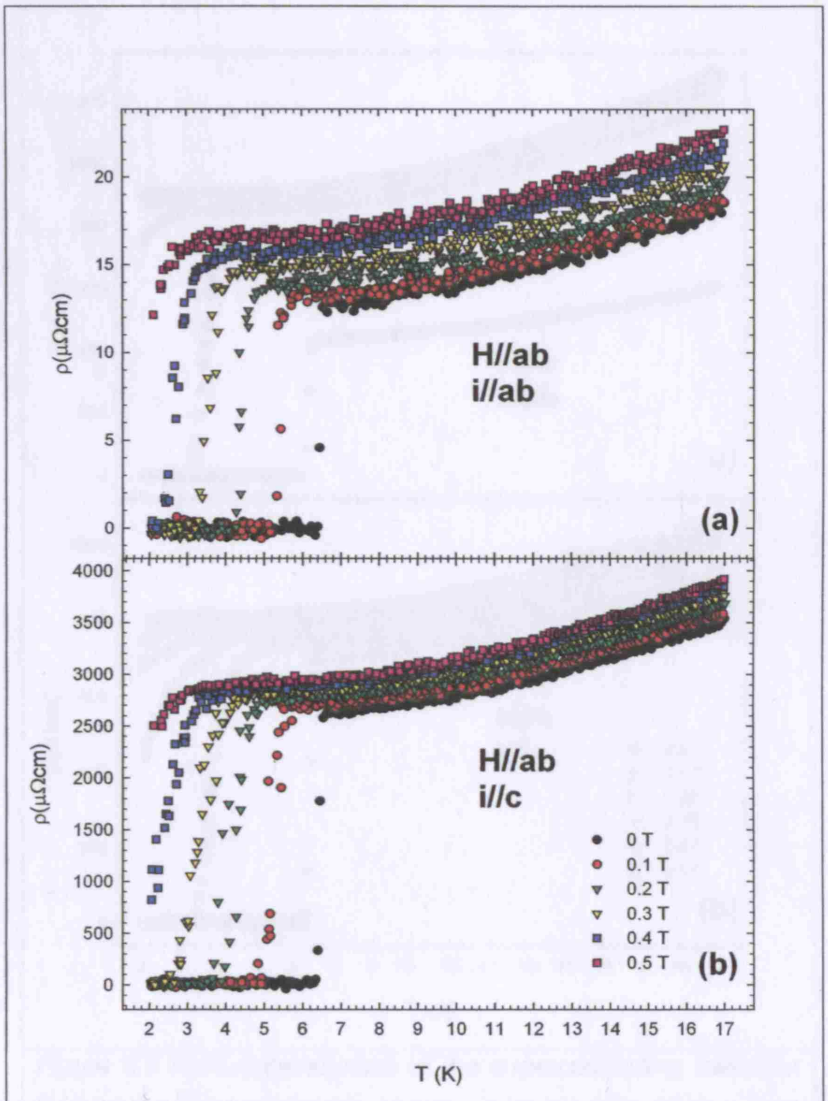

Figure 5.7 Field dependences of the superconducting transition for (a) H//ab i//ab and (b) H//ab i//c. The transition is suppressed by the field in all cases, and there is a response of ρ_0 to the application of field, but little change in the character of the transitions.

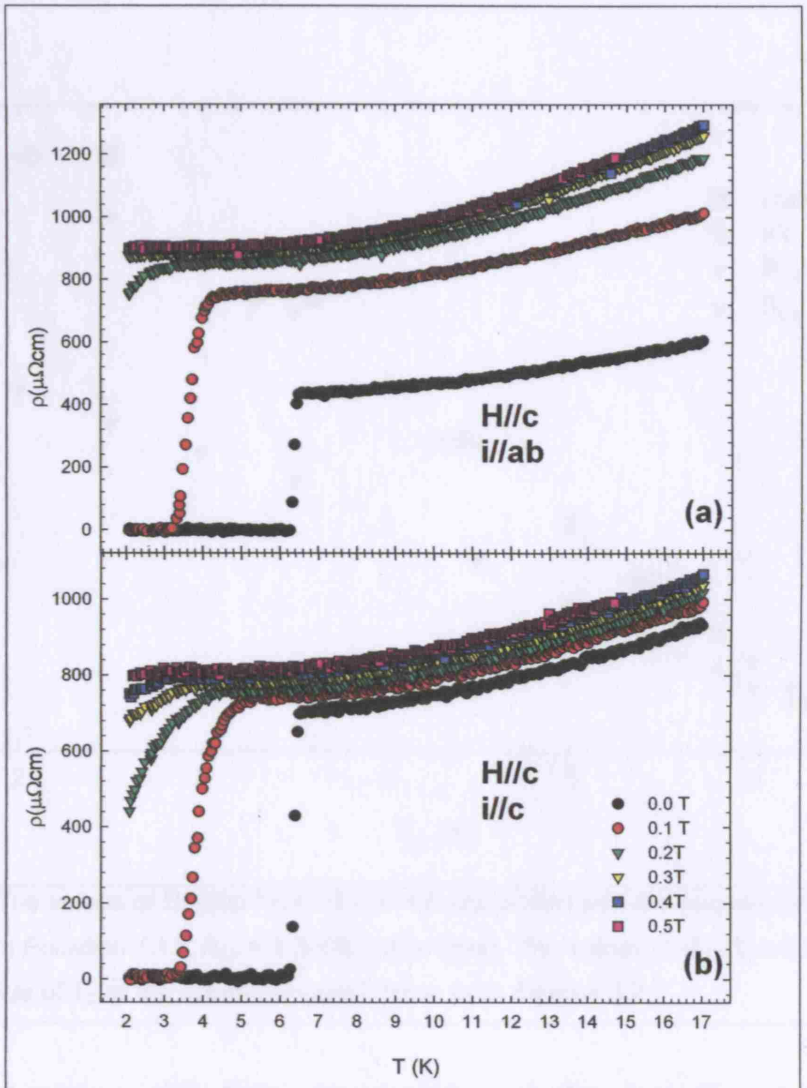

Figure 5.8 Field dependences of the superconducting transition for (a) H//c i//ab and (b) H//c i//c. The transition is suppressed by the field in both cases, and there is a response of ρ_0 to the application of field, but little change in the character of the transitions. The difference between the ρ_0 response to applied fields is highlighted in *Figure 5.9*.

The temperature of the transition in *Figures 5.7 & 5.8* are plotted as phase diagrams in *Figure 5.9 & 5.10*. From *Section 1.6* for H//ab it is expected that superconductivity will be nucleated at a higher field H_{C3} according to *Equation 1.15*. The phase diagram for H//ab should therefore show a transition at a given temperature at a higher field.

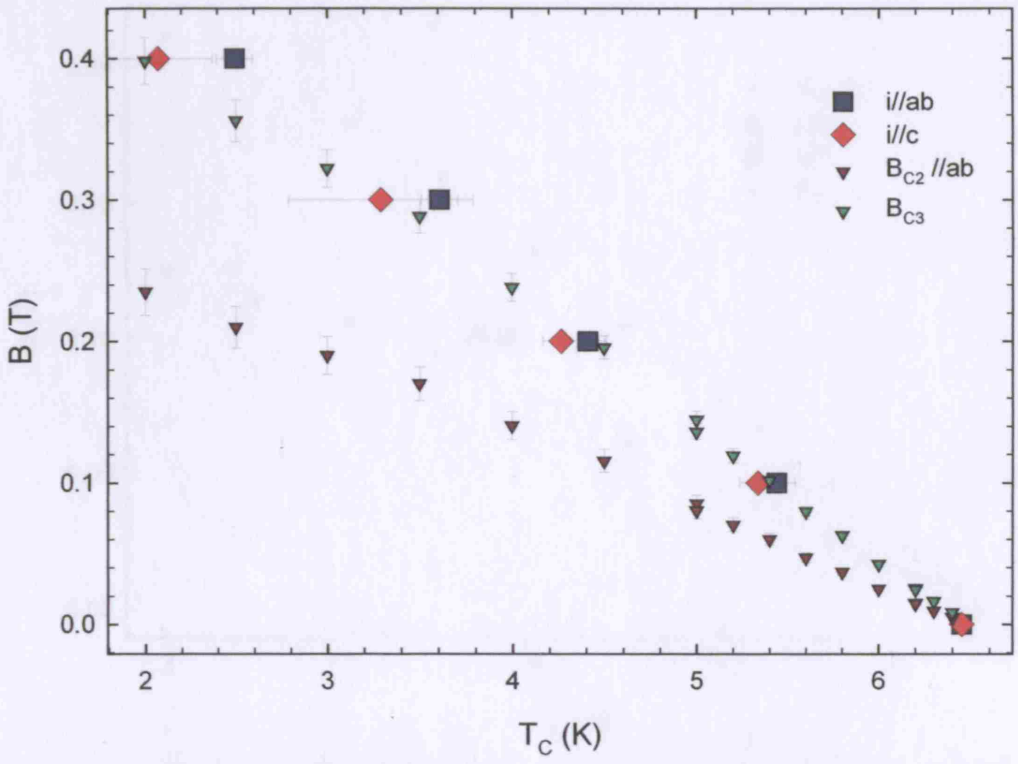

Figure 5.9 The values of B_{C2}//ab from *Figure 4.8* are plotted with the nucleation field values derived from *Equation 1.15*, $B_{C3} = 1.695B_{C2}$ (triangles). The values of (T_C,B) are established from the value of T_C at the maximum dρ/dT taken from *Figures 5.7*.

Figure 5.9 shows the field dependence of the transition temperature compared to the upper critical field B_{C2} from *Figure 4.8*. Plotting *Equation 1.15*, $B_{C3} = 1.695H_{C2}$, shows the surface sheath behaviour expected from discussion in *Section 1.6*. The nucleation of superconductivity may occur in a field parallel to the surface higher than the upper critical field. However, in a field perpendicular to the surface a surface sheath is not expected. The dependence of the transition on the field in the H//c direction, plotted in *Figure 9*, does not show superconductivity much above H_{C2}.

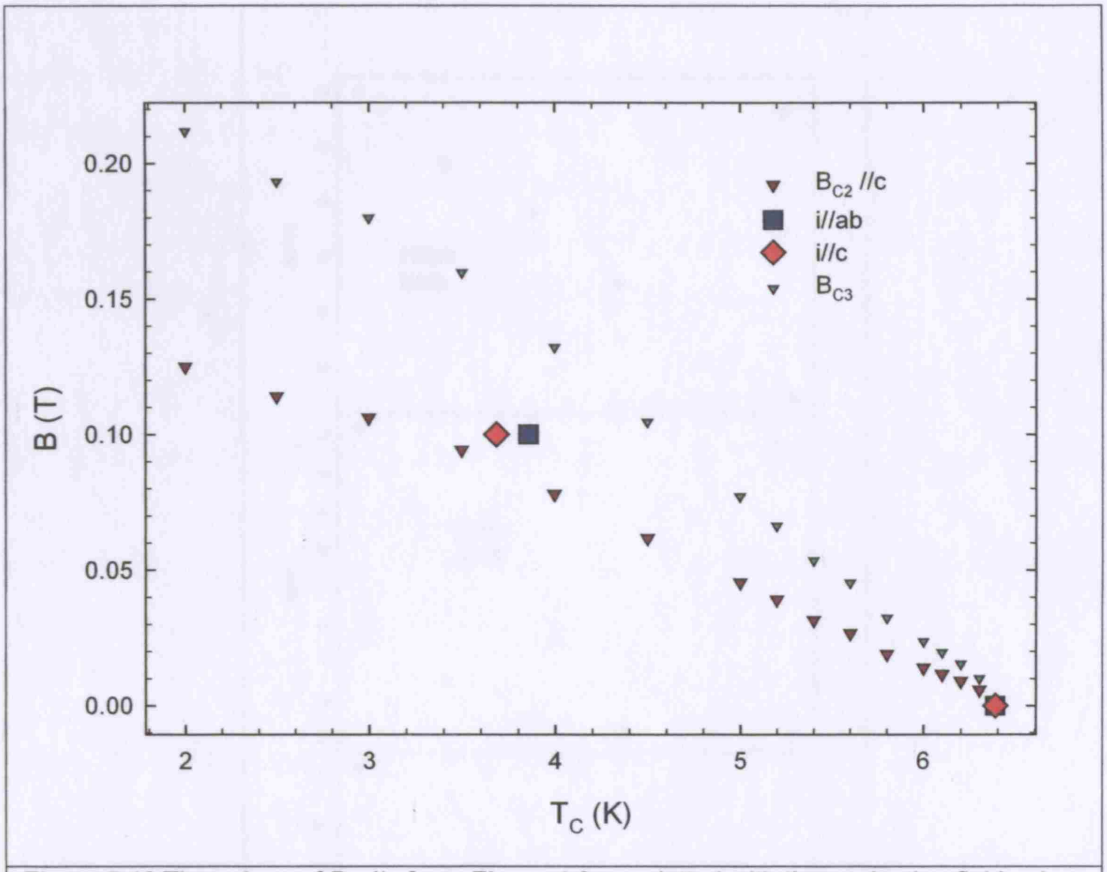

Figure 5.10 The values of B_{C2}//c from *Figure 4.8* are plotted with the nucleation field values derived from *Equation 1.15*, $B_{C3} = 1.695B_{C2}$ (triangles). The values of (T_C,B) are established from the value of T_C at the maximum dρ/dT taken from *Figures 5.8*.

5.3.3 Deriving the mean free path

The ρ_0 values from the data given in *Figure 5.7 & 5.8* allow the mean free path (Λ) to be derived in conjunction with *Equation 1.4*. *Figure 5.11* gives the calculated mean free paths on the basis of the approximation that the Fermi surface is of uniform radius equal to that of C_8K. Each of the geometries is accounted for.

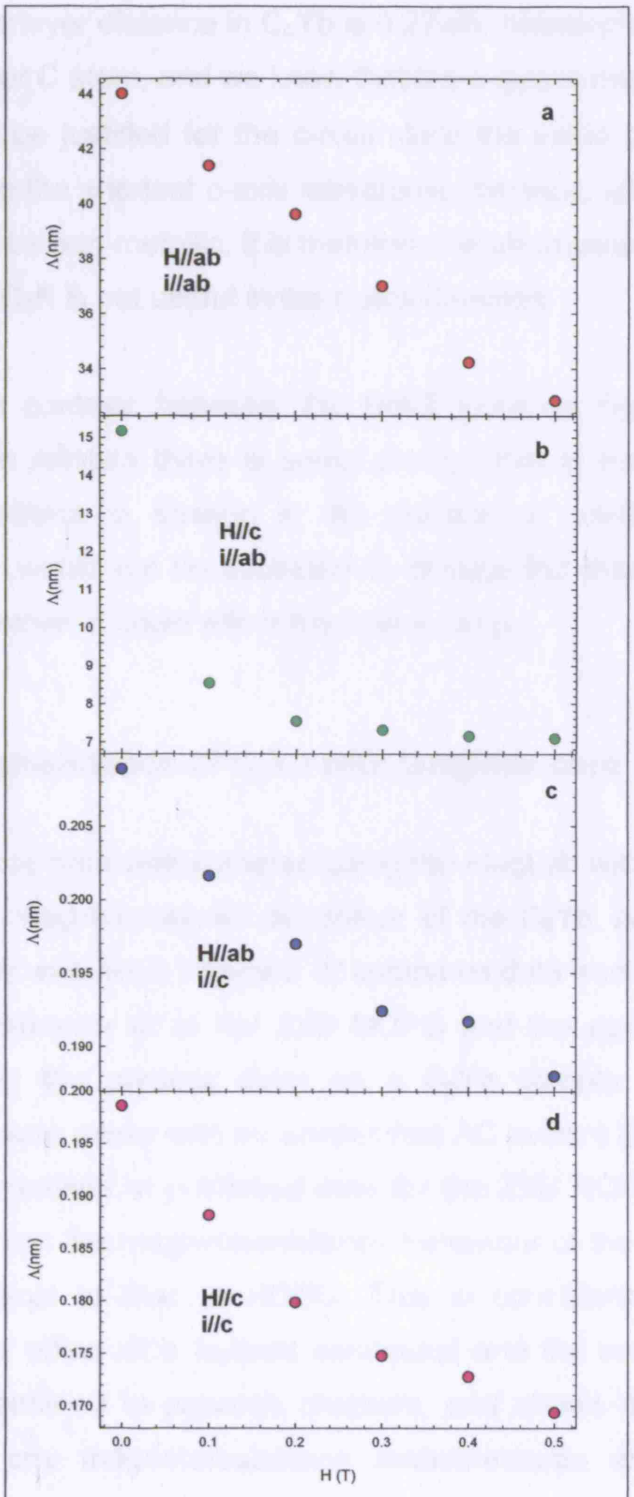

Figure 5.11 Mean free path calculated from ρ_0 assuming an isotropic uniform k_f equal to that of C8K. a) & b) i//ab with H//ab and H//c respectively. c) & d) i//c with H//ab and H//c respectively.

The shortest interlayer distance in C_6Yb is 0.27nm, between an Yb ion and its nearest neighbour C atom, and we know that the c-axis is metallic. The use of $k_F(C_8K)$ can not be justified for the c-axis since the value of Λ produced is then shorter than the shortest c-axis interatomic distance, which would mean the c-axis would be non-metallic. It is therefore the approximation of the Fermi vector to that of C_8K is not useful in the c-axis direction.

Significantly the contrast between the H=0T point in *Figure 11a & 11b* suggests that on rotation there is some change that is not intrinsic to the sample. For instance a change in the position or contact area of the contacting wires would not be expected to change the measured transition temperature, however it could affect the measured ρ_0.

5.3.4 Magnetoresistance of C_6Yb with Graphite core

Magnetoresistance data was gathered using the MagLab with the intention of determining the magnetoresistive behaviour of the C_6Yb. An AC current of 10mA and 110Hz was used. *Figure 5.12* compares data from a measurement published by Stamenov et al. for ZYB HOPG and the equivalent data set measured during the present study on a C_6Yb sample. The Stamenov measurements were made with an unspecified AC current at 1230Hz. It can be seen by comparison of published data for the ZYB HOPG with the data presented here that the magnetoresistance behaviour of the C_6Yb sample is apparently identical to that of HOPG. This is consistent with the large magnetoresistive effect of a layered semimetal and the morphology of the sample, as determined in previous chapters, and shows that the principle component of any magnetoresistance measurements are unfortunately dominated by the HOPG core.

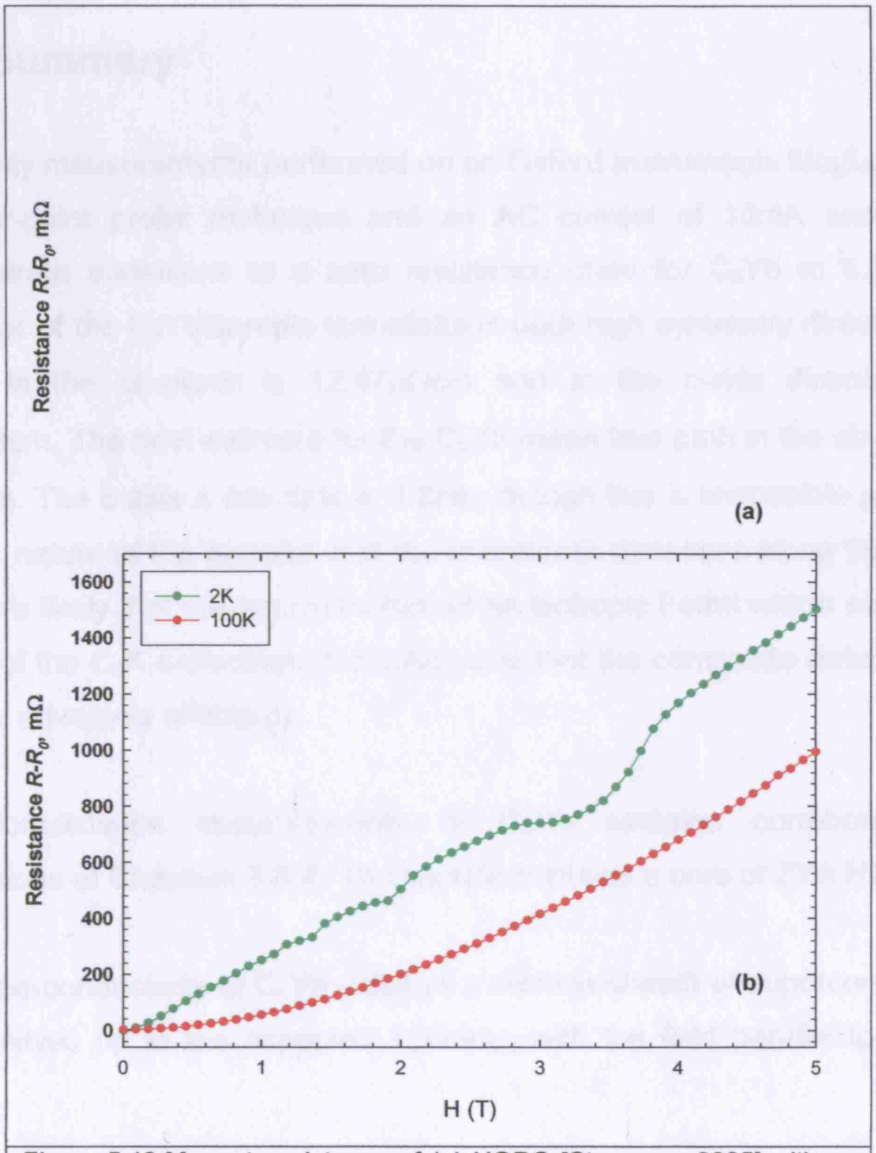

Figure 5.12 Magnetoresistance of (a) HOPG [Stamenov 2005] with an unspecified AC current and a frequency of 1230Hz and (b) a C6Yb sample with an AC current of 10mA and 110Hz. (a) and (b) are both H//c i//ab measurements but (a) is made using a van der Pauw geometry. Comparison of the 2K (green) and 100K (red) between (a) and (b) shows that the dominant contribution to the magnetoresistance of the C6Yb sample was due to the core of ZYA HOPG.

5.4 Summary

Resistivity measurements performed on an Oxford Instruments MagLab using the four-point probe technique and an AC current of 10mA and 110Hz demonstrate transitions to a zero resistance state for C_6Yb at 6.5K. The character of the C_6Yb sample is metallic in both high symmetry directions. At 7K ρ_0 in the ab-plane is 12.47$\mu\Omega$cm and in the c-axis direction it is 2627$\mu\Omega$cm. The best estimate for the C_6Yb mean free path in the ab-plane is Λ=44nm. The c-axis Λ estimate is 0.2nm, though this is impossible given the metallic nature of the material and the interatomic distances along the c-axis. It is more likely that the approximation of an isotropic Fermi vector equivalent to that of the C_8K s-electrons is flawed, and that the composite nature of the material adversely affects ρ_0.

Magnetoresistance measurements of C_6Yb samples corroborate the conclusions of Chapters 3 & 4. The sample contains a core of ZYA HOPG.

The superconductivity of C_6Yb displays a surface sheath of superconductivity that survives up to the expected $1.695H_{C2}$ with the field parallel to the ab-plane.

Chapter 6

Initial Studies of C_6Yb $T_C(P)$

This chapter presents data from measurements of the pressure dependence of the superconducting transition in C_6Yb. This investigation of the pressure dependence of the superconducting transition temperature in C_6Yb was carried out using magnetization measurements and resistivity measurements made in Cambridge. I carried out the magnetization measurements at UCL using a miniature CuBe piston clamp cell in a SQUID magnetometer and Robert P. Smith carried out the resistivity measurements using a piston cylinder clamp cell and low frequency AC four probe technique with an ADR.

6.1 Experimental Method

A high-pressure environment was provided for these measurements by a miniature piston-cylinder type pressure cell 8mm in diameter, shown in *Figure 6.1*. The cell, developed by Ahilan and Saxena [Ahilan 2005], is constructed of high-purity non-magnetic BeCu. A PTFE capsule contains the sample and a hydrostatic pressure medium, with a freezing pressure well above the maximum pressure achieved. This cylindrical capsule is placed in the clamp cell, with a piston inserted in one end, as shown in *Figure 6.1*, which is secured in the base with a locking nut (right of image). A copper gasket at the sealed end of the capsule prevents the PTFE from flowing around the piston shown on the left. The piston on the left applies the pressure and is locked down with the nut on the left. The nut on the left has a hole in the top so that another piston can be used to press down on the piston in the cylinder while the nut on the left is tightened. For a good reference on pressure cells see Walker's paper on non-magnetic piston cylinder pressure cells [Walker 1999].

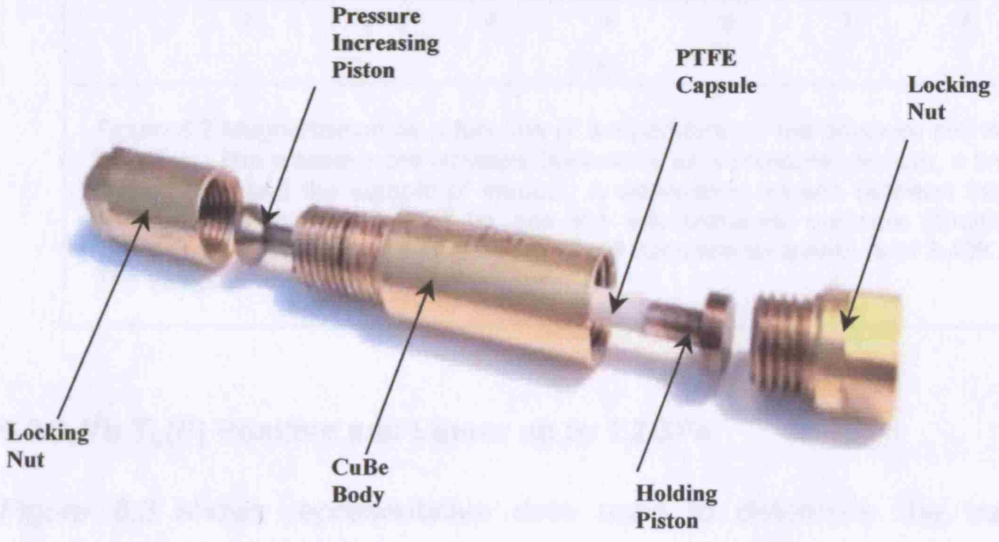

Figure 6.1 A miniature piston-cylinder pressure cell, described in the text, developed by Ahilan and Saxena.

The measured pressure shift of the superconducting transition of tin served as a pressure gauge [Smith 1969]. The raw data, an example of which is shown in *Figure 6.2*, appears inverted compared to that expected. This is an experimental artefact that lacks a full explanation and cannot as yet be systematically removed. The position and width of the transition is unaffected.

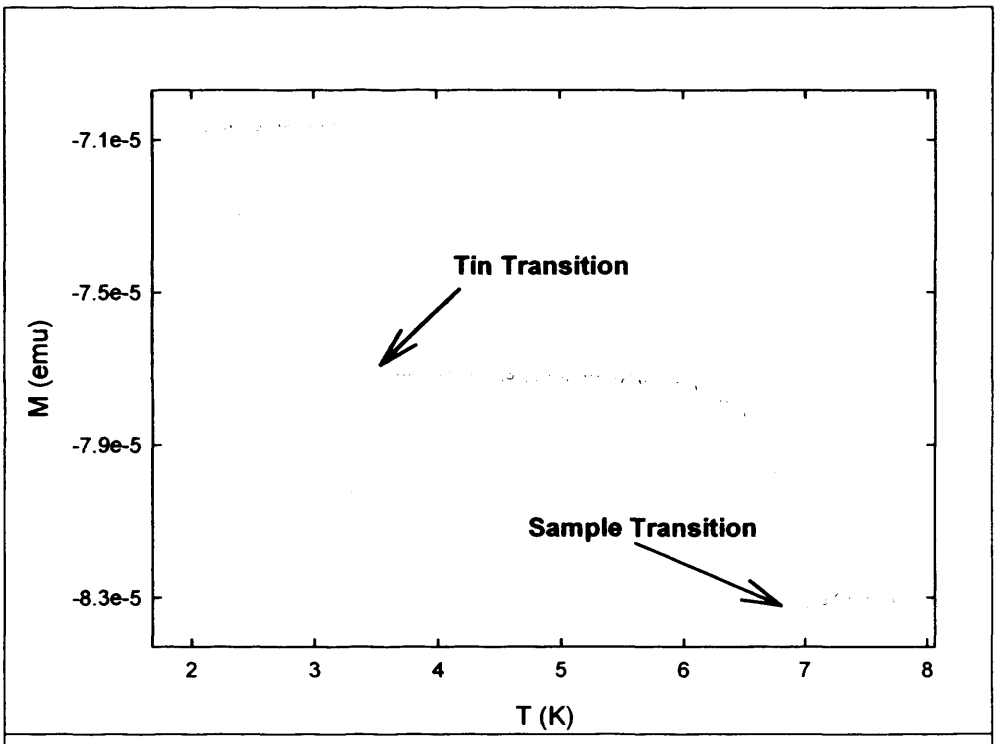

Figure 6.2 Magnetization as a function of temperature for the pressure cell in zero field. The pressure cell contains Daphne oil as a pressure medium, a tin manometer, and the sample of interest. A well-known relation between the superconducting transition of tin and the environmental pressure [Smith 1969] gives a pressure of 0.664GPa from the transition temperature of 3.40K. The sample transition is at 6.84K.

6.2 C_6Yb $T_C(P)$ Positive and Linear up to 1.2GPa

Figure 6.3 shows representative data used to determine the transition temperatures. The measurements were made in zero field, with the remnant field removed by magnet quench well above the superconducting transition of the sample. The upper half of the figure shows magnetization as a function of temperature at pressures of 0.4 GPa (circles) and 0.8 GPa (triangles) in the H//c-axis field orientation, the lower half shows resistivity as a function of temperature at pressures of 0.4 GPa (circles) and 0.9 GPa (triangles) in the H//ab-plane orientation. The magnetometry data has been inverted and

shifted to zero for clarity. The transition is taken as the maximum in the derivative of the data.

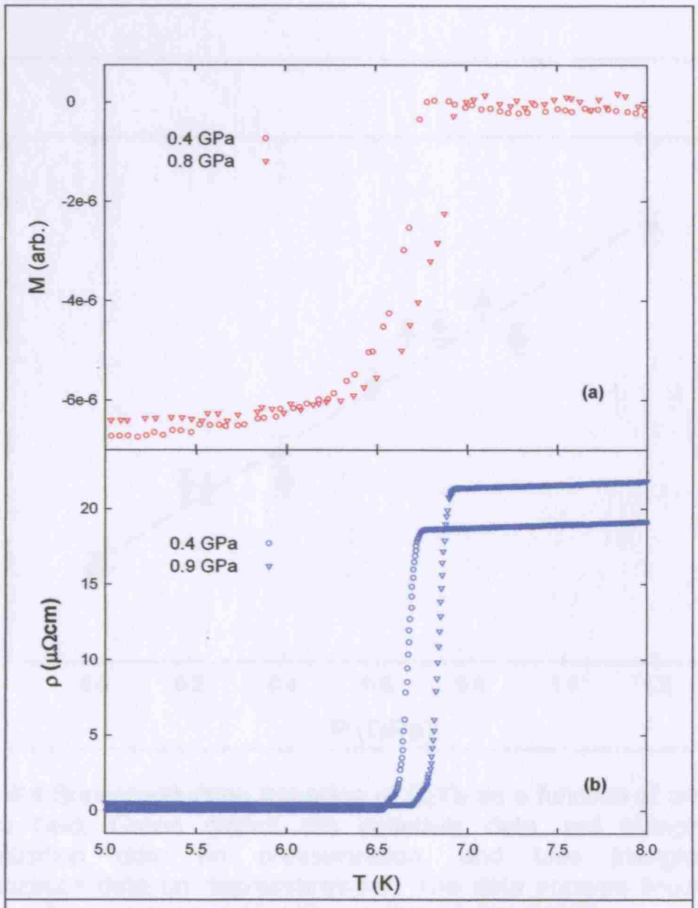

Figure 6.3 Data from pressure cell measurements of (a) magnetisation and (b) resistance in zero field. Pressures of 0.4 GPa (circles) and (a) 0.8 GPa (triangles) and (b) 0.9 GPa (triangles) with i//ab. The magnetometry data (a) has been inverted and shifted to zero for more convenient comparison with (b).

The superconducting transition temperature of C_6Yb in zero field, *Figure 5.7*, is found to increase linearly with pressure from ambient to at least 1.2GPa with a gradient of

$$dT_c/dP = +0.389 \pm 0.005 \text{ K/GPa}$$

Data from both resistivity and magnetization measurements are shown, demonstrating agreement between the two. These results were found to be reproducible after the removal and reapplication of pressure and demonstrate

that the shift in T_c is reversible. It is interesting to note that the c-axis of C_6Ba was found to reduce linearly with pressure up to 1.2GPa, without any structural phase transition [Fischer 1987].

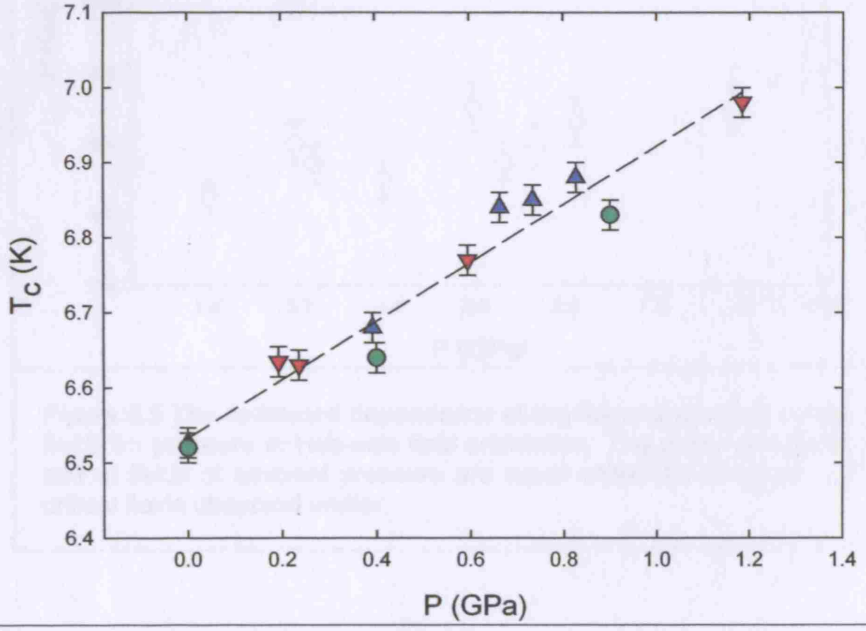

Figure 6.4 Superconducting transition of C_6Yb as a function of pressure, in zero field. Green circles are resistivity data, red triangles are magnetization data on pressurization, and blue triangles are magnetization data on depressurization. The data appears linear up to 1.2GPa, with a gradient of dTc/dP = +0.389 ±0.005 K/GPa.

The dependence of the upper and lower critical fields, *Figure 5.8*, has been estimated for H//c. These also appear to increase linearly. The reduction in the coherence length is about 10nm, over 1.2GPa, this is equivalent to 22 unit cell lengths, or 38 hexagon centres distances, in the ab-plane. This is about a 20% reduction in the coherence length.

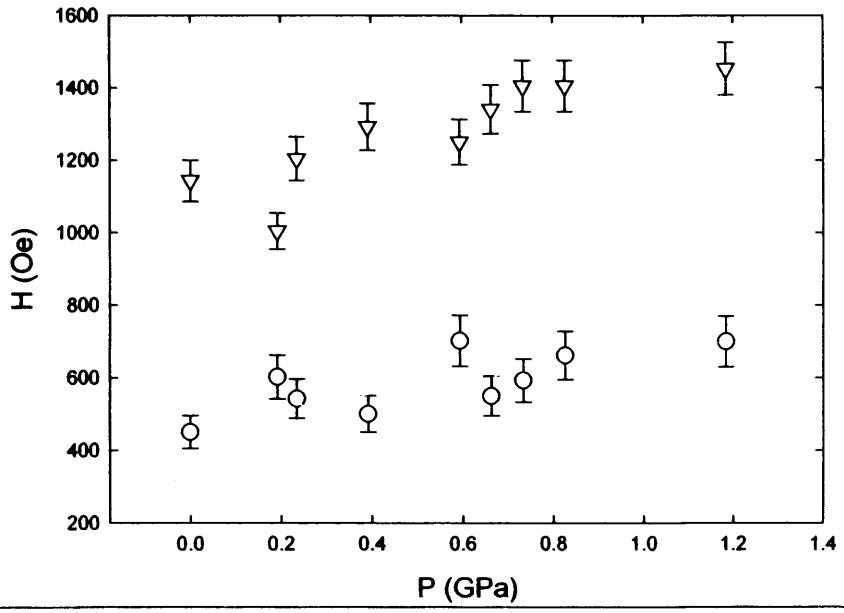

Figure 6.5 The estimated dependence of the lower and upper critical fields on pressure in H//c-axis field orientation. The upper and lower critical fields at ambient pressure are equal within the errors to the critical fields observed earlier.

6.3 Summary

The pressure dependence of the superconducting transition in C_6Yb is positive and appears linear up to 1.2GPa. The absence of broadening with pressure demonstrates that there is no change in the level of disorder in the system. The positive dependence of T_c on pressure shown in C_6Yb is the opposite to that observed in C_8KHg and C_4KHg and would not be expected within a conventional weak coupling phonon model.

Chapter 7

Discussion

This chapter discusses the results of my work in light of the pre-existing intercalate superconductors. It examines which factors should impact on our search for higher transition temperature in graphite intercalates and presents new results from recent studies, and current directions of our team's research. Concluding with comments on the development of sample synthesis.

C_6Yb is a superconductor below 6.5K [Weller 2005], this has been confirmed independently, in Cambridge and Toronto on samples I synthesized [Smith 2006, Sutherland 2006]. My initial measurements also showed an antiferromagnetic transition at around 2.5K. This led to the tantalising possibility that, in line with the hypothesis, the superconducting state in C_6Yb was mediated by antiferromagnetic fluctuations. However I was later able to show that this antiferromagnetic transition was associated with the presence of Yb_2O_3, and that there is no antiferromagnetic transition present in C_6Yb at ambient pressure. Furthermore, C_6Ca, chosen to compare with the potentially magnetic C_6Yb was also discovered to be a superconductor.

C_6Ca is a superconductor below 11.5K, and this has been confirmed completely independently, with samples synthesized by a new method [Emery 2005]. The motivating hypothesis has therefore yielded two new intercalated graphite superconductors, though the hypothesis is falsified at ambient pressure. *Figure 7.1* highlights the leap in transition temperatures provided by C_6Yb and C_6Ca. These new superconductors have transitions 1.5 and 2 orders of magnitude greater, respectively, than any ambient pressure synthesised binary graphite intercalates discovered before. C_6Yb and C_6Ca therefore represent the first opportunity for experimentalists to explore the superconductivity of binary graphite intercalate superconductors in a convenient low temperature, ambient pressure, regime.

Common to all superconducting graphite intercalates is the anisotropy conveyed by the host graphite. *Table 7.1* shows the GL coherence lengths published for various intercalates, and their anisotropy parameters Γ, calculated according to *Equation 1.19*. C_6Yb and C_6Ca have much shorter $\xi_{//ab}$ than all other intercalates. They also have much shorter $\xi_{//c}$ than alkali-binaries, but comparable to the $\xi_{//c}$ of alkali-mercury ternaries. C_6Yb and C_6Ca are much less anisotropic than all other graphite intercalates. This implies that a lower anisotropy in a binary-intercalate correlates to a higher transition temperature. However, the lowest anisotropy does not produce the highest transition temperature. Furthermore, since the ternary-intercalates have a higher anisotropy than the binary-intercalates but higher transition

temperatures it would be wrong to assume they superconduct by the same mechanism. Anisotropy does not correlate with higher transition temperatures.

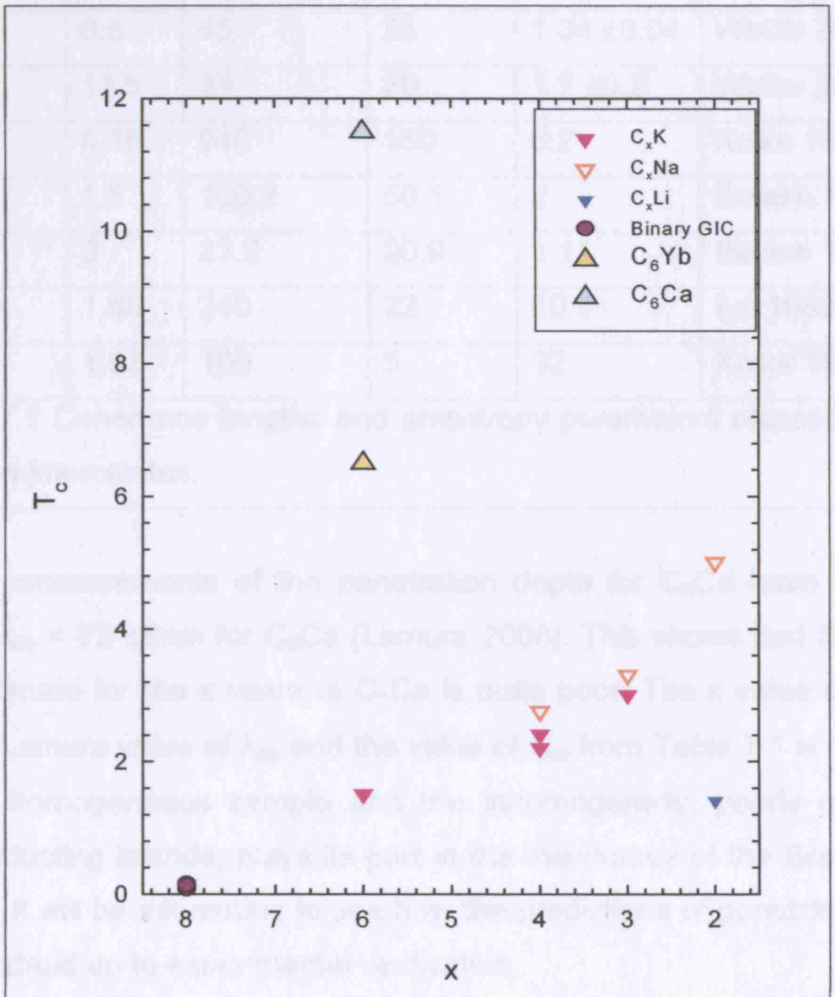

Figure 7.1 Transition temperatures for binary graphite intercalates, and pressure synthesized binary intercalates, with the transitions for C_6Yb and C_6Ca included.

The other significant length scale for superconductors is the penetration depth. This has been estimated for C_6Yb and C_6Ca using Brandt's curves. Brandt's curves allow indirect access to the value of the GL parameter κ, by the comparison of ideal curves to the measured dependence of the magnetisation on the applied field. Small values of κ would be expected given

the small values for most other intercalates. For C_6Yb κ = 1.75 ±0.25, and for C_6Ca a rather larger κ~5. Estimates of penetration depth appear in Table 7.2.

Intercalate	T_C (K)	$\xi_{//ab}$ (nm)	$\xi_{//c}$ (nm)	Γ	Author
C_6Yb	6.5	45	23	1.84 ±0.04	Weller 2005
C_6Ca	11.5	34	20	1.7 ±0.2	Weller 2005
C_8K	0.15	940	150	6.2	Koike 1980
C_6K	1.5	100.2	50.1	2	Belash 1990
C_3K	3	23.2	20.9	1.11	Belash 1990
C_4KHg	1.65	240	22	10.9	Iye 1983
C_8KHg	1.93	160	5	32	Koike 1981

Table 7.1 Coherence lengths and anisotropy parameters recorded for graphite intercalates.

The first measurements of the penetration depth for C_6Ca have yielded a value of λ_{ab} = 72 ±8nm for C_6Ca [Lamura 2006]. This shows that the Brandt curve estimate for the κ value of C_6Ca is quite poor. The κ value calculated from the Lamura value of λ_{ab} and the value of ξ_{ab} from *Table 7.1* is 1.9. C_6Ca is not a homogeneous sample and the inhomogeneity, poorly connected superconducting islands, plays its part in the inaccuracy of the Brandt curve estimate. It will be interesting to see how the predictions of penetration depth for C_6Yb stand up to experimental verification.

	$\lambda_{//ab}$ (2K)	$\lambda_{//c}$ (2K)
C_6Yb	90nm	50nm
C_6Ca	~200nm	~100nm

Table 7.2 The penetration depth for C_6Yb and C_6Ca, estimated from comparison of MH data with Brandt's curves.

The pressure studies, described in *Chapter 6*, have been continued by Ana Akrap in Titus Feher's group at Lausanne. A maximum in the pressure dependence of C_6Yb has been identified, and is shown in *Figure 7.2* where my work is reproduced alongside that of our collaborators. Possible mechanisms for the break down of superconductivity are a change in

structure with pressure, and the evolution of an Yb^{3+} state with pressure. Consequently application has been made to the ESRF to study both resonant inelastic x-ray scattering (Claudia Dallera) and diffraction (Mark Ellerby) as a function of pressure. Our team hopes to get beam time for these experiments this round. Initial RIXS data shows that the transition maximum may correlate with Yb^{2+} to Yb^{3+} transitions, suggesting that magnetism may develop a role in this system under pressure.

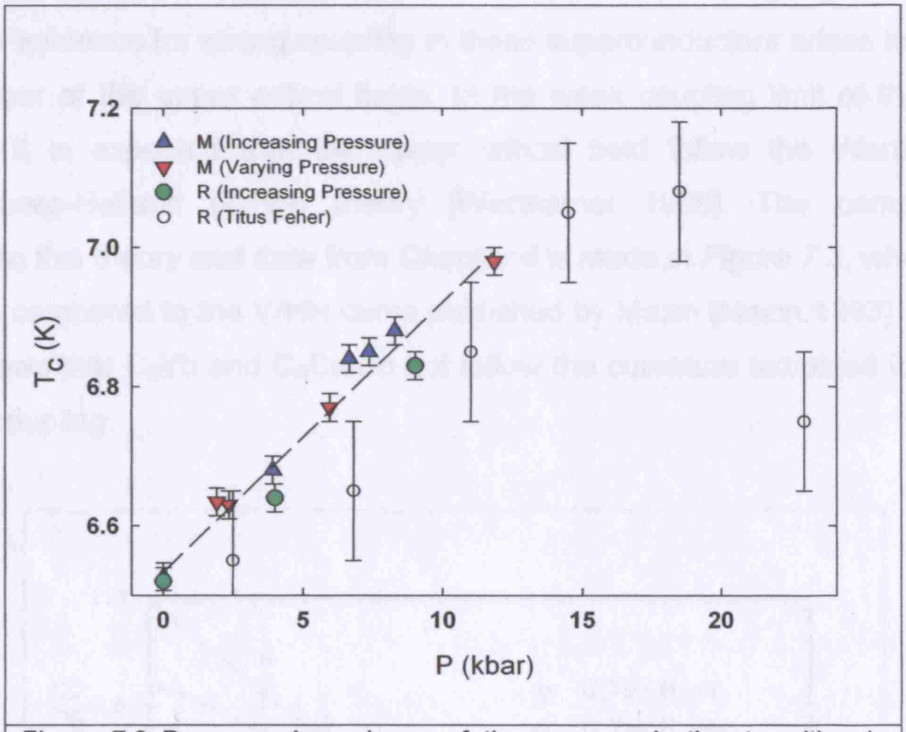

Figure 7.2 Pressure dependence of the superconducting transition in C6Yb. The open circles show the data from Feher's group in Lausanne.

Robert Smith has also continued to extend the work by measuring the pressure dependence of C_6Ca and demonstrating that it is also positive, but larger than that of C_6Yb with dT_C/dP = +0.4 K/GPa [Smith 2006]. Gauzzi et al. have measured the electrical resistivity of C_6Ca up to 16GPa, finding an increase up to 15.1K at 8GPa, where T_C drops and then levels off at 5K above 10GPa [Gauzzi 2006]. The authors suggest that this implies a continuous change of lattice spacing up to 8GPa. Above this pressure a new superconducting phase begins to nucleate within the sample. Once again inelastic and diffraction x-ray experiments will be required to resolve this question.

The pressure dependence demonstrated by C_6Yb and C_6Ca suggests they are outside the validity of the BCS approximation, where the potential experienced by the electrons is set constant. A weak coupling BCS superconductor in this regime would be expected to reduce its transition temperature with pressure, due to the reduction of $N(E_F)$ as discussed in *Section 1.2*. Therefore the pressure dependence points to a strong coupling regime as being appropriate to C_6Yb and C_6Ca.

Further evidence for strong coupling in these superconductors arises from the behaviour of the upper critical fields. In the weak coupling limit of the BCS theory it is expected that the upper critical field follow the Werthamer-Hohenberg-Helfand (WHH) theory [Werthamer 1966]. The comparison between this theory and data from *Chapter 4* is made in *Figure 7.3*, where the data is compared to the WHH curve published by Mazin [Mazin 1993]. *Figure 7.3* shows that C_6Yb and C_6Ca do not follow the curvature expected for BCS weak coupling.

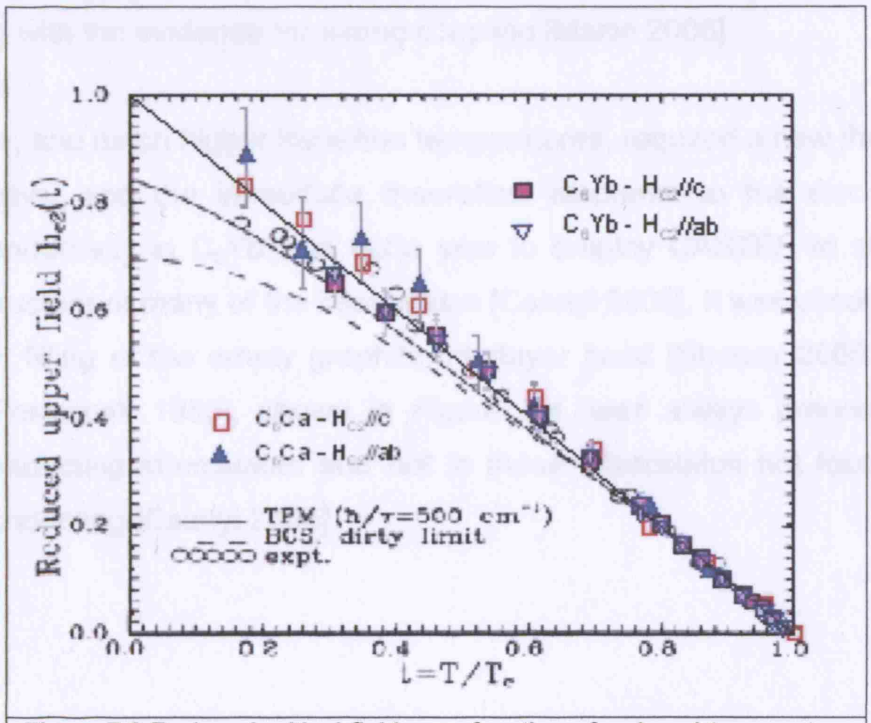

Figure 7.3 Reduced critical field as a function of reduced temperature in both field orientations for C_6Yb and C_6Ca, overlaid on the behaviour expected for the BCS approximation [Mazin 1993].

Various authors have ventured opinions as to whether C_6Yb and C_6Ca are strong or weak coupling superconductors. Lamura et al. measure the in-plane magnetic penetration depth by high-resolution mutual inductance and calculate λ_{ab} = 72 ±8nm and $\Delta(0)$ = 1.79 ±0.08meV, and argue that this value of $\Delta(0)$ indicates weak coupling superconductivity [Lamura 2006]. This value of $\Delta(0)$ is in good agreement with the value, obtained from Scanning Tunnelling Spectroscopy, of $\Delta(0)$ = 1.6 ±0.2meV [Bergeal 2006], these authors are also able to image the vortices and obtain a coherence length of ξ_{ab} = 33nm, in fine agreement with the value recorded in *Table 7.1*. Jobiliong et al. employ McMillan's formula to estimate the McMillan electron-phonon coupling λ_M = 0.85, and therefore suggest that C_6Ca is in the intermediate coupling regime [Jobiliong 2006]. Hinks et al. measured the isotope effect exponent, α, of C_6Ca and found it to be 0.5 [Hinks 2006] rather than the predicted 0.25 [Calandra 2005] also suggesting a strong coupling regime. There is not yet general agreement over the coupling regime into which the new superconductors fall. Mazin therefore highlights the main challenge regarding the superconductivity of C_6M: to reconcile the evidence for weak coupling with the evidence for strong coupling [Mazin 2006].

The new, and much higher transition temperatures, required a new theoretical perspective, and the immediate theoretical response to the discovery of superconductivity in C_6Yb and C_6Ca was to employ CASTEP to study the band structure of many of the intercalates [Csanyi 2005]. It was observed that a partial filling of the empty graphite interlayer band [Strocov 2000, Maeda 1988, Posternak 1983], shown in *Figure 7.4*, was always present in the superconducting intercalates and not in those intercalates not found to be superconducting [Csanyi 2005].

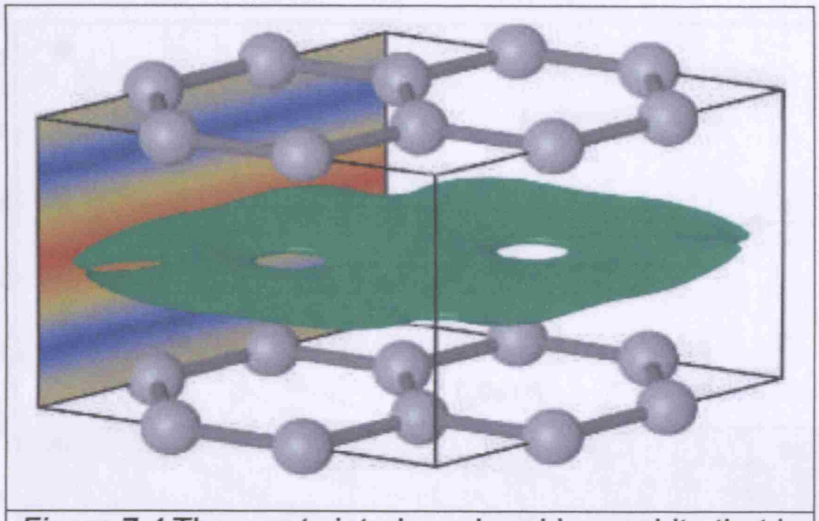

Figure 7.4 The empty interlayer band in graphite that is partially filled in all superconducting graphite intercalates [Csanyi 2005].

Figure 7.5 shows a phase plot of c-axis lattice constant and interlayer band energy [Csanyi 2005]. The gray region denotes the area where the interlayer band is partially filled. The black circles, and lines connecting them, show the interlayer band energy as a function of lattice constant for a given electron doping, where the electron-doping fraction is the number of electrons per carbon. The red crosses then show the superconducting intercalates and the blue show the non-superconducting intercalates. All the superconducting intercalates appear in the gray region.

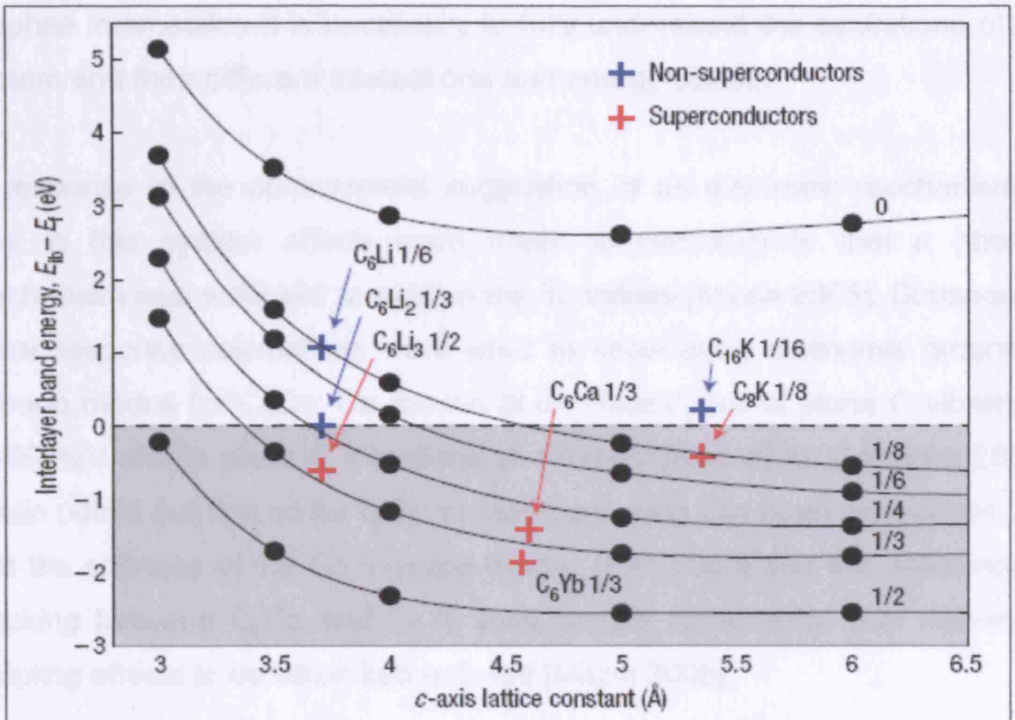

Figure 7.5 A phase diagram showing that all superconducting graphite intercalates have a partially filled interlayer band, and that all those that do not are not superconducting [Csanyi 2005].

This is an indisputable correlation [Mazin 2006], and it is perhaps not so important that it is difficult to distinguish whether this itinerant free-electron-like band is an interstitial state or an intercalant sp band [Mazin 2005], and more important to look for other indisputable correlations.

Csanyi's result was accompanied by the suggestion that Takada's model, discussed in *Section 2.3.5* [Takada 1982], of low energy plasmon modes might explain the apparent enhanced transition temperatures. Interestingly my values of Γ for C_6Yb and C_6Ca are much closer to Takada's predicted value. Most recently an acoustic plasmon model has been put forward for hypothetical superconductivity in a graphene sheet doped with potassium [Uchoa 2006].

None of the evidence presented so far can rule out plasmon-enhanced superconductivity, but undoubtedly phonons will be playing an important role. In order to understand the superconducting mechanism in these two new

graphite intercalates it is necessary to fully understand the excitations of the system and their different interactions and energy scales.

In response to the controversial suggestion of an electronic mechanism at play in this system efforts were made to demonstrate that a phonon mechanism was sufficient to explain the T_C values [Mazin 2005]. Subsequent linear response calculations were used to show three distinctive groups of phonon modes for C_6Ca: Ca modes at ω=10meV, out of plane C vibrations ω=60meV and in plane C vibrations at 170meV [Kim 2006, Calandra 2005]. Mazin points out that so far only harmonic coupling has been considered, but that the softness of the Ca in-plane modes [Kim 2006] and the difference in stacking between C_6Ca and C_6Yb may require anharmonic and non-linear coupling effects to be taken into account [Mazin 2006].

Thus experimental studies of the phonon band structures and their energies are of the utmost importance. Inelastic neutron scattering will help reveal the partial density of states of C_6Ca. Beam-time has been awarded for an experiment on MARI at ISIS to study the partial density of states. It will be very important to carry out further studies of the phonon structure of other intercalates to identify the common features. Unfortunately as yet not enough sample of C_6Yb can be generated to do inelastic neutron experiments on this material, so that further materials development is necessary to move this work forward.

Studies of the electronic structure and excitations must go hand in hand with studies of the phonon structure. Currently Rainer Friedlein is studying the Angle Resolved Ultraviolet Photoemission Spectroscopy (ARUPS) in order to understand the electronic structure of C_6Ca. Additionally plasmon modes could be studied by electron energy loss spectroscopy (EELS), and by optical spectrum measurements. Mazin has calculated the plasma frequencies and average Fermi velocities for C_6Yb and C_6Ca, and these are given in *Table 7.2* [Mazin 2005, Mazin 2006]. It will be interesting to measure the plasmon frequencies for C_6Yb and C_6Ca, as measurements made previously on other intercalates present higher plasmon frequencies for the π-plasmon 7-12eV

and the $\pi+\sigma$-plasmon 27-32eV. The possibility of a low energy intraband plasmon has also been identified at 100meV for stage 1 intercalates [Lin 1997]. This value is already lower than the C in plane phonon mode, but interestingly if the intraband plasmon energy scales the same way as the other plasmons in the system appear to then an energy of 25meV might be expected, and this would be similar to the soft calcium modes [Kim 2006, Calandra 2006].

Intercalate	ω_{ab} (eV)	ω_c (eV)	v_F (cm/sec x 10^8)
C_6Yb	6.2	3.6	2.4
C_6Ca	6.6	3.5	1.2

Table 7.3 Mazin's calculated values of the plasma frequencies.

Establishing the wavefunction symmetry is an important part of the process of understanding the nature of a superconductor. Experimental efforts have been made to establish the symmetry of the wave function in C_6Yb [Sutherland 2006] and in C_6Ca [Lamura 2006, Kim 2006, Bergeal 2006]. Lamura et al. showed that the temperature dependence of the penetration depth λ_{ab} of C_6Ca is consistent with s-wave pairing, and Bergeal et al. showed that the temperature dependence of the gap follows the form expected from the BCS theory. These results can be affected by the potential distortion of otherwise p or d-wave symmetry into s-wave at surfaces [Waldram p212]. Sutherland et al. on the other hand used a bulk technique to show that the temperature dependence of the thermal conductivity of C_6Yb is consistent with an s-wave order parameter, this measurement is much less sensitive to surface effects. The presence of the BCS mechanism, and s-wave symmetry, does not necessarily rule out the presence of other electronic interactions, such as plasmon enhancement.

Materials synthesis is an area requiring considerable effort, particularly for the application of neutron scattering techniques. C_6Ca is currently available in large quantities via a Lithium rich Lithium-Calcium alloy route [Emery 2005] and Ellerby et al. continue to innovate in this direction to provide large quantities of other intercalates.

Additional consideration may be given to the vapour transport route. Experiments could be undertaken to more carefully optimise the process, for instance a study of the intercalant penetration with time could be carried out simply, utilizing SEM imaging of cleaved samples. A calculation such as that of Madden et al, described in *Chapter 3*, could be applied to the whole gamut of intercalants so that the optimum substrate temperature for intercalant absorption and mobility can be identified.

It is interesting to consider what advantages might be gained from micro-structuring HOPG prior to intercalation in order to improve yield. It might be possible to achieve large intercalant yields by creating arrays of 100μm dots of HOPG on an HOPG substrate. Microstructural engineering might also be used to create samples stable in normal atmospheres since *Section 3.5.1* implies that if the edges can be protected, for instance by subsequent deposition of gold, then a region of intercalate should become robust against oxidation under normal atmosphere.

Control of the edge states and decorations may be important to improving yield by the vapour transport and other techniques. One type of edge decoration may favour the nucleation of intercalated regions where another might not. This could be an especially important aspect of the innovation as the kinetics of the transformation between two stages demonstrate a nucleation rather than diffusion limited process [Misenheimer]. A nucleation limited process being one in which the diffusion happens faster than new regions can be nucleated. If the nucleation can be improved then sample synthesis can be improved.

Superconductivity in graphite intercalates has been known since 1965, but progress has been slow. By the time the possibility of an upward trend related to conduction electron manipulation [Hennig 1952] was experimentally identified [Belash 1990] two events had occurred. The most important was the development of cuprate superconductors from 0.3K to the breakthrough 77K [Muller 1985, Wu 1987]. The second was the popularisation of fullerene science. These two events have stimulated so much creativity that now

returning to the graphite intercalates with ideas of coupling beyond the standard BCS phonon coupling we may find much to interest us. This approach has now led to two new superconductors in the class of binary graphite intercalates that push the transitions in this class of materials much higher. It remains to be seen how high graphite intercalate superconductors can go and though certainly these new materials have a component of their superconductivity governed by electron-phonon interactions, as must all superconductors, they may yet prove to exhibit a correlation that also has electronic contributions.

Bibliography

[Abrikosov 2003] Abrikosov's Nobel Lecture www.nobel.se

[Ahilan 1999] K. Ahilan and S.S. Saxena, *unpublished*, (1999)

[Al-Jishi 1983] R. Al-Jishi, Model for superconductivity in graphite intercalation compounds *Phys. Rev. B* **28** 112

[Al-Jishi 1992] R. A. Jishi et al. Superconductivity in graphite intercalation compounds *Phys. Rev. B* **45** 12465 (1992)

[Al-Jishi 1991] R. A. Jishi et al. Theory of the upper critical field in graphite intercalation compounds *Phys. Rev. B* **44** 10248 (1991)

[Anderson 1967] J. R. Anderson et al. Effect of Pressure on the Fermi Surface of Graphite *Phys. Rev.* **164** 1038 (1967)

[Ashcroft 1976] N. W. Ashcroft & N. D. Mermin, *Solid State Physics* Saunders College Publishing (1976)

[Avdeev 1990] V. V. Avdeev et al. The Alkali Metals in Graphite Matrixes: New Aspects of Metallic State Chemistry *High Pressure Research* **6** 11 (1990)

[Bandow 2001] S. Bandow et al. Unique magnetism observed in single-walled carbon nanohorns *Appl. Phys. A* **73** 281 (2001)

[Bardeen 1972] Bardeen's Nobel Lecture www.nobel.se

[Bauer 1999] E. Bauer, Non-Fermi-liquid behaviour of ytterbium compounds, **JMMM 196**, 873 (1999)

[Belash 1990] I.T. Belash et al. Effect of the Metal Concentration on the Superconducting properties of lithium-, sodium- and potassium-containing graphite intercalation compounds *Synthetic Metals* **36** 283 (1990)

[Bergeal 2006] N. Bergeal et al. Scanning Tunnelling Spectroscopy on the novel superconductor CaC_6 *arXiv:cond-mat* 0604208

[Bernal 1924] J. D. Bernal, The Structure of Graphite *Proc. R. Soc. London, Ser. A* **106** 749 (1924)

[Bernasconi 2002] L. Bernasconi & P. A. Madden, Structure and Short Timescale Ion Dynamics of Potassium-Ammonia Graphite Intercalation Compounds *J. Phys. Chem. B* **106** 1161 (2002)

[Bloch 1985] J. M. Bloch et al. X-ray observation of a $\sqrt{3}$ x $\sqrt{3}$ superlattice in KC_8 at high pressure *Phys. Rev. B* **31** 6785 (1985)

[Blundell 2001] S. Blundell, *Magnetism in Condensed Matter* OUP (2001)

[Brandt 1997] E. H. Brandt, Precision Ginzburg-Landau Solution of Ideal Vortex Lattices for Any Induction and Symmetry *Phys. Rev. Lett.* **78** 2208 (1997)

[Broussely 1997] M. Broussely et al. Lithium ion batteries for electric vehicles: performances of 100 Ah cells *J. Power Sources* **68** 8-12 (1997)

[Buzea 2004] C. Buzea & K. Robbie, Assembling the puzzle of superconducting elements: A Review *Supercond. Sci. Technol.* **18** R1 (2005)

[Calandra 2005] M. Calandra & F. Mauri Theoretical Explanation of Superconductivity in C_6Ca *Phys. Rev. Lett.* **95** 237002 (2005)

[Calandra 2006] M. Calandra & F. Mauri Possibility of superconductivity in graphite intercalated with alkaline earths investigated with density functional theory *arXiv:cond-mat* 0606372 (2006)

[Chaiken 1998] A. Chaiken Superconducting properties of ternary graphite intercalation compounds *PhD. Thesis MIT* (1998)

[Clarke 1980] R. Clarke et al. Pressure Induced Staging Transition in KC_{24} *Phys. Rev. Lett.* **44** 1616 (1980)

[Clarke 1981] R. Clarke et al. *Physics of Solids Under High Pressure* Schilling and Shelton (eds.) North-Holland Publishing Company (1981)

[Clarke 1984] R. Clarke & C. Uher, High pressure properties of graphite and its intercalation compounds *Adv. Phys.* **33** 469 (1984)

[Claus 2001] H. Claus et al. Critical current across grain boundaries in melt-textured $YBa_2Cu_3O_{7-\delta}$ rings *Phys. Rev. B* **64** 144507 (2001)

[Cousins 2003] C. S. G. Cousins and M. I. Heggie, Elasticity of Carbon Allotropes. III. Hexagonal graphite: Review of data, previous calculations, and a fit to a modified anharmonic Keating model *Phys. Rev. B* **67** 024109 (2003)

[Csanyi 2005] G. Csanyi et al. The role of the interlayer state in the electronic structure of superconducting graphite intercalated compounds *Nature Physics* **1** 42 (2005)

[DeLong 1982] L. E. DeLong et al, Observation of anomalies in the pressure dependence of the superconducting transition temperature of potassium-based graphite intercalation compounds *Phys. Rev. B* **26** 6315 (1982)

[DeLong 1983] L. E. DeLong & P. C. Eklund, Superconductivity at high pressures in graphite intercalation compounds *Synthetic Metals* **5** 291 (1983)

[DiVincenzo 1982] D. P. DiVincenzo & S. Rabii, Theoretical investigation of the electronic properties of potassium graphite *Phys. Rev. B* **25** 4110 (1982)

[Dresselhaus 1981] M. S. Dresselhaus & G. Dresselhaus Intercalation compounds of graphite *Adv. Phys.* **30** 139 (1981)

[Du 2005] X. Du et al. Metal-Insulator-Like Behaviour in Semimetallic Bismuth and Graphite *Phys. Rev. Lett.* **94** 166601 (2005)

[El-Makrini 1980] M. El-Makrini et al. Intercalation of Rare Earth Metals in Graphite *Physica B + C* **99** 481 (1980)

[Ellerby 2005] M. Ellerby et al. Superconductivity at elevated temperatures in C_6Yb and C_6Ca *Physica B* **378-380** 636 (2006)

[Emery 2005] N. Emery Superconductivity of Bulk CaC_6 *Phys. Rev. Lett.* **95** 087003 (2005)

[Enoki 2003] Enoki et al. *Graphite Intercalation Compounds and Applications* OUP (2003)

[Fischer 1987] J. E. Fischer et al. Neutron-diffraction studies of BaC_6: c-axis compressibility, carbon-carbon bond length, and charge transfer *Phys. Rev. B* **36** 4449 (1987)

[Fredenhagen 1926] K. Fredenhagen & G. Cadenbach, Die Bindung von Kalium durch Kohlenstoff *Z.Anorg.Allg.Chem.* **158** 249 (1926)

[Gallagher 2001] C. Gallagher & J. Goodyer unpublished.

[Gauzzi 2006] A. Gauzzi et al. Pressure-induced enhancement of superconductivity and superconducting-superconducting transition in CaC6 *arXiv:cond-mat* 0603443 v1

[GE Quartz Europe] GE Quartz Europe GmbH, Borsigstrase 1-7, D-21502 Geesthacht, Germany

[Girifalco 2000] L. A. Girifalco et al. Carbon nanotubes, buckyballs, ropes, and a universal graphitic potential *Phys. Rev. B* **62** 13104 (2000)

[Guérard 1975] Guérard D. et al. Intercalation of lithium into graphite and other carbons *Carbon* **13** 337 (1975)

[Guérard 1979] D. Guérard et al. Insertion de Metaux Alcalino-Terreux Dans Le Graphite *Carbon* **18** 257-264 (1979)

[Hannay 1965] N. B. Hannay et al. Superconductivity in Graphitic Compounds *Phys. Rev. Lett.* **14** 225 (1965)

[Hennig 1952] G. Hennig & L. Meyer, Search for Low Temperature Superconductivity in Graphite Compounds *Phys. Rev.* **87** 439 (1952)

[Heremans 1994] J. Heremans et al. Magnetic susceptibility of carbon structures *Phys. Rev. B* **49** 15122 (1994)

[Hérold 1955] A. Hérold et al. Recherches sur les composes d'insertion du graphite *Bull. Soc. Chim. Fr.* **187** 999 (1955)

[Hinks 2006] D. G. Hinks et al. Large Ca Isotope Effect in CaC_6 *arXiv:cond-mat* 0604642 (2006)

[Holzwarth 1978] N. A. W. Holzwarth et al. Theoretical study of lithium graphite. I. Band structure, density of states, and Fermi-surface properties *Phys. Rev. B* **18** 5190 (1978)

[LBL 2006] www-cxro.lbl.gov/optical_constants/atten2.html

[Inoshita 1977] T. Inoshita et al. Electronic Structure of Potassium-Graphite Intercalation Compound: C_8K *J. Phys. Soc. Jap.* **43** 1237 (1977)

[Iye 1982] Y. Iye & S. Tanuma, Superconductivity of graphite intercalation compounds with alkali-metal amalgams *Phys. Rev. B* **25** 4583 (1982)

[Iye 1983] Y. Iye & S. Tanuma, Superconductivity of graphite intercalation compounds-state and pressure dependence of anisotropy, *Synth. Met.* **5** 257 (1983)

[Iye 1985] Y. Iye et al. Non-Ohmic Transport in the Magnetic-Field-Induced Charge-Density-Wave Phase of Graphite *Phys. Rev. Lett.* **54** 1182 (1985)

[Jobiliong 2006] E. Jobiliong et al. Quasi-2D superconductivity and Fermi-liquid behaviour in bulk CaC_6 *arXiv:cond-mat* 0604062

[Kaindl 1983] G. Kaindl et al. Electronic and Magnetic Properties of Europium-Intercalated Graphite *Phys. Rev. Lett.* **50** 123 (1983)

[Kamitakahara 1985] W. A. Kamitakahara In-plane intercalate dynamics in alkali-metal graphite intercalation compounds *Phys. Rev. B* **32** 7817 (1985)

[Kaneiwa 1982] S. Kaneiwa et al. Superconductivity in the Potassium Graphite Hydride $C_8KH_{0.19}$ J. Phys. Soc. Jap. **51** 2375 (1982)

[Keithley 1998] J. Keithley, *Low Level Measurements Handbook* Keithley Instruments, Inc. (1998)

[Kelly 1981] B. T. Kelly, *Physics of Graphite*, Applied Science Publishing (1981)

[Kim 2006] J. S. Kim et al. Effect of Pressure on Superconducting Ca-Intercalated Graphite CaC_6 *arXiv:cond-mat* 0603530

[Kittel 1996] C. Kittel *Introduction to Solid State Physics* John Wiley & Sons, Inc. (1996)

[Klaasse 1981] J. C. P. Klaasse et al. Systematics in Intermetallic Compounds Containing Intermediate-Valent Ytterbium *Physica B* **106** 178 (1981)

[Klemm 1992] R. A. Klemm, Generic properties of layered superconductors *AIP Conference Proceedings* **273** 292 (1992)

[Kobayashi 1979] M. Kobayashi & I Tsujikawa, Susceptibility Fluctuation in Superconducting First Stage Potassium Graphite Intercalation Compound near Transition Temperature *J. Phys. Soc. Jap.* **46** 1945 (1979)

[Kobayashi 1983] M. Kobayashi et al. Responsible Layer for Superconductivity in the First Stage Potassium Graphite Intercalation Compound *J. Phys. Soc. Jap.* **52** 1890 (1983)

[Koike 1978] Y. Koike et al. Superconductivity in graphite-potassium intercalation compound C_8K *Solid State Comm* **27** 623 (1978)

[Koike 1980] Y. Koike et al. Superconductivity in the graphite-potassium intercalation compound C_8K *J. Phys. Chem. Solids* **41**, 1111 (1980)

[Koike 1981] Y. Koike & S. Tanuma, Anisotropic Superconductivity in the Graphite Potassium-Amalgam Intercalation Compound C_8KHg *J. Phys. Soc. Jap.* **50** 1964 (1981)

[Koma 1986] A. Koma et al. Density-of-states investigation of C8K and occurrence of the interlayer band *Phys. Rev. B* **34** 2434 (1986)

[Lamura 2006] G. Lamura et al. Experimental Evidence of s-Wave Superconductivity in Bulk CaC_6 *Phys. Rev. Lett.* **96** 107008 (2006)

[Lang 1994] L. Lang et al. Dynamical study of graphite and graphite intercalation compounds *Phys. Rev. B* **49** 5672 (1994)

[LBL 2006] www-cxro.lbl

[Lide 1994] CRC Handbook of Chemistry and Physics, 75th edition. Florida: Chemical Rubber Co, **1994**.

[Lin 1997] M. F. Lin et al. Plasmons in graphite and stage-1 graphite intercalation compounds *Phys. Rev. B* **55** 13961 (1997)

[Lindsell 1998] G. A. Lindsell Structure and Dynamics of Graphite Intercalation Compounds *PhD Thesis* Australian National University (1998)

[Maeda 1988] F. Maeda et al. Unoccupied-electronic-band structure of graphite studied by angle-resolved secondary-electron emission and inverse photoemission *Phys. Rev. B* **37** 4482 (1988)

[El-Makrini 1980] M. El-Makrini et al. *Physica B* **99** 481-485 (1980)

[Matsubara 1990] K. Matsubara et al. Electrical resistance in the c direction of graphite *Phys. Rev. B* **41** 969 (1990); erratum **46** 1948 (1992)

[Mazin 2005] I. I. Mazin & S. L. Molodtsov, Electrons and phonons in YbC6: Density functional calculations and angle-resolved photoemission measurements *Phys. Rev. B* **72** 172504 (2005)

[Mazin 1993] I. I. Mazin et al. Strong-coupling effects in alkali-metal-doped C_{60} *Phys. Rev. B* **47** 538 (1993)

[Mazin 2005] I. I. Mazin, Intercalant-Driven Superconductivity in YbC6 and CaC6 *Phys. Rev. Lett.* **95** 227001 (2005)

[Mazin 2006] I. I. Mazin et al. Unresolved problems in superconductivity of CaC6 *arXiv:cond-mat* 0606404

[McMillan 1968] W. L. McMillan Transition Temperature of Strong-Coupled Superconductors *Phys. Rev.* **167** 331 (1968)

[Misenheimer 1985] M. E. Misenheimer & H. Zabel, Stage Transformation and Staging Disorder in Graphite Intercalation Compounds *Phys. Rev. Lett.* **54** 2521 (1985)

[Moffatt 1976] W. G. Moffatt, *The Handbook of Binary Phase Diagrams* Genium Publishing (1976)

[Molodtsov 1996] S. L. Molodtsov et al. Electronic structure of Eu and Yb graphite intercalation compounds *Phys. Rev. B* **53** 16621 (1996)

[Monthoux 2001] P. Monthoux and G.G. Lonzarich, Magnetically mediated superconductivity in quasi-two and three dimensions, *Phys. Rev. B* **63** 054529 (2001)

[Morris 1972] R. C. Morris et al. Superconductivity and Magnetoresistance in $NbSe_2$ *Phys. Rev. B* **5** 895 (1972)

[Muller 1985] Muller's Nobel Lecture www.nobel.se (1985)

[Ohno 1979] T Ohno et al. Self-Consistent Calculation of the Band Structure of C_8K Including the Charge Transfer Effect *J. Phys. Soc. Jap.* **47** 1125 (1979)

[Onnes 1913] Onnes' Nobel Lecture www.nobel.se

[Osborn 1945] J. A. Osborn, Demagnetizing Factors of the General Ellipsoid *Phys. Rev.* **67** 351 (1945)

[Pietronero 1981] L. Pietronero & S. Strässler, Bond-Length Change as a Tool to Determine Charge Transfer and Electron-Phonon Coupling in Graphite Intercalation Compounds *Phys. Rev. Lett.* **47** 593 (1981)

[Posternak 1983] M. Posternak et al. Prediction of Electronic Interlayer States in Graphite and Reinterpretation of Alkali Bands in Graphite Intercalation Compounds *Phys. Rev. Lett.* **50** 761 (1983)

[Preil 1984] M. E. Preil & J. E. Fischer X-Ray Photoelectron Study of the Valence Band of KC8: Direct Experimental Proof of Complete K (4s) Charge Transfer *Phys. Rev. Lett.* **52** 1141 (1984)

[Meservey 1969] R. Meservey & B. B. Schwartz, in *Superconductivity*, ed. R. D. Parks (Dekker, New York, 1969).

[Richardson 1977] D. D. Richardson, A calculation of Van der Waals interactions in and between layers of atoms: application to graphite *J. Phys. C: Solid State Phys.* **10** 3235 (1977)

[Ritsko 1981] J. J. Ritsko et al. Excitations of back-folded graphite bands in KC_8 *Phys. Rev. B* **24** 6114 (1981)

[Ritsko 1982] J. J. Ritsko, Valence- and core-electronic excitations in potassium-intercalated graphite *Phys. Rev. B* **25** 6452 (1982)

[Roth 1985] G. Roth et al. Enhanced superconductivity in hydrogenated potassium-mercury-graphite intercalation compounds *Phys. Rev. B* **32** 533 (1985)

[Lide 1994] D. R. Lide, *CRC Handbook of Chemistry and Physics* The Chemical Rubber Publishing Company (1994)

[Safran 1979] S. A. Safran & D. R. Hamann, Long-Range Elastic Interactions and Staging in Graphite Intercalation Compounds *Phys. Rev. Lett.* **42** 1410 (1979)

[Salzano 1965] F. J. Salzano & S. J. Aronson, Kinetic Study of the Decomposition of Cesium-Graphite Lamellar Compounds *J. Chem. Phys.* **42** 1323 (1965)

[Shikin 1995] A. M. Shikin et al. Electronic structure of La-intercalated graphite *Phys. Rev. B* **51** 13586 (1995)

[Shoenberg 1962] D. Shoenberg *Superconductivity* CUP 1962

[Smith 1969] T. F. Smith et al. Superconducting manometers for high pressure measurement at low temperature *Cryogenics* 9 53 (1969)

[Smith 2006] R. P. Smith et al. Pressure dependence of the superconducting transition temperature in C6Yb and C6Ca *Phys. Rev. B* **74** 024505 (2006)

[Solin 1988] S.A. Solin & H. Zabel, The physics of ternary graphite intercalation compounds *Adv. Phys.* **37** 87 (1988)

[Song 2004] M. K. Song et al. No Substitution Effect of Carbon with Group 13, 14, and 15 Elements on Lithium Intercalation in Graphite *J. Electrochem. Soc.* **151** A1696 2004

[Stamenov 2005] P. Stamenov et al. Shubnikov de Haas and Hall quantum oscillations in graphite *J. M. M. M.* **290-291** 1402 (2005)

[Stephens 1971] A. E. Stephens et al. Effects of Contact Placement and Sample Shape in the Measurement of Electrical Resistivity *J. Appl. Phys.* **42** 2592 (1971)

[Strocov 2000] V. N. Strocov et al. Three-dimensional unoccupied band structure of graphite: Very-low-energy electron diffraction and band calculations *Phys. Rev. B* **61** 4994 (2000)

[Suematsu 1980] H. Suematsu et al. Electronic Properties of Graphite-Potassium Intercalation Compounds. II. Resistivity, Hall Effect and Magnetoresistance *J. Phys. Soc. Jap.* **48** 1541 (1980)

[Suhl 1959] H. Suhl et al. Bardeen-Cooper-Schrieffer Theory of Superconductivity in the Case of Overlapping Bands *Phys. Rev. Lett.* **3** 552 (1959)

[Sutherland 2006] Mike Sutherland et al. Bulk evidence for single-gap s-wave superconductivity in the intercalated graphite superconductor C6Yb *arXiv:cond-mat* 0603664

[Takada 1978] Y. Takada Plasmon Mechanism of Superconductivity in Two- and Three-Dimensional Electron Systems *J. Phys. Soc. Jap.* **45** 786 (1978)

[Takada 1982] Y. Takada Mechanism of Superconductivity in Graphite-Alkali Metal Intercalation Compounds *J. Phys. Soc. Jap.* **51** 63 (1982)

[Tarascon 1993] J. M. Tarascon et al. The $Li_{1+x}Mn2O_{4/C}$ rocking-chair system: a review *Electrochimica Acta* **38** 1221 (1993)

[Timp 1983] Gregory L. Timp, Studies on Graphite Intercalation Compounds *PhD thesis* Massachusetts Institute of Technology (1983)

[Tinkham 1975] M. Tinkham *Introduction to Superconductivity* McGraw Hill Inc. (1975)

[Uchoa 2006] B. Uchoa & A. H. Castro-Neto, Superconductivity in metal coated graphene *arXiv:cond-mat* 0608515

[UDEL 2006] www.udel.edu/chem/GlassShop

[Uher 1984] R. Clarke & C. Uher, High pressure properties of graphite and its intercalation compounds *Adv. Phys.* **33** 469 (1984)

[Uher 1987] C. Uher et al. Pressure dependence of the c-axis resistivity of graphite *Phys. Rev. B* **35** 4483 (1987)

[UK Mains] www.nationalgrid.com/uk/Electricity/Data

[Vogel 1981] Vogel et al. **34** 373 (1989)

[Waldram 1996] J. R. Waldram, *Superconductivity of Metals and Cuprates* IoP Publishing Ltd. (1996)

[Walker 1999] I. R. Walker, Nonmagnetic piston–cylinder pressure cell for use at 35 kbar and above *Rev. Sci. Inst.* **70** 3402 (1999)

[Walters 1999] J. K. Walters et al. The interlayer structure of a graphite-potassium-ammonia intercalation compound by neutron diffraction *Chem. Phys. Lett.* **300** 444 (1999)

[Wang 1991] G. Wang et al. Fermi surface of the stage-1 potassium graphite intercalation compound *Phys. Rev. B* **44** 8294 (1991)

[Weber 1978] H. W. Weber et al. Transition from Type-II to Type-I Superconductivity with Magnetic Field Direction *Phys. Rev. Lett.* **41** 1502 (1978)

[Weller 2005] T. E. Weller et al. Superconductivity in the intercalated graphite compounds C_6Yb and C_6Ca *Nature Physics* **1** 39 (2005)

[Werthamer 1966] N. R. Werthamer et al. Temperature and Purity Dependence of the Superconducting Critical Field, H_{C2}. III. Electron Spin and Spin-Orbit Effects *Phys. Rev.* **147** 295 (1966)

[Wilson 1982] Wilson's Nobel Lecture www.nobel.se

[Winter 2006] M. Winter *The Orbitron* www.shef.ac.uk/chemistry/orbitron/

[Wu 1987] M. K. Wu et al. Superconductivity at 93K in a New Mixed-Phase Y-Ba-Cu-O Compound System at Ambient Pressure *Phys. Rev. Lett.* **58** 908 (1987)

[Yamaya 2002] K. Yamaya et al. The effect of pressure on the charge-density wave and superconductivity in $ZrTe_3$ *J. Phys.: Condens. Matter* **14** 10767 (2002)

[Yeh 1982] V. Yeh et al. *Bull. Am. Phys. Soc.* 340 (1982)

[Zabel 1982] H. Zabel & A. Magerl, Inelastic neutron measurement of phonons in graphite-alkali intercalation compounds *Phys. Rev. B* **25** 2463 (1982)

[Zabel 1983] H. Zabel et al. Planar Diffusive Motion of Alkali-Metal Intercalant Atoms in Graphite *Phys. Rev. Lett.* **50** 2094 (1983)

[Zabel 2001] H. Zabel, Phonons in layered compounds *J.Phys.: Condens. Matter* **13** 7679 (2001)

[Ziman 1960] J. M. Ziman, *Electrons and Phonons The Theory of Transport Phenomena in Solids* OUP (1960)